Title
Structural Analysis of Cell Components and Cell division in Archaeal Cells

Author
Toso, Daniel B

Publication Date
2013

Peer reviewed|Thesis/dissertation

UNIVERSITY OF CALIFORNIA

Los Angeles

Structural Analysis of Cell Components and Cell division in Archaeal Cells

A dissertation submitted in partial satisfaction of the requirements for the degree

Doctor of Philosophy in Biomedical Engineering

by

Daniel Brizuela Toso

2013

ABSTRACT OF THE DISSERTATION

Structural Analysis of Cell Components and Cell division in Archaeal Cells

by

Daniel Brizuela Toso

Doctor of Philosophy in Biomedical Engineering

University of California, Los Angeles, 2013

Professor Z. Hong Zhou, Chair

Archaea occupy one of the three domains of life and it is recognized that many of their cellular processes bear more similarity to their analogous processes in eukaryotic cells than the comparable processes in prokaryotic cells. However, despite the fact that archaeal cells are similar in complexity to bacterial cells, they have been studied to a much lesser extent, with the majority of species yet to be examined at all in the laboratory. Further study of this domain of life can be expected to contribute to the understanding of the cellular processes in higher organisms, including humans. In particular, very little is known about the structures and morphogenesis of archaeal cells. The studies described here aim to fill this knowledge gap by examining and resolving the structures of archaeal cells under a variety of conditions and with different techniques. Specifically, this work characterized the unique structural components of archaeal cells, analyzed the properties of concentrated inclusion bodies, and examined structural changes throughout cell division in archaeal cells. A combination of biophysical methods, including cryo electron microscopy (cryo EM), cryo electron tomography (cryo ET), scanning transmission EM (STEM) tomography, and energy dispersive x-ray (EDX)

spectroscopy, were used to identify and characterize high-density polyphosphate bodies distributed within the *Methanospirillum hungatei* cell cytoplasm, two distinct high-density inclusion bodies distributed within the *Archeaoglobus fulgidus* cytoplasm, and the processes of cell division in both *M. hungatei* and *A. fulgidus*.

The dissertation of Daniel Brizuela Toso is approved.

Feng Guo

Lily Wu

Robert Gunsalus

Timothy Deming

Z. Hong Zhou, Committee Chair

University of California, Los Angeles

2013

DEDICATION

To my family, for always believing in me no matter what, especially my Mom, who always encourages me to be a better version of myself.

TABLE OF CONTENTS

LIST OF ACRONYMS

3D – Three-Dimensional

ADF – Annular Dark-Field

ATP – Adenosine Triphosphate

CCD – Charge-Coupled Device

cryo EM – cryo Electron Microscopy

cryo ET – cryo Electron Tomography

DGCR8 – DiGeorge syndrome Critical Region 8

DNA – Deoxyribonucleic Acid

dsRBD – double stranded RNA Binding Domain

EDX – Energy Dispersive X-ray (spectroscopy)

EM – Electron Microscopy

ET – Electron Tomography

FtsZ – Filamentous temperature-sensitive mutant Z

GDP – Guanosine Diphosphate

GIF – Gatan Imaging Filter

GPU – Graphics Processing Unit

GTP – Guanosine Triphosphate

HAADF – High Angle Annular Dark-Field

ISB – Iron Sulfide Body

MCM – Mini-Chromosome Maintenance (protein)

MVP – Major Vault Protein

PPB – Polyphosphate Body

PPK – Polyphosphate Kinase

RNA – Ribonucleic Acid

RPM – Revolutions Per Minute

S-layer – Surface layer

SEM – Scanning Electron Microscope

SIRT – Simultaneous Iterative Reconstruction Technique

SNR – Signal-to-Noise Ratio

STEM – Scanning Transmission Electron Microscope

TEM – Transmission Electron Microscope

TIA – TEM Imaging and Analysis

TMV – Tobacco Mosaic Virus

UA – Uranyl Acetate

LIST OF FIGURES

ACKNOWLEDGEMENTS

I would, first of all, like to thank my advisor, Prof. Hong Zhou, for providing me with guidance and a model for success and for always pushing me to be a better scientist, with varying success. I would also like to sincerely thank all of the members of my PhD committee for their valuable time and insight: Prof. Feng Guo, Prof. Lily Wu, Prof. Robert Gunsalus, and Prof. Timothy Deming.

I would like to thank all of the current and past members of the Zhou lab: Ivo Atanosov, Dr. Xing Zhang, Wong Hoi Hui, Dr. Jiansen Jiang, Dr. Sakar Shivakoti, Dr. Peng Ge, Dr. Xui-kui Yu, Xinghong Dai, Nicole Poweleit, Dr. Louise Hughes, Dr. Hongrong Liu, Dr. Li Peng, Dr. Lingpeng Cheng and Dr. Lei Jin. They always provided me with standards to emulate in my microscopy and research endeavors.

I would like to thank my collaborators in the Gunsalus lab: Prof. Rob Gunsalus, Dr. Anne Meint Henstra, Dr. Lars Rohlin, Nicole Poweleit, Dr. Mohsin Javed, and Andrea Rivera. I couldn't have done this work without their support and the samples they provided.

Finally, I would like to thank all of my undergrads, who provided invaluable help, encouragement, and friendship: Kevin Chen, Justin Chen, Connie Huang, Jennifer Wong, Tracey Tan, Jessica Chinison, Jenny Lin, Simon Cheong, Edward Amador, and all of my MIMG 105 students.

BIOGRAPHICAL SKETCH

Daniel B. Toso

EDUCATION UNIVERSITY OF CALIFORNIA, LOS ANGELES

Ph.D. Biomedical Engineering, Summer 2013

M.S. Biomedical Engineering, 2009

UNIVERSITY OF MINNESOTA, Twin Cities

Ph.D. candidate Biomedical Engineering, 2004-2006

Advisor: Dr. Osha Roopnarine, Biochemistry Lab

UNIVERSITY OF CALIFORNIA, BERKELEY

B.S. Bioengineering, 2004

TEACHING EXPERIENCE UNIVERSITY OF CALIFORNIA, LOS ANGELES

DEPARTMENT OF MIMG 2010-2012

PUBLICATIONS

1. Toso, D.B., Henstra, A.M., Gunsalus, R.P., and Zhou, Z.H. (2011) Structural, mass, and elemental analyses of storage granules in methanogenic archaeal cells. Env. Microbiology. 13(9): 2587–2599
2. Buehler, D.C., Toso, D.B., Kickhoefer, V.A., Zhou, Z.H., and Rome, L.H. (2011) Vaults engineered for hydrophobic drug delivery. Small. 7(10): 1432-1439.
3. Faller, M., Toso, D., Matsunaga, M., Atanasov, I., Senturia, R., Chen, Y. Zhou ZH, Guo F. (2010) DGCR8 recognizes primary transcripts of microRNAs through highly cooperative binding and formation of higher-order structures. Rna. 16(8): 1570-1583.
4. Slaymaker IM, Fu Y, Toso DB, Ranatunga N, Brewster A, Forsburg SL, Zhou ZH, Chen XS. (2013) Mini-chromosome maintenance complexes form a

filament to remodel DNA structure and topology. Nucleic Acids Res. 41(5): 3446-56

5. Xiao, Q., Sohn, H., Chen, Z., Toso, D., Mecklenburg, M., Zhou, Z.H., Poirier, E., Dailly, A., Wang, H., Wu, Z., Cai, M., Lu, Y. (2012) Mesoporous metal and metal alloy particles synthesized by aerosol-assisted confined growth of nanocrystals. Angew Chem Int Ed Engl. 51(42): 10546-50

PRESENTATIONS

CSMM SYMPOSIUM, March 4th 2009

UCLA – Poster Presentation

ADVANCED ELECTRON MICROSCOPY IN NANOMEDICINE SYMPOSIUM, Oct. 2nd – 3rd, 2009

UCLA – Poster Presentation

CNSI EAB MEETING, July 19th 2011

UCLA – Poster Presentation

MIMG RETREAT, September 20th 2011

UCLA - Poster Presentation

SCSMM SYMPOSIUM, March 3rd 2012

Caltech - Oral Presentation

CFAR SEMINAR, January 29th 2013

UCLA – Oral Presentation

SCSMM SYMPOSIUM, March 30th 2013

UCLA – Poster Presentation,

Chapter I

Introduction

ARCHAEA

The Archaea constitute one of the three domains of life, the others being the Eukarya and Bacteria. Archaea were once classified as part of the domain of Bacteria as they are both comprised of single-celled organisms without nuclei or membrane-bound organelles, however, with increasing phylogenetic data, it became apparent that there are several key differences in evolutionary history and biochemistry between the two groups of organisms and Archaea were reclassified as the third domain of life (Woese et al., 1990). There is some debate about the evolutionary relationship among the three domains, but the archaeans and eukaryotes are often described as having diverged from a common ancient ancestor, which may have evolved from bacteria, and thus can be classified together in a super domain known as neomura, meaning new walls due to the evolutionary replacement of peptidoglycan cell walls with other glycoproteins (Cavalier-Smith, 2002). In fact, it has been shown that the Archaea share genetic similarities with both the Bacteria and Eukarya, with metabolic pathways, including metabolic enzymes, metabolite uptake systems, enzymes for cell wall biosynthesis and others, being more related to Bacteria while gene expression pathways, including translation & transcription, chromosome replication, and protein secretion, are more closely related to Eukarya (Koonin et al., 1997). Archaea were originally viewed as exclusively extremophiles, living only in locations such as hot springs, salt lakes or acidic water found in caves, but are now recognized to exist in a diverse range of environments, from soils, oceans, and marshlands to inside the human body (Robinson et al., 2005). However, despite their ubiquitous presence, Archaea have not been studied nearly to the same extent as Eukaryotes or Bacteria and extensive structural studies, in particular, are lacking.

Archaeal classification

Most of the known Archaea are currently divided among two main phyla: the *Euryarchaeota* and the *Crenarchaeota,* with a third phylum, the *Thaumarchaeota* more recently classified (Brocher-Armanet et al., 2008). There are several other potential phyla, such as the Nanoarchaeota, Korarchaeota, Aigarchaeota, and Geoarchaeota awaiting confirmation (Barns et al., 1996; Huber et al., 2002; Kozubal et al., 2013; Nunoura et al., 2011). Species are classified together based on common ancestors and shared structural features as well as the use of the sequence of ribosomal RNA genes, which was first pioneered by Carl Woese (Woese and Fox, 1977). As species are discovered that do not fit with the current classifications, new classifications are proposed, and, as there are many as yet uncharacterized archaeons, the classification system is constantly in flux.

Archaeal structural similarities and differences with bacteria

Archaea, in general, are similar in cell structure to bacteria, but differ in some crucial aspects of the makeup and arrangement of their outer structures. Organisms from both domains lack internal membranes and membrane-bound organelles, and organisms from both domains are usually bounded by cellular envelopes and use flagella for motility (Thomas et al., 2001). One aspect of archaeal morphology that is distinctive is the molecular makeup of their membranes, which provides evidence for their evolutionary separation (Koga and Morii, 2007). The membranes of archaea are mainly composed of glycerol-ether lipids, as opposed to the glycerol-ester lipids common in the membranes of bacteria and eukaryotes. The ether bond is chemically more resistant than the ester bond, which may help archaea survive in the harsh environments inhabited by some species, such as the acidophiles, alkalilphiles, and thermophiles (Albers et al., 2000). Additionally, the fatty acid chains of archaeal membrane lipids can contain multiple side-branches and even cyclic rings, as opposed to the straight chains found in other organisms (Damsté et al., 2002). This adaptation provides further

protection for thermophiles by preventing membrane leakage at high temperatures (Koga and Morii, 2005). One final membrane distinction is the alteration of the lipid bilayer to a monolayer in some archaea species. These monolayers are created by the fusion of the hydrophobic tails of two phospholipids producing lipids with two polar heads and a non-polar connecting region, which increases rigidity and may aid in survival in harsh environments (Hanford and Peeples, 2002). In regard to cellular envelopes, archaea are often bounded by a surface layer or S-layer composed of a rigid paracrystalline protein array, which provides chemical and physical protection. The S layer of archael cells usually have hexagonally ordered lattice symmetry made up of many single protein monomer subunits held together by noncovalent bonds. In contrast to bacteria, this S-layer is never composed of peptidoglycan (Kandler and König, 1998). Archaeal flagella function similarly to bacterial flagella, with an extended filamentous structure that is driven by proton-gradient powered rotary motor proteins (VanDyke et al., 2008). However, the composition and assembly of archaeal flagella are quite distinct from bacterial flagella, as they are composed of unique flagellin proteins, are much thinner in diameter, and assemble from the base rather than the distal end (Bardy et al., 2003). It has also been postulated that archaeal flagella are actually related to the bacteria type IV pilus system due to the similarities in filament structure, gene sequence, homologous proteins, and mode of assembly between the two systems (Ng et al., 2006).

Archaeal reproduction

Archaea reproduce by binary fission, simply dividing and passing on an identical set of genes to each daughter cell. This is controlled in a cell cycle, whereby cell division can be broken down into a series of stages: cell growth (G1), chromosome replication (S), further cell growth (G2), genome segregation (M), and finally cell division (D) (Lindås and Bernander, 2013). Archaea are known to utilize DNA replication proteins that are more similar to eukarya than bacteria, including DNA polymerase, helicase, and the origin replication complex. Furthermore, it has

been found, in certain archaeal species, that chromosomes can replicate from multiple origins of replication as is common among eukaryotes (Kelman and Kelman, 2004). Conversely, the cell division regulation proteins that form the contractile ring during cytokinesis and regulate septum formation, which includes FtsZ in the *Euryarchaeota,* are more similar to their bacterial homologs (Bernander, 1998). Recently, a unique mechanism for cellular division has been described in crenarchaeotes, which involves Cdv proteins forming contractile ring-shaped structures (Lindås et al., 2008; Samson et al., 2008). Cell division was examined in the euryarchaeotes *Methanospirillum hungatei* and *Archaeoglobus fulgidus* by cryo ET to gain an understanding of the structural changes that occur during division and a complete description of this process can be found in Chapter IV.

Archaeal extremophiles

Many archaea are extremophiles and thrive in harsh environments, such as very high temperatures, high salt, extremes of pH, and anaerobic surroundings (Pikuta et al., 2007). These extremophilic archaea can be classified into four main groups: thermophiles, halophiles, alkaliphiles, and acidophiles. Thermophiles grow best at high temperatures, usually above 45^{o}C (113^{o}F) and hyperthermophiles grow at even higher temperatures, usually above 80^{o}C (176^{o}F). Halophiles live in extremely saline conditions such as are found in salt lakes. Alkaliphiles and acidophiles thrive in very basic or acidic environments, respectively, and one species has even been shown to grow at pH 0 (Ciaramella et al., 2005). The ability to thrive under extreme stresses seems to have been an evolutionary adaptation for archaea and may be a competitive advantage under variable environmental conditions (Valentine, 2007). Studying how these organisms have adapted to their harsh environments can give us insight into cell survival under extreme conditions and may even be more broadly applicable to studying cell survival in extraterrestrial environments.

Archaeal ecological impact

Archaea have an important role in recycling certain elements, such as carbon, nitrogen, and sulfur, in their environment, which is crucial for ecosystem vitality, however, they can also contribute to pollution. Many archaeons take part in the nitrogen cycle, some performing actions such as nitrate respiration and denitrification that remove nitrogen and others carrying out reactions such as nitrate assimilation and fixation that introduce nitrogen, which is even found to occur at extreme temperatures (Cabello et al., 2004; Mehta and Baross, 2006). Furthermore, archaea have been found to be involved in ammonia oxidation, crucial for nitrification and the nitrogen cycle overall, in both the ocean and the soil, further indicating their importance in these ecosystems (Coolen et al., 2007; Francis et al., 2007; Leininger et al., 2006). The sulfur cycle involves several steps which, generally, can either produce sulfide from reduction of sulfate or produce sulfide from oxidation of sulfate, with elemental sulfur intermediates. Archaea can be involved in either direction of the reaction, but when organisms that oxidize sulfur to sulfate accumulate, such as in an abandoned mine, large amounts of sulfuric acid can be produced and lead to acid mine drainage or other environmental problems (Baker and Banfield, 2003). Lastly, methanogens contribute to the carbon cycle by breaking down organic waste in anaerobic ecosystems (Schimel, 2004). Unfortunately, methane is a very abundant greenhouse gas in the atmosphere and the methanogens contribute a vast amount of atmospheric methane through their metabolic processes, thereby contributing to the buildup of greenhouse gases and global warming, unless the released methane can be utilized as a biofuel (Parawira et al., 2008).

Archaeal applications in biotechnology

The extremophiles which are resistant to heat or extremes of pH are particularly useful as sources of enzymes that remain functional under these harsh conditions (Egorova and Antanikian, 2005). Enzymes that remain active and non-denatured under extreme conditions of temperature and acidity have a wide variety of applications in industry. Also, their stability under

harsh conditions makes them attractive for studying homologous enzymes in bacteria and eukaryotes. In addition, methanogenic archaea are used for sewage treatment both for anaerobic digestion of biomass and for biogas production (Schiraldi et al., 2002). Acidophilic archaea have also been used for extracting metals, such as gold, cobalt and copper from ores (Norris et al., 2000). Archaea produce antimicrobial agents that have the potential to be utilized for antibiotic treatment, with many yet to be discovered (Shand and Leyva, 2008). With further study of their unique properties, new and innovative applications for archaeal biological processes are sure to be discovered.

ELECTRON MICROSCOPY TECHNIQUES

Several different electron microscopy techniques were utilized during these studies of archaeal cells. The main techniques used were cyro electron tomography (cryo ET), scanning transmission electron microscopy (STEM), and energy dispersive X-ray (EDX) spectroscopy.

Cryo electron tomography (cryo ET)

CryoET is an important tool in structural microbiology research because it enables visualization of complexes in a cellular environment and at a molecular resolution. It is a three-dimensional (3D) imaging technique in which electron microscopy tomographic imaging is performed on cryogenically cooled, vitrified specimens after which the object is computationally reconstructed.

Before a sample can be imaged, it must be frozen in vitrified ice. This is achieved by rapidly freezing the sample in a cryogen, often liquid ethane that is cooled by liquid nitrogen to near its freezing point, around 100 K. The sample is deposited onto an electron microscope grid covered by holy carbon, which allows sample to freeze in a thin film of ice within the holes of the carbon layer for imaging without interference from the carbon film. The sample is then blotted down to a thin film before plunging into the cryogen (Fig. 1-1A). The cryogen freezes the water around the sample so rapidly that it does not have a chance to crystallize and remains in an amorphous state as vitreous ice. The frozen water essentially fixes the sample in its native, hydrated state in solution (Dubochet et al., 1988). Once the sample is frozen, it must remain cooled in liquid nitrogen at all times, as warming would allow crystallization that would essentially ruin it for imaging.

The principle behind three dimensional imaging by electron tomography is the same as that used in computerized axial tomography with x-rays. Basically, a series of projection images of a specimen are collected by varying its orientation over a certain range with respect to the incident electron beam. Usually this is accomplished by tilting the sample around a set axis to create a tilt series. Each projection image contains all of the three-dimenstional information

about the sample compressed along the axis of the incident beam into a single plane. Therefore, the original three dimensional objects can be recovered by computationally combining the information in the tilt series (Fig. 1-1B).

To get the most faithful reconstruction of the three dimenstional structure of the original object, the acquired tilt series must first be well aligned. During tomography tilt series collection, it would make the process prohibitively time consuming, and may not even be possible, to perfectly align each image before acquisition. Therefore, the alignment must be performed on the acquired tilt images. This is accomplished by calculating and correcting the shifts between each image in the tilt series and correcting any orientational discrepencies of the images from the tilt axis. Coarse shift alignment can be done by cross-correlating the Fourier transform of successive images in the tilt series and correcting the measured shifts. Fine shift alignment can be done most easily with fiducial marker tracking. Gold nanoparticles are often used as fiducial markers for cryo ET, as they have a very high contrast, do not usually disrupt the sample, and can be distributed easily and evenly in solution. Essentially, the gold markers are tracked between successive tilt images and any remaining shifts are corrected. Another method is by breaking up the tilt images into patches and using cross-correlation of each small patch region as a fiducial model. However, due to the low contrast in cryo ET images, this is often not feasible. Optimal reconstruction also requires the tilt axis to have a known orientation in each image so that the backprojection plane can be properly calculated. The tilt axis angle is measured during calibration of the microscope, and then each image can be rotated to orient the tilt axis vertically. If there is a discrepancy, the angle should be recalculated by recalibration of the instrument. Once the tilt series has been well aligned, with a vertically positioned tilt axis, it is ready for reconstruction.

In order to recover the three dimensional information into a tomogram from the series of projection images, the main principle is to do the inverse of the process that generated the projection images. Essentially, you are back projecting the image along the direction that the

projection was acquired. The three dimensional volume can be attained by combining these back projection profiles from each image that was taken along a different orientation. The distribution of the density in the superimposed reconstruction is proportional to the distribution of the density of the original object that was imaged. This reconstruction process, as well as the alignment procedures, can be executed automatically by one of several available software packages such as IMOD (Kremer et al., 1996).

One of the inherent limitations of electron tomography is that the sample cannot be viewed from every possible orientation. The physical limitations of the microscope do not allow the sample to be tilted a full 90 degrees in each direction because the beam becomes blocked by part of the grid or grid holder. This leads to a volume in the backprojection reconstruction that lacks projection data, and which is shaped like a wedge due to the angles being excluded during tilt series acquisition, thus this region is often termed the ‘missing wedge’. This missing wedge causes the three dimensional information within the missing region to be essentially lost, thus structures above and below the central plane of the reconstruction are often poorly resolved.

Another limitation is due to the low signal to noise ratio (SNR) in cryo ET images. Samples being imaged by cryo EM can only receive a certain amount of dosage from the electron beam before the radiation from the high energy electrons causes permanent structural damage. Thus, cryo EM images have to be acquired at a low dose of electrons and this increases the amount of noise present in the images. For cryo ET, the same region of the sample is imaged multiple times, often over 100 times, so the electron dosage applied to the sample has to be distributed among all of the tilt images and, consequently, each image must be acquired at an even lower dosage. This causes cryo ET images to have an even higher amount of noise and greatly limits the level of resolution and contrast that can be achieved. Contrast limitations due to the low dosage are compensated for, to some degree, by underfocusing the images by several microns.

Scanning transmission electron microscopy (STEM)

STEM imaging is distinct from conventional transmission electron microcopy (TEM) in that the electron beam is focused to a fine probe, which is then raster scanned over the sample to produce images. STEM instruments are usually a combination of a conventional TEM instrument with additional scanning coils, detectors and other equipment, which allows the beam to be focused to a probe and the desired signals to be detected. This also provides the instrument with the versatility to switch between imaging modes.

The signal in STEM dark-field imaging is acquired on an annular dark-field (ADF) detector, upon which only highly scattered electrons will be collected, the unscattered or weakly scattered electrons will pass through undetected (Fig. 1-2). By utilizing a high-angle ADF or HAADF, only the highest angle, incoherently scattered electrons will be detected, and the images produced will be highly sensitive to variations in the atomic number of the atoms in the sample being scanned, often called Z-contrast images (Jesson and Pennycook, 1995). Because of the sensitivity of the imaging technique to atomic number in the sample, it can be utilized to directly measure the mass of the sample being imaged (Muller and Engel, 1998). STEM imaging also has been shown to have unique applications for imaging biological complexes (Wall and Simon, 2001). It has advantages over conventional TEM in that it does not require staining or fixation to provide high contrast images for small objects and can resolve samples, such as DNA, that other EM techniques cannot without treatment of the sample.

Energy dispersive X-ray (EDX) spectroscopy

EDX spectroscopy is a technique in which a sample is exposed to an excitation source and, simultaneously, the characteristic X-rays released are measured, which provides information about the elemental composition of the sample. In regards to EDX with electron microscopy, the source of excitation is the electron beam and an energy dispersive spectrometer that can detect the X-rays emitted from the sample is installed in the column of the microscope (Fig. 1-2). This

allows simultaneous imaging and elemental composition determination of samples by scanning electron microscope (SEM), TEM, or STEM instruments. When using a STEM instrument, the ability to scan and localize the probe on the sample while collecting spectra provides additional utility and can provide highly resolved elemental information, depending on the size of the electron probe. Individual, small points within the sample can have their spectrum examined, spectra can be acquired across a line to create an elemental profile, and two-dimensional scans over specific areas of the sample can be acquired to provide elemental maps.

The principle behind EDX spectroscopy is that each element has a characteristic atomic structure that will have a characteristic X-ray emission signal upon excitation (Agarwal, 1991). The structure of the atom is arranged with negatively charged electrons orbiting the positively charged protons within the nucleus. The number of orbital electrons, for unexcited atoms, is characteristic and should be equivalent to the atomic number Z (the number of protons in the nucleus). The electrons are arranged at discrete orbital states that have specific energy levels and the orbital states are filled from lowest to highest energy level, with the lowest energy states filled first. The orbitals are designated K, L, and M, from lowest to highest energy state. The K level has one orbital, the L has three, and the M has five. Each orbital can contain two electrons. When the atom is excited by an excitation source, such as an electron beam, electrons from the lower energy orbitals can be ejected. An electron then drops down from a higher energy orbital to fill the vacancy left at the lower energy orbital. During this process, the electron must lose energy equivalent to the difference in energy between the two orbital states, this energy is released in the form of an X-ray photon (Fig. 1-3). Because the energy levels are discrete and characteristic for each element, the X-rays released have characteristic energy levels. Therefore, the energy dispersive spectrometer records the number of X-rays emitted at each energy level and outputs a spectrum that gives a description of the elemental composition of the sample (Goldstein, 2003).

PREVIOUS STUDIES INVOLVING ELECTRON TOMOGRAPHY

Several other projects, not involving archaeal cells, were also carried out during my doctoral studies. I have provided a brief description of some of these studies, which demonstrate the variety of uses for electron tomography (ET) and cryo ET in structural studies of both biological and inorganic samples.

ET of DGCR8 protein complex

MicroRNAs (MiRNAs) are short nucleic acids, only about 22 nucleotides long, which are involved in the regulation of gene expression through translational repression and mRNA degradation (Filipowicz et al., 2008). The RNA binding protein, DiGeorge critical region 8 (DGCR8), also known as Pasha, is required during the maturation process of miRNAs from their extended primary transcript form (pri-miRNA). During the cleavage of the pri-miRNAs by the Drosha nuclease, the DGCR8 protein must recognize and bind to the pri-miRNAs, and together Drosha and DGCR8 form the Microprocessor complex (Denli et al., 2004).

In collaboration with Dr. Michael Faller, the 3D structure of DGCR8 proteins in complex with a double-stranded pri-miRNA hairpin (pri-mir-30a) was examined by ET to determine the binding configuration. DGCR8-pri-mir-30a complex samples were deposited onto carbon coated grids and stained using 2.5% uranyl acetate. Tomography tilt series were collected using a 200kV Tecnai F20 instrument and processed to produce 3D reconstructions of the protein particles (Fig. 1-4). The particles were then classified according to shape and size and the best were aligned and averaged together to create a 3D model of the protein complex (Fig. 1-5). It was determined that the structure could contain three DGCR8 dimer subunits, which supported the biochemical data that suggested a cooperative, trimeric binding process (Faller et al., 2010).

Cryo ET of vault particles

Several different studies were carried out in collaboration with members of the Rome lab at UCLA. Each of these studies involved cryo ET imaging of modified vault particles, which the

Rome lab provided. The vault particle is a large ribonucleoprotein complex of unknown function, which is expressed in the cells of most eukaryotes, including humans. Vaults form a large nanocapsule with a barrel-shaped structure that tapers at the top and bottom and contains a large, hollow interior. Vaults, *in vivo*, are composed of multiple copies of the major vault protein (MVP) with associated minor vault proteins, VPARP and TEP1, as well as small vault RNAs (vRNA) (van Zon et al., 2003). It was discovered that vault-like particles could be assembled *in situ* by expressing only MVP in insect cells, which do not express endogenous vaults (Stephen et al., 2001). The studies described used vault particles produced in insect cells and composed of MVP modified with a cysteine rich peptide at the N-terminus (CP-MVP) unless otherwise noted.

Initially, cryo ET was performed to localize the int protein packaged in vault particles. The int protein is the binding domain of VPARP, the minor vault protein known to associate with MVP. First, vault particles were imaged on their own by cryo ET. The characteristic vault particle shape and empty interior is shown in the three-dimensional reconstruction (Fig. 1-6A). Next, vault particles mixed with int protein were imaged by cryo ET. Slices from the 3D reconstruction show extra density near the mid-barrel region indicating clearly that the int protein has been packaged inside of the vault particles (Fig. 1-6B).

The structural features and biocompatibility (they are expressed normally in all human cells) of vault particles make them a candidate for development into a drug delivery vehicle, and several studies were performed examining the potential for drug packaging within vault particles. In the first study, a lipid nanodisk was packaged in vault particles and imaged by cryo ET (Buehler et al., 2011). Extra density can clearly be seen within the vault particles in the 3D reconstructions (Fig. 1-6C). Particles were segmented from the tomograms and rendered to show the location of the lipid disk within the vault particle in three dimensions (Fig. 1-6D). In the second study, vault particles were modified by adding an AH1Z membrane anchor domain at the N terminus of the MVP proteins, hoping to bind lipids at the waist region of the vault in which

lipid soluble drugs could be packaged. Cryo ET reconstructions clearly show additional density at the waist of the vault particles when examining them in cross-section, indicating that lipids had been bound by the anchor domain (Fig. 1-6E). Particles were also segmented to visualize the packaged vaults in three dimensions (Fig. 1-6F). A manuscript including this data is currently being prepared for submission by Dr. Daniel Buehler et al.

In the final study, vaults particles were modified by mutating residues 3-8 near the N-terminus of MVP to histidine, termed 6-His-MVP. This was done to examine the effects this has on vault formation *in situ*. It was discovered that the vault particles failed to form normally, but instead formed large coiled structures composed of many copies of 6-His-MVP in long chains. This was visualized in three dimensions by cryo ET (Fig. 1-6G). A manuscript including this data is currently being prepared for re-submission by Dr. Jan Mrazek et al.

ET of MCM filaments

As noted above, the Archaea and Eukaryotes have a very similar chromosomal DNA replication pathway, which includes sharing the use of the mini-chromosome maintenance (MCM) proteins to unwind DNA. During the replication process, MCM forms a ring complex that acts as an ATP-dependent DNA helicase to unwind the genome, opening double-stranded DNA into single-stranded DNA templates.

In collaboration with Ian Slaymaker, I examined MCM filament formation by TEM and ET in order to examine the filament's helical nature, for use as a comparison with his crystal structure, and to visualize MCM binding DNA. Multiple archaeal MCM filament samples were created *in vitro* by combining DNA segments with MCM protein and alba (chromatin protein) in various concentrations and buffer conditions. The resulting filament samples were placed on grids and stained using 2.5% uranyl acetate. They were imaged in a 200kV Tecnai F20 instrument and tomography tilt series were acquired. The tilt series were used to reconstruct the filaments in three dimensions and models were constructed to analyze the helical structure of

the filaments (Fig. 1-7A) and examine how the DNA strand is packaged within (Fig. 1-7B). Additionally, wild type MCM filaments (Fig. 1-7C) and α5 mutant MCM filaments (Fig. 1-7D) were compared by TEM. It was observed that the wildtype filaments were 175 Å in diameter, similar to the cystal structure, but the mutants that could not induce supercoiling of the DNA produced filaments that were only 125 Å in diameter (Slaymaker et al., 2013).

ET of metal nanoparticles

ET can also be applied to materials science to study the three dimensional architecture of nanomaterials. In collaboration with Dr. Qiangfeng Xiao, mesoporous metal nanoparticles composed of nickel and carbon were imaged by ET and 3D arrangement of the nickel networks was elucidated (Xiao et al., 2012). Nickel nanoparticles were deposited onto carbon coated grids and imaged by ET using a 200 kV Tecnai F20 instrument. Tilt series were acquired and processed to create three-dimensional reconstructions of the nanoparticle structure. The 3D density maps were segmented and analyzed to examine the internal architecture of the pores within the particles as well as the transition between nickel and carbon within the particles determined by variations in density (Fig. 1-8).

SIGNIFICANCE

The Archaea in general have not been characterized structurally to the extent that prokaryotic and eukaryotic organisms have been, and this study should contribute to strengthening our knowledge about this important class of organisms.

Preference for cryo EM & ET for visualizing whole cells

The focus of this study was the characterization, by cryo electron microscopic techniques, of whole cells of the archaea *M. hungatei* and *A. fulgidus*. The main reason for utilizing cryo electron microscopy versus traditional transmission electron microscopy using plastic embedding, sectioning, and staining is the preservation of the sample in a layer of vitrified ice. Rapid freezing of the sample keeps it maintained in its hydrated state in solution, avoiding artifacts caused by dehydrating the sample, adherence of the sample to a surface, or fixation of the sample in a plastic or resin material. Also, the sample is left unstained so the images obtained are of the actual proteins, lipids, and other biological materials that comprise the sample rather than of a heavy metal coating on the surface. To avoid crystallization of the water in the sample buffer, the samples are first blotted to maintain a thin layer (< 1 μm) of solution before being rapidly frozen by plunging into liquid ethane cooled by liquid nitrogen to temperatures in the range of -180ºC (near the freezing point of ethane). Rapidly freezing the samples prevents the transition of the ice into a crystallized state and it instead remains in an amorphous vitrified state. The use of cryoprotectants such as glycerol to aid in maintaining a vitrified state is unsuitable for cryo electron microscopy due to the adverse effects on imaging of the frozen samples. Thus, using a thin layer of solution and imaging only sufficiently thin samples are requirements to ensure vitrification of the entire volume during the freezing process.

By comparing the results of conventional versus cryo techniques for *M. hungatei* it becomes immediately apparent why cryo imaging is preferred (Fig. 1-9).The negatively stained

cells have dried, collapsed, and flattened somewhat, distorting their natural morphology and most likely damaging the structure of the cell (Fig. 1-9A-C). The cells imaged in vitreous ice show the normal morphology of tubular cells that maintains the proper shape and structure, also the surface layers and interior structures are much more clearly visualized and apparent in the cryo electron images (Fig. 1-9D-F).

Preliminary description of M. hungatei

M. hungatei is an anaerobic methanogen and is part of a class of organisms vital for anaerobic digestion of organic waste in the ecosystem. *M. hungatei* has a unique morphology with multiple external envelope layers including a paracrystalline S-layer immediately external to the plasma membrane and a rigid external layer that may encompass multiple cells. This most external envelope layer of *M. hungatei* is made up of many closely packed hoop-like structures that form an open-ended sheath structure, which differs greatly from a typical S-layer. It is complicated to examine the structure of the envelope S-layer due to the presence of the sheath and its difficulty of removal. In addition to the external envelope layers, the ends of each cell have a multi-layered plug structure, which is perforated to allow flagella to extend outward from individual cells into the external environment for motility (Fig. 1-10). Although previous studies have used conventional EM to examine the basic structure of this organism (Beveridge et al., 1985; Beveridge *et al.*, 1990; Beveridge *et al.*, 1991; Southam and Beveridge, 1992; Firtel *et al.*, 1993), a more thorough examination with the techniques of cryo EM and cryo ET were necessary to get a better understanding of the molecular structure of the various cell components described above as well as the structural changes that occur during cell division.

Chapter summaries

In Chapter II, a study is described that involved structural, elemental, and mass analysis of inclusion bodies discovered within *M. hungatei* cells. We visualized whole *M. hungatei* cells embedded in vitreous ice using cryo EM and observed dense granules located near the ends of

each cell. Using EDX spectroscopy, we discovered that the granules were composed of high concentrations of phosphorous and oxygen and were most likely polyphosphate bodies (PPBs). Then, by using STEM tomography and a mass standard in the form of tobacco mosaic virus particles, we analyzed the mass density of the granules and found them to be 3.8 g/cm^3, on average. Finally, by utilizing cryo ET we were able to visualize the whole cell in three-dimensions, which allowed us to localize the granules more precisely, and we observed that the dense PPBs localize near cell ends and the radial axis of the cell. By examining this unique intracellular feature of *M. hungatei* we have learned that the cells direct the accumulation of large amounts of phosphate, possibly for use as a high-energy storage system.

In Chapter III, the presence of inclusion bodies with *A. fulgidus* is examined. Whole cells containing multiple dense granules were examined in 3D by cryo ET, and the granules were found to be localized very close to the cell membrane. When analyzing the elemental composition of the granules by EDX spectroscopy, it was discovered that there were actually two distinct types of granules. One type was composed of high concentrations of phosphorous and oxygen, and were therefore determined to be PPBs as also found in *M. hungatei*. The other type of granule was composed of high concentrations of iron and sulfur, thus we termed them iron-sulfide bodies (ISBs). Both types of granules are found simultaneously within the cells. Again, we discovered that an archaean, *A. fulgidus*, directs the accumulation of mineral resources, in this case into two distinct high-density granules, for use as a energy storage medium.

In Chapter IV, the structure of growing and dividing cells is examined. We were able to visualize and study the process of cell division in *M. Hungatei* and *A. fulgidus*, which had not been fully characterized before. For *M. hungatei*, division occurs in the middle of the cell after it has undergone extensive growth, perhaps doubling in length. During cell division, the cells must undergo growth and fission at a central location, and this must involve a complicated process of reforming two entire multi-layered plug structures before a septum can be formed between the

two new cells, not to mention the enormous amount of energy and resources used to continually extend the sheath layer, which is formed completely external to the cell. The cell divides by constricting the membrane and then a new septum begins to form along with all of the components of the cell poles, including new plugs and the growth of new polyphosphate bodies. In *A. fulgidus*, division occurs by the formation of a depression followed by an invagination which extends deeper into the cell until it reaches the opposite membrane. By examining cells in the midst of division we analyzed the process from a structural standpoint and gained insight into how it occurs in these unique organisms.

Finally, in Chapter V, the future work, based on preliminary studies, is described. By further examining the structure of the sheath, S-layer, plug, and other components of the ultrastructure of *M. hungatei* and *A. fulgidus* to higher resolution, we will gain a better understanding of how this organism, as well as other Achaea, have adapted to their environments, which are often harsh in the extreme. These studies aim to utilize cryo EM and cryo ET to resolve the structural components of the cell by visualizing these structures in three-dimensions and utilizing techniques such as subtomogram averaging and helical reconstruction techniques to improve the resolution currently attained.

FIGURES

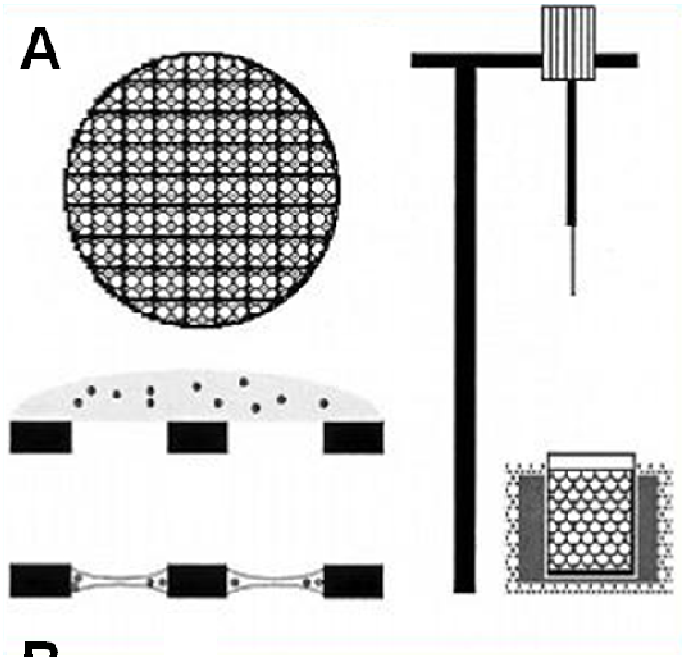
A

B

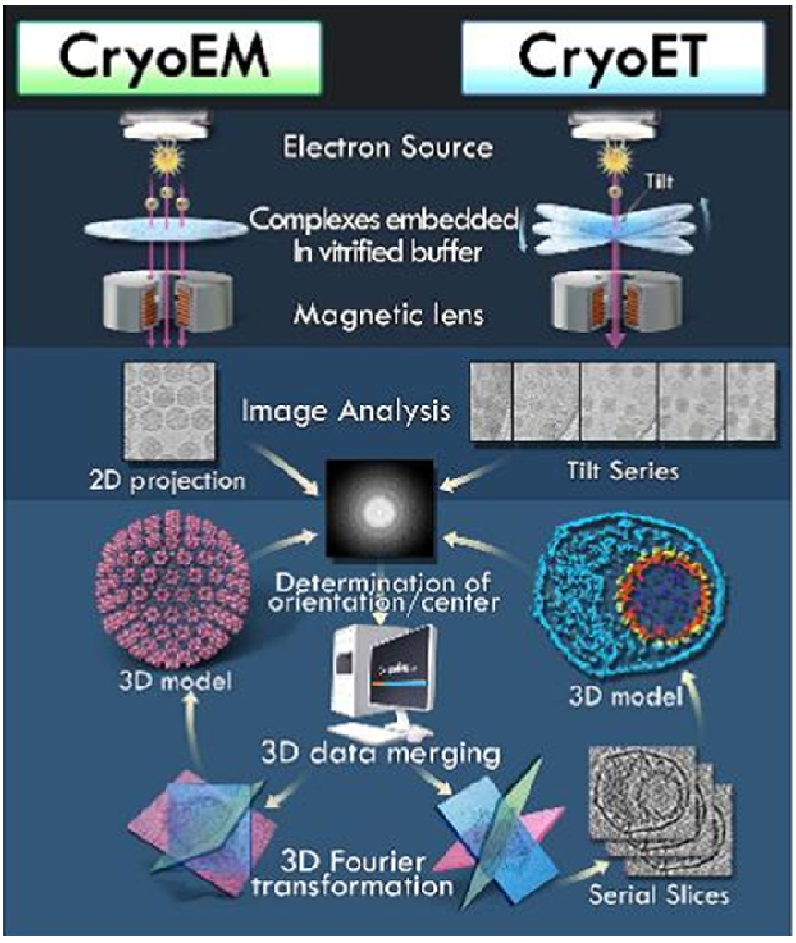
CryoEM
CryoET
Electron Source
Tilt
Complexes embedded in vitrified buffer
Magnetic lens
Image Analysis
2D projection
Tilt Series
Determination of orientation/center
3D model
3D model
3D data merging
3D Fourier transformation
Serial Slices

Fig. 1-1: (A) Representations of the holey grids used for cryo EM, a droplet of sample before and after blotting, and the plunge freezing apparatus. (B) A depiction of the procedures for cryo EM and cryo ET.

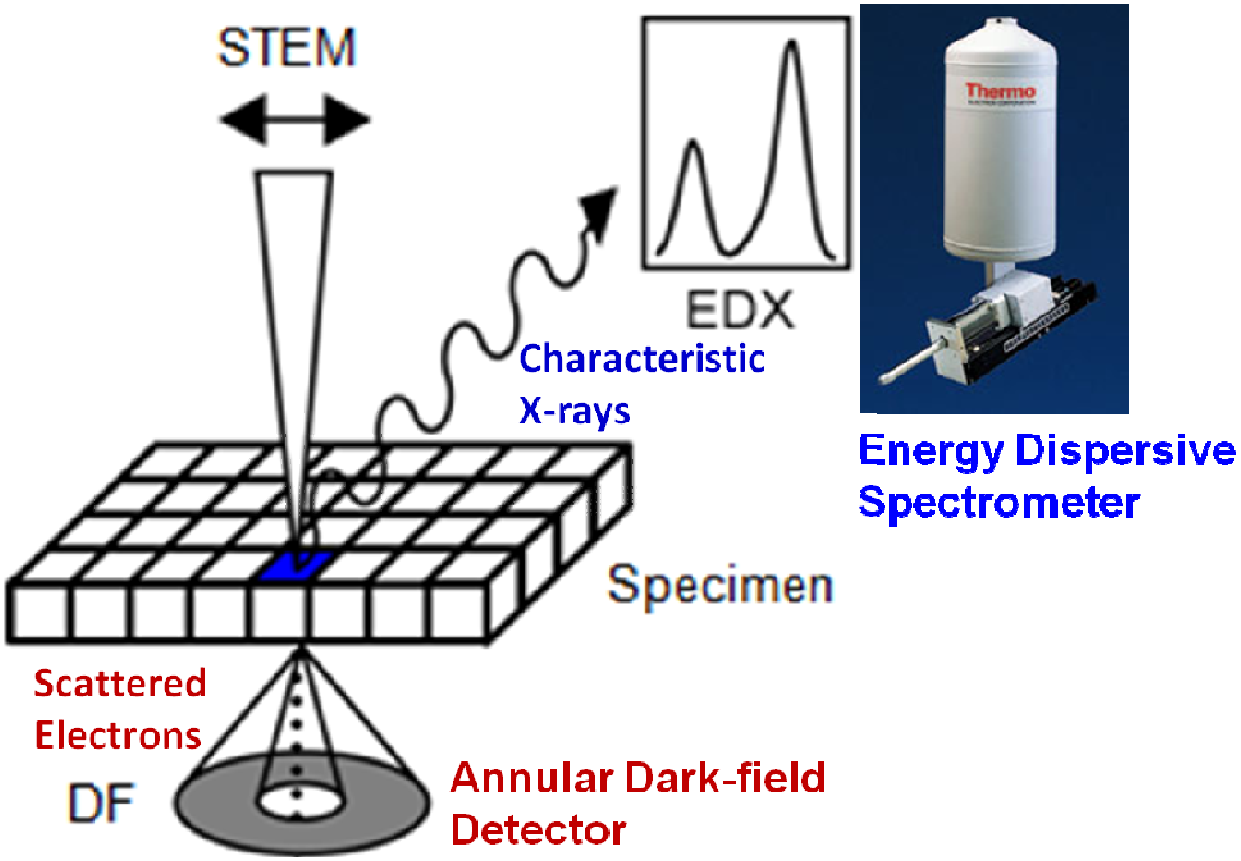

Fig. 1-2: STEM dark-field imaging and EDX spectroscopy. In STEM microscopy the electron beam is focused to a fine probe and raster scanned over the sample. The highly scattered electrons are detected by an annular dark-field detector to construct a STEM dark-field image. The characteristic X-rays released by excitation of the sample are detected by an energy dispersive spectrometer to determine the elemental composition of the sample.

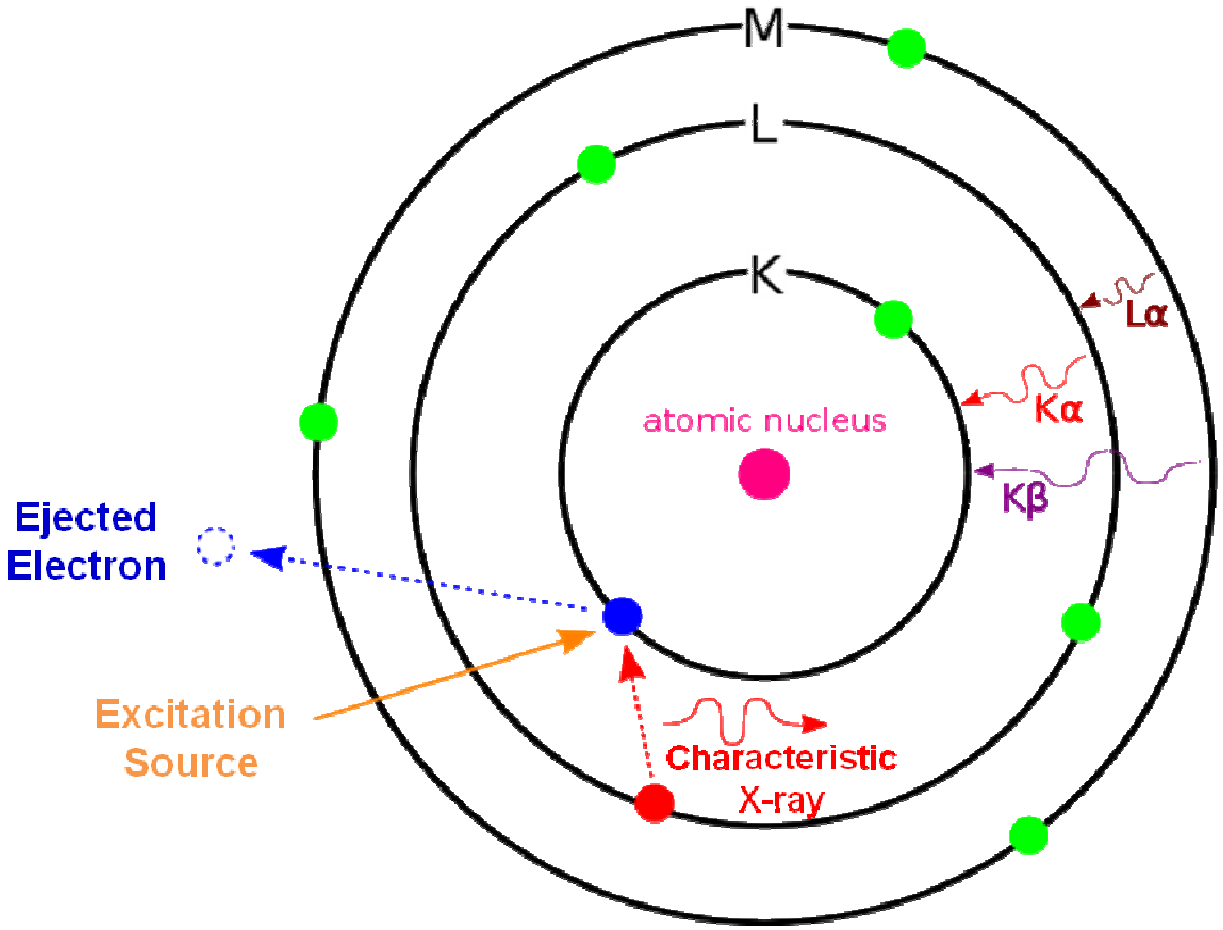

Fig. 1-3: The principle behind X-ray spectroscopy. The excitation source (orange) can cause a low-energy orbital electron to be ejected (blue). The vacancy is filled by a higher-energy orbital electron (red) and the difference in energy is released in the form of a characteristic X-ray.

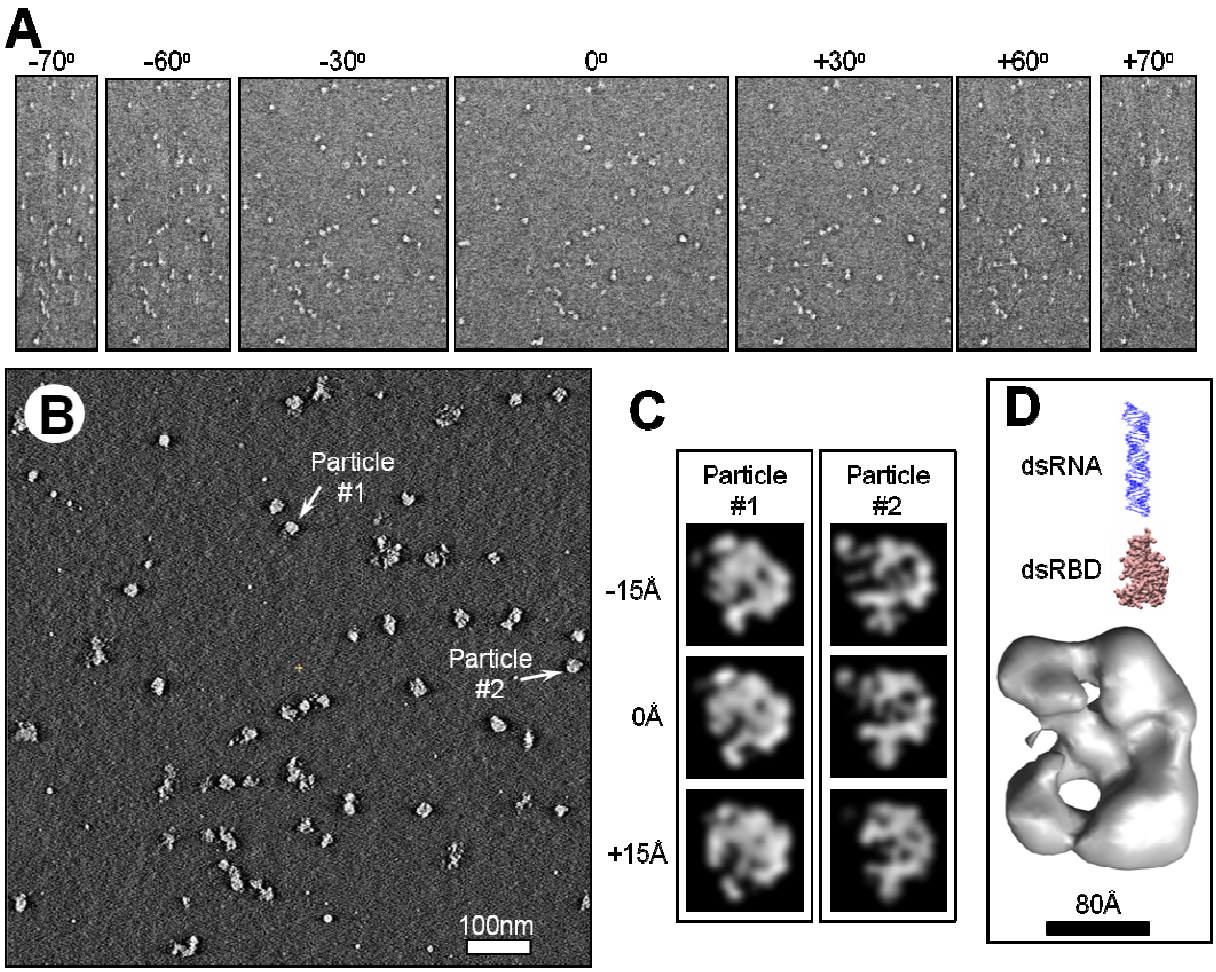

Faller, M., Toso, D. et al. (2010) *RNA* 16: 1570-1583

Fig. 1-4: Electron tomography of the DGCR8-pri-mir-30a complex. (A) Representative tilt images from a single tilt series, showing the sample imaged from -70°to +70°with a 1 ° tilt increment. (B) A slice through the 3D reconstruction made from the tilt series shown in *A* after alignment. (C) Selected particles were segmented out and low pass filtered to create particles suitable for averaging. Shown here are single pixel (7.4 Å) slices at three different z-heights of two different particles segmented from the reconstruction in *B* and aligned in three dimensions. Particles aligned this way were averaged together to generate an averaged 3D density map of the complex. (D) Surface representation of the averaged density map of DGCR8–pri-mir-30a

complex, compared with a model of the double-stranded region of miR-30a hairpin and the crystal structure of the double stranded RNA binding domain (dsRBD) of DGCR8.

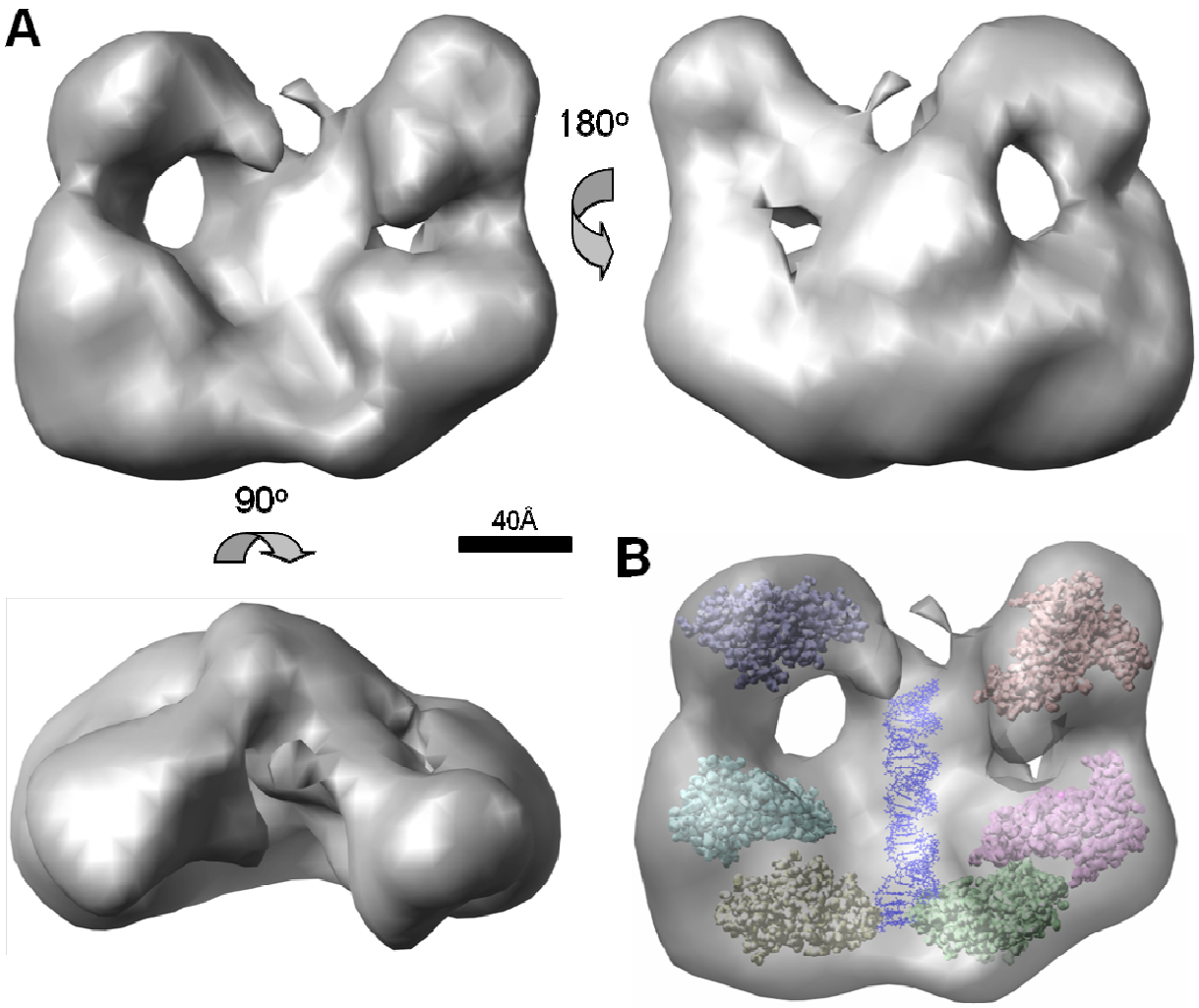

Faller, M., Toso, D. et al. (2010) *RNA* 16: 1570-1583

Fig. 1-5: Structural organization of the DGCR8–pri-mir-30a complex. (A) Surface representation of the averaged density map viewed in different orientations. (B) Plausible arrangement of protein molecules and RNA in the complex. We suggest that the RNA helix is located in the central region of the complex. Six copies of the crystal structure of DGCR8 dsRBDs are placed in the density, solely for the purpose of demonstrating that there is sufficient room in the electron density for three DGCR8 dimer subunits and the RNA strand.

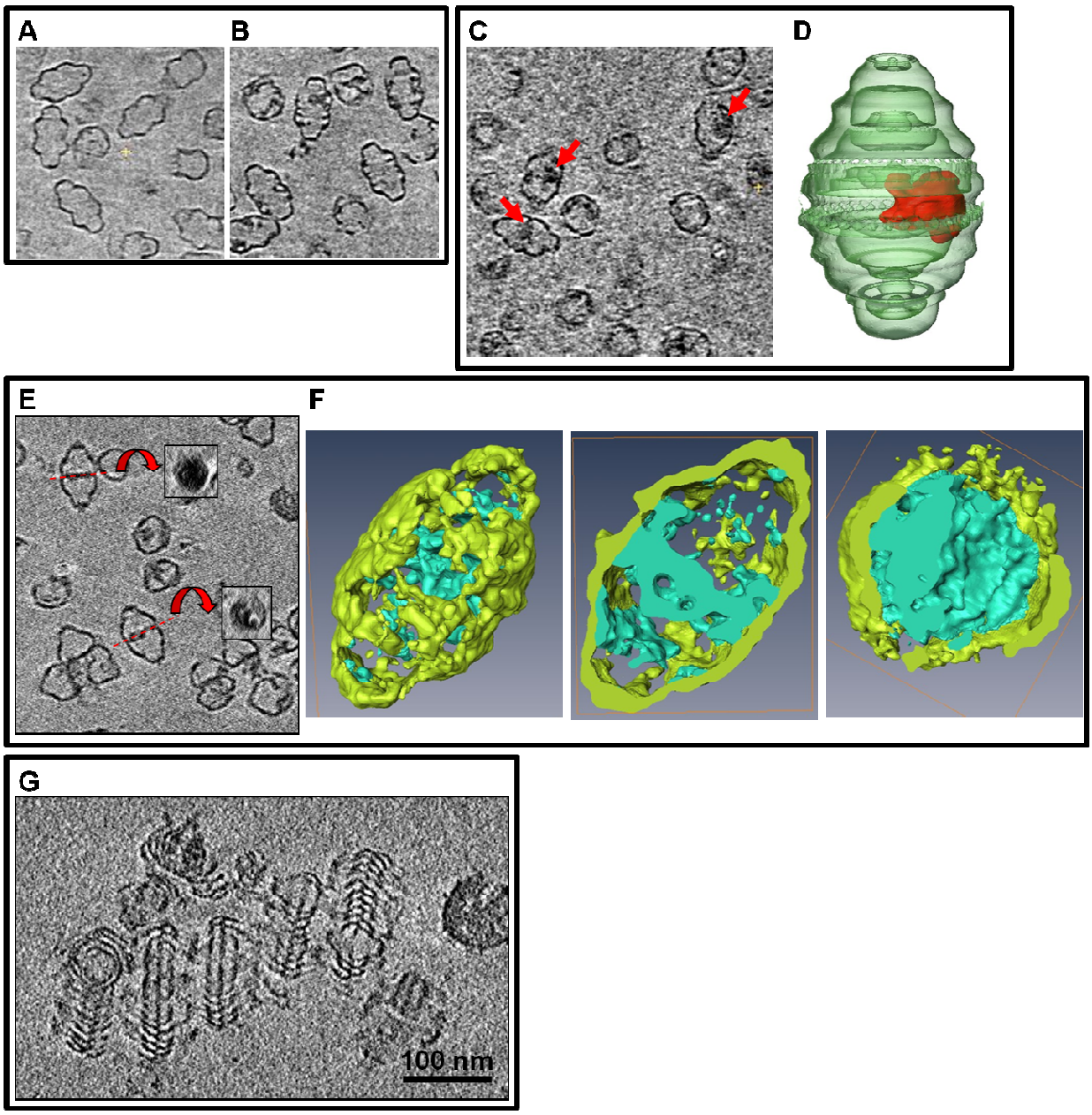

Fig. 1-6: Central slices from cryo ET reconstructions of frozen (A) cp2 vault particles, (B) cp2 vaults + int protein, the int proteins are shown decorating the vault in the mid-barrel region, (C) cp2 vaults + NDM lipid disks, the lipid disk densities are shown within the vaults, (E) cp2-AH1Z vaults, the AH1Z membrane anchor domain added to the N terminus is thought to bind lipid at the waist of the vault and extra density is clearly shown at this location (waist cross-sections are shown in insets), and (G) 6-His MVP rolls, the mutated MVP protein cannot pinch off to form

normal vault particles. (D) 3D segmented model of a vault particle packaged with lipid disk. (F) 3D segmented model of a whole cp2-AH1Z + int vault particle (left) with coronal (middle) and transverse (right) cross-sections.

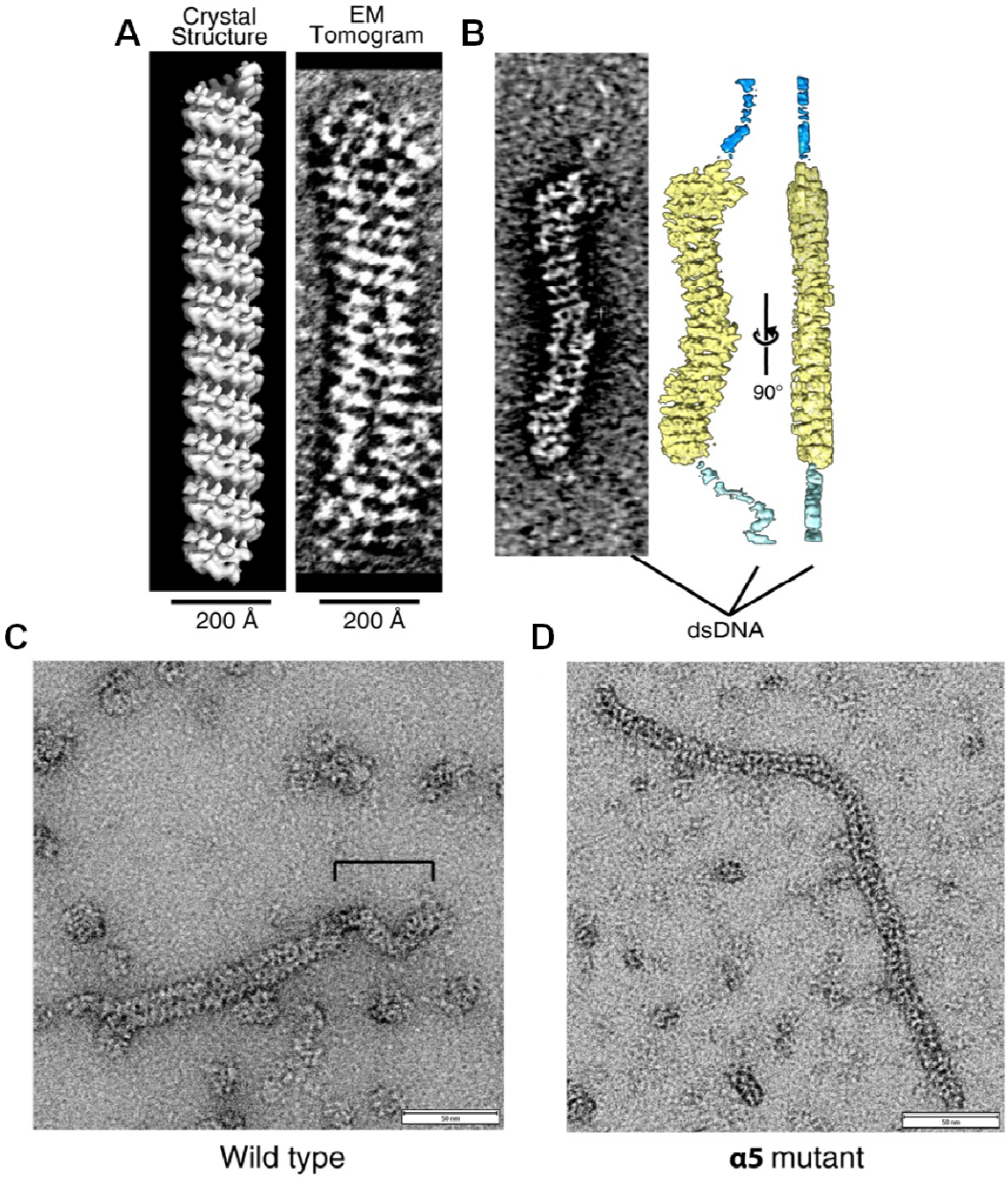

Slaymaker, I., Fu, Y., Toso, D.B. et al. (2013) *Nucleic Acids Res.* 41(5): 3446-56

Fig. 1-7: TEM imaging of MCM filament formation on dsDNA. (A) Side by side comparison of the MCM filament crystal structure filtered to 8Å and one reconstructed by ET. Superimposing the crystal structure with the ET tomogram shows well matched groove dimensions and helical handedness. (B) ET reconstruction of an MCM filament showing DNA protruding from the ends. Electron micrographs of (C) a wild type filament with 175Å diameter and (D) α5 mutant forming a filament with 125Å diameter.

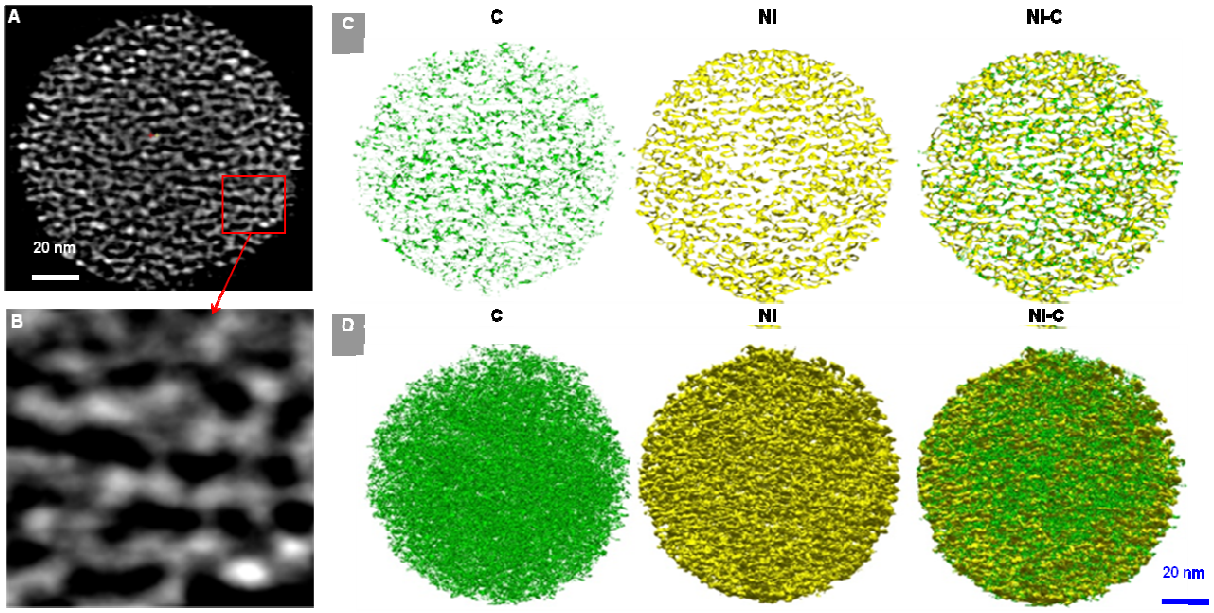

Xiao, Q., Sohn, H., Chen, Z., Toso, D. et al. (2012) *Angew Chem Int Ed Engl* 51(42): 10546-50

Fig. 1-8: (A) a cross-sectional image of a Ni particle via 3D tomogram showing density variation between the Ni framework and surrounding carbon layer. (B) Magnified image from (A) further revealing the formation of Ni nanocrystal networks within the particle. (C) Cross-sectional images of C (green), Ni (yellow) and their convolution of Ni and C mappings obtained by segmentation. (D) 3D volume reconstruction images of C (green), Ni (yellow), and convoluted 3D networks of Ni and C showing the unique mesoporous architecture.

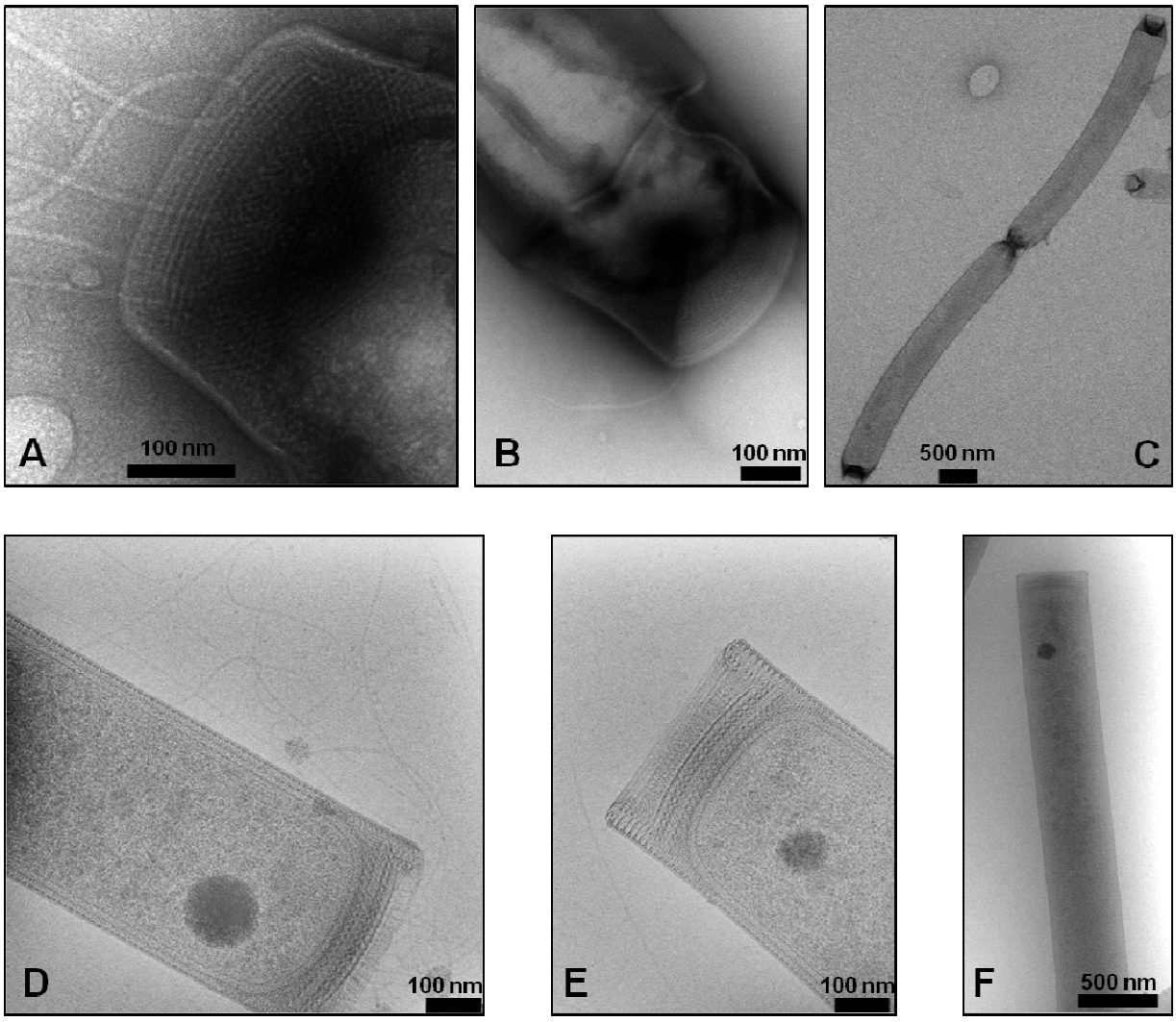

Fig. 1-9: Comparison of whole *M. hungatei* cells imaged by negative staining (A-C) versus cryo EM (D-F). The morphological changes induced by staining the cells are very apparent.

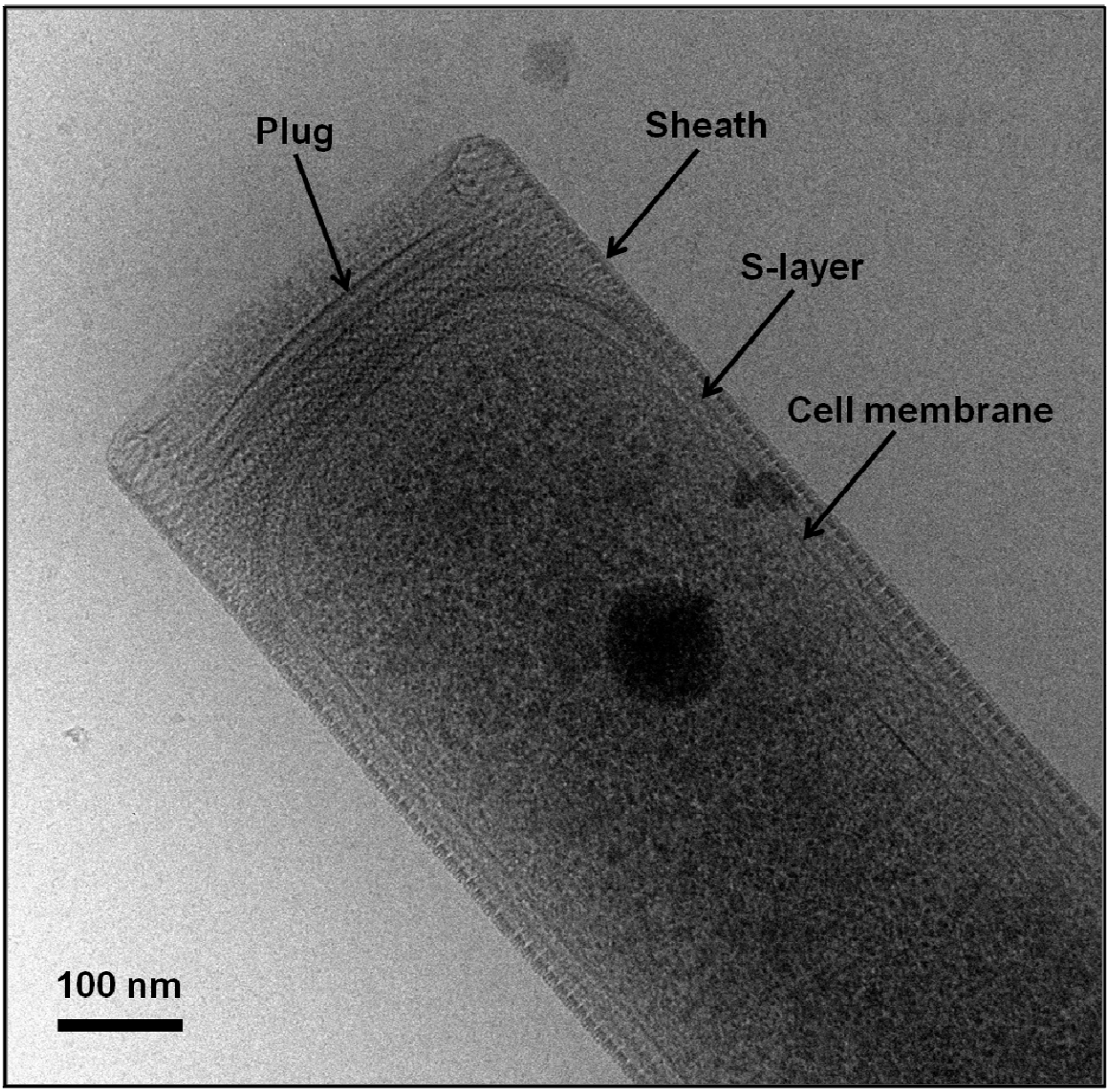

Fig. 1-10: CryoEM image of a whole *M. hungatei* cell embedded in vitreous ice showing the cell end region. The plug, sheath, s-layer, and cell membrane are indicated by arrows.

REFERENCES

Agarwal, B.K. (1991) *X-ray Spectroscopy: An Introduction(2nd ed).* Springer. Vol. 15

Albers, S.V., van de Vossenberg, J.L., Driessen, A.J., and Konings, W.N. (2000) Adaptations of the archaeal cell membrane to heat stress. *Front Biosci* **5**: D813-820.

Baker, B.J. and Banfield, J.F. (2003) Microbial communities in acid mine drainage. *FEMS Microbio Ecology* **44**(2): 139-152.

Bardy, S.L., Ng, S.Y., and Jarrell, K.F. (2003) Prokaryotic motility structures. *Microbiology* **149**: 295-304

Barns, S.M., Delwiche, C.F., Palmer, J.D., and Pace, N.R. (1996) Perspectives on archaeal diversity, thermophily and monophyly from environmental rRNA sequences. *Proc Natl Acad Sci* **93**: 9188-9193.

Bernander, R. (1998) Archaea and the cell cycle. *Mol Microbiol* **29**(4): 955-961.

Beveridge, T.J., Sprott, G.D., and Whippey, P. (1991) Ultrastructure, inferred porosity, and gram-staining character of Methanospirillum hungatei filament termini describe a unique cell permeability for this archaeobacterium. *J Bacteriol* **173**: 130-140.

Beveridge, T.J., Stewart, M., Doyle, R.J., and Sprott, G.D. (1985) Unusual stability of the *Methanospirillum hungatei* sheath. *J Bacteriol* **162**: 728-737.

Beveridge, T.J., Southam, G., Jericho, M.H., and Blackford, B.L. (1990) High-resolution topography of the S-layer sheath of the archaebacterium *Methanospirillum hungatei* provided by scanning tunneling microscopy. *J Bacteriol* **172**: 6589-6595.

Buehler, D.C., Toso, D.B., Kickhoefer, V.A., Zhou, Z.H., and Rome, L.H. (2011) Vaults engineered for hydrophobic drug delivery. *Small* **7**(10): 1432-1439.

Brochier-Armanet, C., Boussau, B., Gribaldo, S., and Forterre, P. (2008) Mecophilic Crenarchaeota: proposal for a third archaeal phylum, the Thaumarchaeota. *Nature Rev Microbiol* **6**: 245-252.

Cabello, P., Rolán, M.D., and Moreno-Vivián, C. (2004) Nitrate reduction and the nitrogen cycle in archaea. *Microbiology* **150**: 3527-3546.

Cavalier-Smith, T. (2002) The phagotrophic origin of eukaryotes and phylogenetic classification of Protozoa. *Int J Sys Evo Microbio* **52**: 297-354.

Ciaramella, M., Napoli, A., Rossi, M. (2005) Another extreme genome: how to live at pH 0. *Trends Microbiol* **13**(2): 49-51.

Coolen, M.J., Abbas, B., van Bleijsjk, J., Hopmans, E.C., Kuypers, M.M.M., Wakeham, S.G., and Damsté, J.S. (2007) Putative ammonia-oxidizing Crenarchaeota in suboxic waters of the Black Sea: a basin-wide ecological study using 16S ribosomal and functional genes and membrane lipids. *Environ Microbiol* **9**(4): 1001-1016.

Damsté, J.S., Schouten, S., Hopmans, E.C., van Duin, A.C., and Geenevasen, J.A. (2002) Crenarchaeol: the characteristic core glycerol dibiphytanyl glycerol tetraether membrane lipid of cosmopolitan pelagic cranarchaeota. *J Lipid Res* **43**(10): 1641-51.

Denli, A.M., Tops, B.B., Plasterk, R.H., Ketting, R.F., and Hannon, G.J. (2004) Processing the primary microRNAs by the Microprocessor complex. *Nature* **432**: 231-235.

Dubochet, J., Adrian, M., Chang, J.J., Homo, J.C., Lepault, J., McDowall, A.W., and Schultz, P. (1988) Cryo-electron microscopy of vitrified specimens. *Q Rev Biophys* **21**(2): 129-228.

Egorova, K. and Antranikian, G. (2005) Industrial relevance of thermophilic Archaea. *Curr Opin Microbiol* **8**(6): 649-55.

Faller, M., Toso, D., Matsunaga, M., Atanasov, I., Senturia, R., Chen, Y. Zhou, Z.H., and Guo F. (2010) DGCR8 recognizes primary transcripts of microRNAs through highly cooperative binding and formation of higher-order structures. *RNA* **16**(8): 1570-1583.

Faller, M., Guo, F. (2008) MicroRNA biogenesis: There's more than one way to skin a cat. *Biochem Biophys Acta* **1779**: 663-667.

Fancis, C.A., Beman, J.M., and Kuypers, M.M. (2007) New processes and players in the nitrogen cycle: the microbial ecology of anaerobic andarchaeal ammonia oxidation. *ISME J* **1**(1): 19-27.

Filipowicz, W., Bhattacharyya, S.N., and Sonnenberg, N. (2008) Mechanisms of post-translational regulation by microRNAs: Are the answers in sight? *Nat Rev Geneti* **9**: 102-114.

Firtel, M., Southam, G., Harauz, G., and Beveridge, T.J. (1993) Characterization of the cell wall of the sheathed methanogen *Methanospirillum hungatei* GP1 as an S layer. *J Bacteriol* **175**: 7550-7560.

Goldstein, J., Newbury, D.E., Joy, D.C., Lyman, C.E., Echlin, P., LIfshin, E., Sawyer, L., and Michael, J.R. (2003) *Scanning Electron Microscopy and X-ray Microanalysis* (3rd ed). Springer.

Hanford, M.J. and Peeples, T.L. (2002) Archaeal tetraether lipids: unique structures and applications. *Appl Biochem Biotechnol* **97**(1): 45-62

Huber, H., Hohn, M.J., Rachel, R., Fuchs, T., Wimmer, V.C., and Stetter, K.O. (2002) A new phylum of Archaea represented by a nanosized hyperthermophilic symbiont. *Nature* **417**(6884): 63-67.

Jesson, D.E., Pennycook, S.J. (1995) Incoherent imaging of crystals using thermally scattered electrons. *Proc R Soc Lond A* **449**: 273-293.

Kandler, O. and König, H. (1998) Cell wall polymers in Archaea (Archaeabacteria). *CMLS* **54**(4):305-308.

Kelman, L.M. and Kelman, Z. (2004) Multiple origins of replication in archaea. *Trends Microbiol* **12**(9): 399-401.

Koga, Y., Morii, H. (2005) Recent advances in structural research on ether lipids from archaea including comparative and physiological aspects. *Biosci Biotechnol Biochem* **69**(11): 2019-34.

Koga, Y., Morii, H. (2007) Biosynthesis of ether-type polar lipids in archaea and evolutionary considerations. *Microbiol Mol Biol Rev* **71**(1): 97-120.

Koonin, E.V., Mushegian, A.R., Galperin, M.Y., and Walker, D.R. (1997) Comparison of archaeal and bacterial genomes: computer analysis of protein sequences predicts novel functions and suggests a chimeric origin for the archaea. *Mol Microbio* **25**(4): 619-637.

Kozubal, M.A., Romine, M., Jennings, R.D., Jay, Z.J., Tringe, S.G., Rusch, D.B., Beam, J.P., McCue, L.A., and Inskeep, W.P. (2013) Geoarchaeota: a new candidate phylum in the Archaea from high-temperature acidic iron mats in Yellowstone National Park. *ISME J* **7**(3): 622-634.

Kremer, J.R., Mastronarde, D.N., and McIntosh, J.R. (1996) Computer visualization of three-dimensional image data using IMOD. *J Struct Biol* **116**: 71-76.

Leininger, S., Urich, T., Schloter, M., Schwark, L., Qi, J., Nicol, G.W., Prosser, J.I., Schuster, S.C., and Schleper, C. (2006) Archaea predominate among ammonia-oxidizing prokaryotes in soils. *Nature* **442**(7104): 806-809.

Lindås, A.-C. and Bernander, R. (2013) The cell cycle of archaea. *Nat Rev Microbiol* **11**: 627-638.

Lindås, A.-C., Karlsson, E.A., Lindgren, M.T., Ettema, T.J., and Bernander, R. (2008) A unique cell division machinery in the Archaea. *Proc Natl Acad Sci* **105**:18942-18946.

Mehta, M.P. and Baross, J.A. (2006) Nitrogen fixation at 92^{o}C by a hydrothermal vent archaeon. *Science* **314**(5806): 1783-1786.

Muller, S.A., and Engel, A. (1998) Mass measurement in the scanning transmission electron microscope: a powerful tool for studying membrane proteins. *J Struct Biol* **121**: 219-230.

Ng, S.Y., Chaban, B., and Jarrell, K.F. (2006) Archaeal flagella, bacterial flagella and type IV pili: a comparison of genes and posttranslational modifications. *J Mol Microbiol Biotechnol* **11**: 167-191.

Norris, P.R., Burton, N.P. and Foulis, N.A.M. (2000) Acidophiles in bioreactor mineral processing. *Extremophiles* **4**: 71-76.

Nunoura, T., Takaki, Y., Kakuta, J., Nishi, S., Sugahara, J., Kazama, H., Chee, G.J., Hattori, M., Kanai, A., Atomi, H., Takai, K., and Takami, H. (2011) Insights into the evolution of Archaea and eukaryotic protein modifier systems revealed by the genome of a noval archaeal group. *Nucleic Acids Res* **39**(8): 3204-3223.

Parawira, W., Read, J.S., Mattiasson, B., and Björnsson, L. (2008) Energy production from agricultural residues: high methane yields in pilot-scale two-stage anaerobic digestion. *Biomass Bioeng* **32**: 44-50.

Pikuta, E.V., Hoover, R.B., and Tang, J. (2007) Microbial extremophiles at the limits of life. *Crit Rev Microbiol* **33**: 183-209.

Robinson, C.E., Harris, J.K., Spear, J.R., and Pace, N.R. (2005) Phylogenetic diversity and ecology of environmental Archaea. *Curr Opin Microbiol* **8**: 638-642.

Samson, R.Y., Obita, T., Freunds, S.M., Williams, R.L. and Bell, S.D. A role for the ESCRT system in cell division in archaea. *Science* **322**: 1710-1713.

Schimel, J. (2004) Playing scales in the methane cycle: from microbial ecology to the globe. *Proc Natl Acad Sci* **101**(34):12400-12401.

Schiraldi, C., Giuliano, M., De Rosa, M. (2002) Perspectives on biotechnological applications of archaea. *Archaea* **1**(2): 75-86.

Shand, R.F., Leyva, K.J. (2008) Archaeal antimicrobials: an undiscovered country. In Blum P (ed.) *Archaea: New Models for Prokaryotic Biology*. Caister Academic Press.

Slaymaker, I.M., Fu, Y, Toso, D.B., Ranatunga, N., Brewster, A., Forsburg, S.L., Zhou, Z.H., and Chen, X.S. (2013) Mini-chromosome maintenance complexes form a filament to remodel DNA structure and topology. *Nucleic Acids Res.* **41**(5): 3446-56

Southam, G., and Beveridge, T.J. (1992) Detection of growth sites in and protomer pools for the sheath of *Methanospirillum hungatei* GP1 by use of constituent organosulfur and immunogold labeling. *J Bacteriol* **174**: 6460-6470.

Stephen, A.G., Raval-Fernandes, S., Huynh, T., Torres, M., Kickhoefer, V.A., and Rome, L.H. (2001) Assembly of vault-like particles in insect cells expressing only the major vault protein. *J Biol Chem* **276**: 23217-23220.

Thomas, N.A., Bardy, S.L., and Jarrell, K.F. (2001) The archaeal flagellum: a different kind of prokaryotic motility structure. *FEMS Microbiol Rev* **25**(2): 147-174.

Toso, D.B., Henstra, A.M., Gunsalus, R.P., and Zhou, Z.H. (2011) Structural, mass, and elemental analyses of storage granules in methanogenicarchaeal cells. *Env. Microbiology* **13**(9): 2587–2599

Valentine, D.L. (2007) Adaptations to energy stress dictate the ecology and evolution of the Archaea. *Nat Rev Microbiol* **5**(4): 316-323.

VanDyke, D.J., Ng, S.Y., Chaban, B., Wu, J., and Jarrell, K.F. (2008) Archaeal Flagella. *eLS*

van Zon, Z., Mossink, M.H., Scheper, R.J., Sonneveld, P., and Wiemer, E.A.C. (2003) The vault complex. *CMLS* **60**(9): 1838-1837.

Wall, J.S. and Simon, M.N. (2001) Scanning transmission electron microscopy of DNA-protein complexes. *Methods Mol Biol* **148**: 589-601.

Woese, C.R. and Fox, G.E. (1977) Phylogenetic structure of the prokaryotic domain: The primary kingdoms. *Proc Natl Acad Sci* **74**(11): 5088-5090.

Woese, C.R., Kandler, O., Wheelis, M.L. (1990) Towards a natural system of organisms: Proposal for the domains Archaea, Bacteria, and Eucarya. *Proc Natl Acad Sci* **87**: 4576-4579.

Xiao, Q., Sohn, H., Chen, Z., Toso, D., Mecklenburg, M., Zhou, Z.H., Poirier, E., Dailly, A., Wang, H., Wu, Z., Cai, M., and Lu, Y. (2012) Mesoporous metal and metal alloy particles synthesized by aerosol-assisted confined growth of nanocrystals. *Angew Chem Int Ed Engl.* **51**(42): 10546-50

Chapter II

Structural, mass, and elemental analyses of storage granules in methanogenic archaeal cells

Daniel B. Toso[1,2,3], Anne M. Henstra[1], Robert P. Gunsalus[1,4,*] and Z. Hong Zhou[1,2,3,*]

Department of Microbiology, Immunology, and Molecular Genetics[1];

Electron Imaging Center for Nanomachines, California Nano Systems Institute[2];

The UCLA Biomedical Engineering Interdepartmental Program[3];

The UCLA Institute of Genomics and Proteomics[4],

University of California, Los Angeles (UCLA),

Los Angeles, CA 90095

Running Title: Storage granules in methanogenic archaeal cells

KEYWORDS: *Methanosprillum hungatei,* polyphosphate energy storage granules, cryo-electron tomography, STEM elemental composition, cell positioning

* To whom correspondence should be addressed:

Biophysical analyses, cryo EM and tomography:

Hong Zhou: Phone 310-983-1033 Hong.Zhou@ucla.edu

Microbiology:

Rob Gunsalus: Phone 310-206-8201 robg@microbio.ucla.edu

Published in *Environmental Microbiology* September 2011; **13** (9) : 2587–2599

DOI: 10.1111/j.1462-2920.2011.02531.x

Received 20 December, 2010; accepted 18 May, 2011. Published: 12 SEP 2011. Article first published online: 19 AUG 2011

SUMMARY

Storage granules are an important component of metabolism in many organisms spanning the bacterial, eukaryal, and archaeal domains, but systematic analysis of their organization inside cells is lacking. In this study, we identify and characterize granule-like inclusion bodies in a methanogenic archaeon, *Methanospirillum hungatei*, an anaerobic microorganism that plays an important role in nutrient recycling in the ecosystem. Using cryo-electron microscopy, we show that granules in mature *M. hungatei* are amorphous in structure with a uniform size. Energy dispersive X-ray spectroscopy analysis establishes that each granule is a polyphosphate body (PPB) that consists of high concentrations of phosphorous and oxygen, and increased levels of iron and magnesium. By scanning transmission electron tomography, we further estimate that the mass density within a PPB is a little less than metal titanium at room temperature and is about 4 times higher than that of the surrounding cytoplasm. Finally, three-dimensional cryo-electron tomography reveals that PPBs are positioned off-center in their radial locations relative to the cylindrical axis of the cell, and almost uniformly placed near cell ends. This positioning ability points to a genetic program that spatially and temporally directs the accumulation of polyphosphate into a storage granule, perhaps for energy-consuming activities, such as cell maintenance, division or motility.

INTRODUCTION

Archaea encompass one of the three domains of life and have been recognized to bear more similarity to eukaryotes than to bacteria, which is one of the main reasons behind the interest in studying this unique class of organisms. Believed to be among the oldest life forms known on earth, archaeal cells use special means to generate and store energy in order to thrive in harsh environments. As one of the best studied archaea, *Methanospirillum hungatei* is a methanogen belonging to the *Methanomicrobiales* division of the *Euryarchaeota*. Initially isolated from an anaerobic benzoate degrading enrichment culture, it utilizes hydrogen plus carbon dioxide and/or formate as a source of energy and carbon for cell growth and methane production (Ferry *et al.*, 1974; Ferry and Wolfe, 1977; Mountfort and Bryant, 1982). This organism is distinct from many other hydrogenotrophic methanogens in that it can form specialized and inter-dependent biochemical partnerships with a variety of syntrophic bacteria (Ferry and Wolfe, 1976; McInerney *et al.*, 1981). When grown in co-culture, these methanogens aid in catalyzing the breakdown of a variety of short chain fatty acids, alcohols, and aromatic compounds essential for the normal operation of the anaerobic food chains in nature (Stieb and Schink, 1985; McInerney *et al.*, 2008). However, little is known concerning energy generation and storage or morphological determinants that favor the adaptation and survival of this physiologically distinct methanogen in many environmentally diverse habitats.

M. hungatei species are morphologically distinct from other methanogen cell types. With a mildly curved surface, cells exhibit the characteristic ability to grow within a sheath-like structure containing one to more than ten cells along its length (Ferry et al., 1974; Patel *et al.*, 1976; Beveridge *et al.*, 1985). All cell types retain their outer sheath during all phases of growth where multiple flagella emanate from the sheath tips or ends. The recent sequencing of *M. hungatei* JF1 genome reveals it to possess the sixth largest (3.5 MB) of all archaea genomes sequenced to date (NC_007796.1). Whereas a core set of genes/proteins were identified for

methane biosynthesis from hydrogen/carbon dioxide and/or formate, many other aspects of *Methanosprillium* cell energetics and physiology remain un-explored.

In this study, we employ a combination of biophysical methods, including cryo-electron microscopy, cryo-electron tomography, STEM tomography and EDX analyses, to identify and characterize high-density inclusion bodies (also called granules) distributed within the *M. hungatei* cell cytoplasm. We show that these structures, generally reaching 150 nm in diameter, are rich in phosphorous and oxygen and are typically positioned asymmetrically nearby each cell tip. With the likely function in phosphate and cellular energy storage, the presence of these granules may suggest an ancient origin of polyphosphate synthesis and accumulation in this model methanogenic archaean. Alternatively, they may have acquired this ability by lateral gene transfer from other organisms.

RESULTS

Observation of high-density inclusion bodies within M. hungatei cells by cryo EM

Previous ultrastructural studies of *M. hungatei* have used conventional transmission electron microscopy (TEM) of fixed cells using thin sectioning, followed by heavy metal staining (Beveridge et al., 1985; Beveridge *et al.*, 1990; Beveridge *et al.*, 1991; Southam and Beveridge, 1992; Firtel *et al.*, 1993). Such approaches suffer from dehydration of the sample, staining artifacts, as well as missing information due to the impermeability of the outer sheath layer to the stain.

CryoEM images of *M. hungatei* reveal that it has a multi-layered envelope, which includes two proteinaceous surface layers, both a paracrystalline S-layer and a sheath layer, external to the cellular bi-layer membrane, as well as a multi-layered plug structure at the ends of each cell (Fig. 2-1A-C). The use of cryo EM allows us to visualize the whole cells embedded in vitreous ice thus preserving their structures in a natural state and eliminating artifacts associated with stain. The cryo EM images of *M. hungatei* cells show an elongated shape of each cell that is 5-10 µm in length and 0.4-0.5 µm in diameter with a characteristic multi-enveloped outer structure, with the layers of sheath, S-layer, and cellular membrane clearly visible. The sheath layer at both ends of the rod-shaped cell curls inward to form a circular lip and connects with the multi-layered plug structure (Fig. 2-1A-C). However, if there is a cell division occurring between two cells sharing one sheath, then the sheath is continuous between the two cells and there is a septum region separating the ends of each cell (Fig. 2-2, inset, see also Fig. 2-6A).

The most striking feature within the cytoplasm of the cell is an electron dense inclusion body, which is similar to granules found in bacteria (Kornberg *et al.*, 1999). To our best knowledge, this is the first time the high density inclusion bodies have been described in *M. hungatei* and no systematic analysis has been carried out previously. The granules varied from

roughly spherical to an angular surfaced shape (Fig. 2-1A-C). Higher magnification images revealed that the bodies appeared to be made up of very small particles that have clustered into their characteristic spherical shape (Fig. 2-1D). No repeating or ordered arrangements were observed either visually as a crystalline pattern in the packing of the TEM image, or is obvious in the Fourier transform of the images of the inclusion bodies (Fig. 2-1D inset). Together, this evidence suggests that the bodies have an amorphous arrangement that would allow packing of smaller molecules into the structure (discussed below).

Elemental composition of inclusion bodies by EDX

In bacteria and other archaea similar granules have been characterized utilizing both energy-filtered TEM (EELS) and energy dispersive X-ray spectroscopy (EDX) in order to analyze the elemental composition of the inclusion bodies (Scherer and Bochem, 1983; Lechaire *et al.*, 2002; Remonsellez *et al.*, 2006). An FEI Titan STEM instrument was employed to collect EDX spectra to analyze the elemental composition of the inclusion bodies within representative *M. hungatei* cells (Fig. 2-3). EDX is performed in the STEM microscope by utilizing the high-energy, focused electron probe to excite a specific region of the sample. The atoms being excited may eject electrons. If an inner shell electron is ejected, its position can be occupied by a higher energy electron from the outer shell, an event accompanied by energy release in the form of an emitted X-ray photon. The energy of these X-rays is characteristic of the specific atomic element from which they were emitted. Therefore, an energy-dispersive spectrometer is used to measure the number and energy of the X-rays and give a quantitative description of the elemental composition of the specific region of the sample that was excited.

Using the EDX spectrum analysis tool integrated into FEI TIA software, we detected only the following elements in the sample: C, N, O, P, Fe, Mg, Ca, S and Si. The element line spectra across the *M. hungatei* bodies was obtained by scanning the electron probe along a line across the sample, and the spectra revealed a high abundance of phosphorous and oxygen

within the granule region (Fig. 2-3A). Area scan spectra, or dot-mapping, were also obtained by scanning specific areas of the cells that included one or more inclusion bodies, and the area scans also clearly established a high concentration of phosphorous and oxygen within the bodies (Fig. 2-3C). Among all the elements, carbon and nitrogen were found in highest abundance throughout the entire scanned region across the cells with a relative abundance of 3.5X and 1.3X respectively when compared to phosphorous, and a slight dip in carbon concentration was seen in the regions of the inclusion bodies (Fig. 2-3B), consistent with their being essential elements making up the cell envelope. After phosphorous and oxygen the next most prevalent elements, iron and magnesium, were found to be slightly concentrated (both about 0.2X phosphorous) within the granules relative to the cell cytoplasm. Lastly, calcium, silicon and sulfur were detected in small amounts within the granules at about 0.1X compared to phosphorous.

The high concentration of phosphorous and oxygen within the inclusion bodies suggests that the granules are composed of concentrated phosphate, PO_4^{-3}. Previous studies have shown that phosphate concentrates into granules by polymerizing into long chains of poly-anionic phosphate, $Cat_3PO_4(CatPO_3)_n$, where Cat is a monovalent cation and n is the length of the polymer chain (Kulaev *et al.*, 1999). The ratio of oxygen to phosphorous is approximately 5.2 (+/- 1.6):1 in the area of the granules. We reason that there are relatively more oxygen atoms than phosphorous atoms above and below the granules within the cell that also contributed to this ratio. Therefore, the actual oxygen to phosphorous ratio within the granules might be closer to 3:1, depending on the length of the phosphate chains. This high concentration of polyphosphate excludes proteins and other organic carbon, thus explaining the slight dip observed in the carbon count spectra across the area of the granules (Fig. 2-3A). The presence of low to intermediate concentrations of iron, magnesium, and calcium also suggests that the bodies are storing these elements as counter ions, and/or that the bodies are bound with enzymes or other structures with a higher concentration of these elements. It has also been

previously shown that divalent cations, such as magnesium and calcium, can form ionic bonds between two separate phosphate groups. This cross-linking activity has been proven to allow phosphate chains to pack more tightly and thus would increase the density of the granule (Parsons *et al.*, 2010). There was little apparent variation in packing or general elemental distribution within granules. This analysis allows us to conclude that the observed inclusion bodies are in fact polyphosphate bodies (PPBs).

Mass distribution of PPB by STEM tomography

While cryo EM gives faithful representation of structural organization, it does not give accurate representation of mass distribution due to the phase contrast and noisy background perturbation intrinsic to the technique. One way to get a quantization of the mass distribution is to utilize STEM imaging which allows the precise correlation of intensity to mass (Engel, 1978). In STEM imaging, an electron probe is raster scanned over a square area of the sample grid divided into n^2 elements or pixels, and at each pixel the electrons from the probe are scattered by the sample. An annular dark-field detector system capable of counting single electrons is used to collect most of the elastically scattered electrons. The resulting dark-field image can be used to directly measure the mass of the sample scanned by the electron probe, because, in unstained samples and in the absence of multiple scattering events, this annular detector signal is directly proportional to the number of atoms, weighted by atomic number (Z), irradiated by the electron probe. By utilizing theoretical data on elastic scattering it is possible to directly measure the mass, since the detector signal can be correlated directly to the number of electrons by dividing by the elastic scattering cross sections, the collection efficiency and the dose, determined by probe current, dwelling time, and pixel area (Muller and Engel, 1998). Alternatively, the mass can be estimated by comparing the signal of the sample to the signal of a mass standard, and in our case we utilized tobacco mosaic virus (TMV) particles with a known mass-per-unit-length (131.4 kDa/nm).

We collected two STEM tomography tilt series of *M. hungatei* cells mixed with TMV particles and calculated the mass density of PPB using the known TMV mass as a reference (Fig. 2-4). Having the 3D reconstructions allowed us to separate PPB and TMV from the background. From the 3D STEM tomography reconstruction, we estimated that the average mass density of the PPB is 3.8 g/cm^3, which is about 4 times higher than that of the surrounding cytoplasm. This value is larger than the density of most non-metal materials in their solid phases and is between densities of barium (3.51 g/cm^3) and titanium (4.54 g/cm^3).

3D localization of PPBs inside cells

We also systematically examined the distribution of the *M. hungatei* PPBs within the cells by taking images of entire cells frozen in vitreous ice at lower magnification to establish locations and numbers of PPBs per cell. Present in every cell and within each field examined (Fig. 2-1A-C, Fig. 2-2), we observed that there was typically one PPB located near each of the two poles of every cell.

To precisely locate the PPB inside the *M. hungatei* cells, we employed cryo-electron tomography to examine the methanogen in 3D. The 3D reconstructions of individual cells allowed us to examine the precise longitudinal and radial positions of each PPB within the cell lumen (Fig. 2-5). Among the 65 cells analyzed, we found that the average longitudinal distance of the PPB is 612 +/- 52 nm from the cell end, measured from the plug (Fig. 2-6C). Perpendicular cross-sectional views of the reconstructions through the center of the PPB (Fig. 2-5F) also reveal the precise distance from the center of the PPB to the radial center of each cell. The PPBs are centered, on average, 74 +/- 4 nm from the cylindrical axis of the cell (Fig. 2-6D). Interestingly, the off-center distance is about the same as the radius of the PPB (described below) (*i.e.*, 145/2=72.5 nm).

From the 3D tomograms, we then measured the dimensions of the PPBs (Fig. 2-6E). The 65 bodies measured are 145 +/- 3 nm in diameter, which reflects a fairly consistent size in

fully mature cells (*e.g.*, in stationary phase cells), but in actively growing and dividing cells the bodies are found in a range of diameters up to 200 nm. The approximate diameter of 150 nm would give a PPB volume of 1.8×10^6 nm^3/body [*i.e.*, $V = (4/3)*\pi*75^3$]. For each PPB, this would be equivalent to approximately 0.2% of the total cell volume assuming cylindrical cell dimensions of 450 nm diameter by 5 μm length (cell volume V = 0.80 μm^3). Calculating based on the volume of the body (1.8×10^6 nm^3), the density of the body (3.8 g/cm^3), and the molecular weight of each PO_3 group of polyphosphate (79 g/mol), we estimate that the maximum amount of phosphate that could be present in one body is about 8.7×10^{-5} pmol. If divalent cations were to comprise 25% of the PPB, the value would be reduced to 6.5×10^{-5} pmol.

Distribution of PPBs in different stages of cell growth

In stationary phase cells, in which the cells have a more regular length and are not growing or dividing, the bodies are always found near the ends of each cell and never intermediate along the length. Also, the bodies in stationary phase cells are usually fully developed, with a mostly uniform size and shape in contrast to the smaller granules observed in newly dividing cells. Cell growth and division during exponential phase requires significant phosphate utilization for biosynthesis, which may limit phosphate accumulation and incorporation into the PPBs, and thus contribute to PPB size variability. In early stationary phase cells, the phosphate demand is reduced, allowing equilibration of the phosphate body development.

In exponential growth phase, as the cells lengthen prior to cell division, one or two additional PPBs are often observed in the middle of the cell, and at roughly equal distance from the opposite end (Fig. 2-2). These PPBs appear to be in the process of newly forming, with the smaller body at the mid-cell location in contrast to a larger body at the other end of the cell that has previously undergone cell division. This suggests that, during cell growth, two new PPBs are initiated and develop in the middle of the cell in preparation for cell division. When multiple

M. hungatei cells share a common sheath with septum regions between adjacent cells (Fig. 2-2, arrows), the PPBs are present at both ends of adjacent cells (*i.e.*, on both sides of the septum spacer regions). It is not known what guides PPB development during cell division but our observations of multiple cells suggest that, after sufficient cell elongation occurs, and before the new cell end forms, a new body initiates close by the pole adjacent to the newly forming septum. Granule migration from other cell locations was not evident. The newly formed PPB then gradually enlarges into a fully developed body as the cells further extend within the sheath and then divide. A similar and irregularly shaped small body also appears on the opposite side of the newly forming septum (Fig. 2-2, right inset indicated with arrows). These small growing bodies which would presumably be the new, daughter bodies found at the new cell ends appear to mature at similar rates. In some instances, one body is considerably larger (Fig. 2-6A) and it is unknown if this represents an existing body from an old cell, or if a development plan and or cell metabolism allows more rapid PPB synthesis.

DISCUSSION

One of the first observations about the PPBs discovered in the frozen hydrated *M. hungatei* cells was their localization at the ends of each cell (Fig. 2-1). After further study, the PPB number, location, and size revealed a relationship between the number of bodies and the length of the cells: as the cells grow, additional bodies develop along their length (Fig. 2-2). This may indicate a function for the bodies throughout the length of the cell, or they may be developing in preparation for a new division event after additional growth has occurred. The presence of PPBs in close proximity to the ends of nearly every cell indicates there may be some function required at the cell end. It is perhaps used as a phosphate-based energy source, for example, in flagellar/motor biogenesis or function, as the archaeal flagella protrude from the nearby cell ends and many can be seen in images of cells in motile phase (Fig. 2-6B). However, the fact that PPBs are also positioned at the ends of cells in the middle of chains of multiple cells within a single sheath would suggest other roles that are not tightly coupled to flagellar function, since the internal cells do not produce flagella.

PPBs in stationary, older cells are larger and more uniformly shaped than in pre-division or recently divided cells (*e.g.*, Fig. 2-2). This indicates that as additional phosphate is taken up by the cell, PPBs grow as excess phosphate is incorporated. In a phosphate limited environment, it would be presumed that PPBs would fail to develop although this has not been tested experimentally. In addition, despite their amorphous composition, PPBs tend to round up into spherically shaped particles. This is most likely due to the need to minimize the surface energy of the PPB by achieving the maximum compaction and lowest surface area to volume ratio. It is known that short polyphosphate chains [*e.g.*, two (pyrophosphate) or three (tripolyphosphate) phosphates] form crystalline structures naturally (Griffith and Grayson, 1977; Pritzker, 1998). The amorphous packing of PPBs inside *M. hungatei* observed in this study suggests that they contain longer phosphate chains. In other organisms these are reported to range from several hundred to over one thousand repeating units in length.

Is PPB development in M. hungatei programmed?

As noted above, PPBs in mature *M. hungatei* cells achieve a uniform size of about 150 nm in diameter and are positioned near cell ends (Fig. 2-1) but off-center from the longitudinal cell axis. These PPBs are located about one radius in distance from the center of the cell (Fig. 2-6D), and this would mean that the edge of each PPB is usually located in close proximity to the center line of the cell (Fig. 2-5F). Therefore, if there are cytoskeletal structures that run along the length of the cells down their centers, the PPBs would be positioned to interact with such structures. It has yet to be observed, in *M. hungatei*, if there are any such intracellular structures contacting the PPB. In contrast to well studied bacterial systems (Rao *et al.*, 2009), we still know little about events of cell positioning and replication in the archaea. The ability to uniformly position PPBs within each cell in concert with the observed pattern for development of new bodies indicates that *M. hungatei* possesses a genetic program to spatially and temporally direct these events. This process would appear to be coupled to cell growth and division within the sheath since random cell locations were not observed. Whether polyphosphate is somehow directly involved in and essential for these events, or alternatively, is a by-product of them, is unknown.

Polyphosphate in other organisms

Related PPBs in bacteria and archaea have been reported to sequester heavy metals and other elements. In the archaeon, *Sulfolobus metallicus,* it was observed that PPBs decreased in number and size upon exposure to increasing copper concentration (Remonsellez et al., 2006). They concluded that the phosphate was utilized in metal ion detoxification by binding up the copper ions prior to being transported out of the cells. EDX and electron energy loss spectroscopy were used to verify the sequestration of these elements within the bodies of cells grown in an environment containing heavy metals. Considerably lower levels of polyphosphate

were detected in *Sulfolobus acidocaldarius* and *Sulfolobus solataricus* cells and this was not altered by copper ion exposure (Remonsellez et al., 2006).

Few other archaeal species are reported to contain PPBs. *Methanosarcina vacuolata* as well as *Methanosarcina barkeri* strains Fusaro, 227, and Wiesmoor each contained a single round to oval shaped PPB-like granule of 0.15-0.30 μm in diameter with associated Ca and Fe ions (Scherer and Bochem, 1983). Presence of the bodies was variable depending on the nutritional conditions used, and they gradually disappeared as cells aged or starved. In contrast, addition of FeS appeared to stimulate body density which the authors suggested may be due to accumulation of polymeric iron phosphate. Interestingly, several of the above mentioned strains also contained up to a hundred very small irregular shaped inclusion bodies called “granula” that were likely to be composed of polyphosphate based on their EDX spectra (Scherer and Bochem, 1983). The relationship of cyclic 2,3-diphosphoglycerate synthesis and “granula” accumulation to 14% of the *Methanosarcina mazei* (formerly *Methanosarcina frisia)* cell dry weight is unknown, although the cellular phosphate accumulation was dependent on phosphate availability and the methanogenic substrate used (Rudnick *et al.*, 1990). No related “granula” bodies were observed in *M. hungatei* cells (this study).

Polyphosphate has been shown to be an important compound in the metabolic and regulatory pathways of many organisms (Kulaev and Kulakovskaya, 2000; Rao et al., 2009). It has very diverse roles in bacterial and eukaryotic cells, including phosphate reserves, cation sequestration and storage, cell envelope formation and function, modulating gene expression, regulation of enzyme activity, stress response and stationary phase adaptation, membrane channel function, *etc*. In *E. coli* the enzyme PPK (polyphosphate kinase) has been shown to be an important regulator of PPB biosynthesis (Ahn and Kornberg, 1990). The analogs for PPK in archaea species that exhibit polyphosphate body formation have not been reported, but a similar enzymatically regulated process is thought to occur. Inspection of the *M. hungatei*

genome reveals two ppk-like genes, Mhun_0889 and Mhun_1431 that are candidates for this function (Ca. ~8.6 e-108 relative to *E. coli* b2501).

Polyphosphates were found to play a key role in regulatory control, in *E. coli*, during the transition from growth phase to stationary phase and to the survival of the cell in the stationary phase or under stress (Kornberg et al., 1999). Many archaea, including *M. hungatei*, exist in harsh environments that would be uninhabitable for many other organisms, therefore mechanisms to cope with environmental stress including phosphate limitation are expected. In this regard, the genome reveals both a high affinity ABC-type phosphate uptake system as well as a Na+ type low affinity phosphate symport system. The PPBs could certainly function to help *M. hungatei* handle other environmental stresses, such as metal toxicity as shown in *Sulfolobus* species (Remonsellez et al., 2006), or perhaps in aiding accumulation of iron as seen in *Methanosarcina barkeri* (Scherer and Bochem, 1983).

It was recently shown by cryo-electron microscopy and tomography of carboxysomes in several bacterial cell types (*i.e.*, in *Halothiobacillus neapolitanus, Thiomonas intermedia*, and *Thiomicrospira crunogena*) (Iancu *et al.*, 2010) that PPB-like granules were often associated with these shell structures. Although little is known about the properties or associated functions of these putative PPB-like granules, it was suggested that they may somehow provide cations needed for carboxysome synthesis and/or functioning. By analogy, *M. hungatei* might employ PPBs to sequester divalent cations (*e.g.*, Fe) needed in great abundance for methane biosynthesis.

Other roles for PPBs are possible. For example, when methanogenic substrates (i.e., hydrogen or formate) are depleted in the cell's immediate environment, cellular energy in the form of ion gradients and ATP becomes limited. Under these conditions, polyphosphate-based energy reserves in *M. hungatei* could then be employed to fuel essential cell functions, by re-synthesizing ATP using the anhydride bond energy stored in PPBs, and/or to restore

electrochemical ion gradients. The latter would fuel motility and taxis to allow cells to find new substrate(s) and adapt accordingly. Based on the PPB volume and density values reported above, we have estimated that each granule contains about 6.5 x 10^{-5} pmol of phospho-anhydride repeating units. Were this stored bond energy in both PPB granules to be freely converted into ATP, it would be equivalent to 13 x 10^{-5} pmol of ATP or about 200 mM ATP given the cell volume V = 0.80 μm^3. Thus, the *M. hungatei* PPB appears to be a remarkably compact energy storage device! The two PPBs per cell require only ~0.4% of the cell volume and stores ~100 fold more energy than is contained in the cellular ATP pool within the other 99.6% of the cytoplasm (i.e., assuming an intracellular ATP concentration of 2 mM). These estimates of PPB density and energy storage in *M. hungatei* have significant implications for PPB in other archaea and bacteria. Regardless of PPB function(s), *M. hungatei* appears to be exquisitely adapted for life in low hydrogen environments.

EXPERIMENTAL PROCEDURES

Cell culture

Methanosprillum hungatei strain JF1 (DSM 864) was cultivated on a CO_2/bicarbonate buffered mineral medium supplemented with trace metals, vitamins, and sodium acetate with a vessel headspace containing a 80%-20% atmosphere of hydrogen and carbon dioxide. The medium contained per 1000 ml: 0.54 g NaCl, 0.12 g $MgSO_4 \cdot 7H_2O$, 5.0 g NH_4Cl, 1.8 g KH_2PO_4, 2.9 g K_2HPO_4, 0.06 g $CaCl_2 \cdot 2H_2O$, 2.72 g Na Acetate $\cdot 3H_2O$, 10 mL of 100x trace metal solution and 1 mL of 1000x vitamin solution. Following sterilization, the medium was supplemented with 10 ml filter-sterilized solution of reducing reagent (2.5% $Na_2S \cdot 9H_2O$, 2.5% Cysteine HCl) and 20 ml of a 1 M $NaHCO_3$ solution. Trace metals and vitamins were as previously described for *M. acetivorans* (Rohlin and Gunsalus, 2010). Following inoculation, anaerobe tubes containing 10 ml of medium were incubated at 37 °C horizontally on a rotary drum shaker (60 RPM, New Brunswick, Inc). Cells were serially transferred at least three times with transfers made at mid-exponential phase to achieve 10 plus cell doublings prior to harvest and electron microcopy analysis.

Cryo-electron microscopy

To optimize samples for cryo EM observation, we first performed negative stained electron microscopy of cells prepared on carbon-coated copper grids and stained with 1% uranyl acetate. To adjust the sample concentration, cells were centrifuged at low speed in a table-top microfuge, and re-suspended at the appropriate density using culture medium.

A droplet of 4 µl of the sample with optimized concentration was placed onto a glow discharged, 200 mesh Quantifoil grid (Ermantraut *et al.*, 1998) with a spacing of 3.5 µm hole/ 1 µm edge. The sample was allowed to settle for 30 seconds, blotted by filter paper, and immediately plunged into liquid nitrogen cooled liquid ethane.

An FEI Tecnai F20 transmission cryo-electron microscope with an accelerating voltage of 200 kV was used to image the *M. hungatei* cells imbedded in vitreous ice. Each image was imaged at a dosage of 33 and 6 electrons/$Å^2$, for those shown in Fig. 2-1 and 2-2, respectively. The targeted underfocus values were 2.5 µm.

Cryo-electron tomography

For cryo ET, we have used two cryo-electron microscopes. For PPB location and size distribution, we used the above mentioned Tecnai F20 instrument with a 16 megapixel CCD camera. For the cryo ET reconstructions shown in Fig. 2-5, we used an FEI Titan Krios instrument with a Gatan image filter (GIF) and a 4 mega pixel CCD camera, with the instrument operated at an accelerating voltage of 300kV and a total dose of 100 $e^-/Å^2$ for each tilt series. During tilt series acquisition, we chose cells whose long axis was roughly parallel to the tilt axis of the microscope. The cells were imaged at 29,000x. An underfocus value of 3 to 6 µm at zero degrees tilt was used. All tomography tilt series were recorded using the FEI Batch Tomography software with a tilt range from -70^o to $+70^o$.

STEM tomography and EDX analysis

We performed the STEM imaging/tomography and EDX analysis using an FEI Titan 80-300kV scanning transmission electron microscope. *M. hungatei* cells were placed on carbon coated copper grids, air-dried and imaged inside the Titan instrument.

For mass measurement using STEM tomography, we mixed tobacco mosaic virus (TMV) particles with the *M. hungatei* cells before placing the sample on grids. Samples were loaded on a Fischione 2020 tomography holder and FEI batch tomography software was used to collect STEM tomography tilt series at 300kV accelerating voltage.

FEI TEM Imaging and Analysis (TIA) software package was used to acquire the line scan and area scan EDX spectra of different areas of the sample at 80kV at a dosage of about 50 $e^-/Å^2$. The spectral data for the indicated elements were stored as counts over distance or

area. The area spectra were output in 3D graphical format using Mathematica (Wolfram Research).

CryoET data analysis and 3D visualization

The tomography tilt series were processed with a suite of programs to generate a 3D reconstruction. Inspect3D was used to quickly achieve an initial rough alignment (translation, rotation, and tilt axis) of the tilt series using the graphical interface of the software. The image stacks were roughly aligned using cross-correlation with proper filtering. The high and low-pass limits for the filtering were optimized so that a clearly distinguishable cross-correlation peak was obtained. After this alignment, the tilt axis was adjusted so that it was vertical and centered. This process was repeated 3-4 times until there were no further changes larger than one pixel in the x and y translational coordinates.

After the initial rough alignment, gold-bead tracking in Inspect3D was used to align the tilt series more precisely. Gold bead tracking started with finding several representative beads at zero degrees tilt to create a representative model, this model was used to find many other beads, bad beads were discarded, and the remainder were tracked throughout the whole tilt series. Errors in bead tracking were corrected and an alignment solution was calculated based on the bead positions. At this point the bead positions could be iteratively error adjusted and a new alignment solution could be found until it converged on a solution with the least amount of error. Once the precise alignment was found it was applied to the tilt series.

The aligned tilt series was then used to make a 3D reconstruction using GPU-based SIRT (Simultaneous Iterative Reconstruction Technique) reconstruction implemented in Inspect3D. The 3D reconstructions were saved as a stack of X-Y plane images that are single pixel slices along the Z-plane.

Alternatively, we used the *etomo* tomography processing software from the Imod package (Kremer *et al.*, 1996) to perform very similar alignment and reconstruction steps as

those described above, including rough alignment by cross-correlation, fine alignment by fiducial (gold-bead) tracking, and reconstruction by weighted back-projection. We further processed the reconstructions by applying a median filter to enhance the contrast.

Slices from the reconstructions were displayed using slicer within *3dmod* from the Imod package. Amira (Visage Imaging GmbH, http://www.amira.com/) was used to create volume renderings of the 3D density maps of the cells.

Acknowledgements

We thank Feng Shen for technical assistance in STEM tomography, Matthew Mecklenburg for assistance in EDX data collection and presentation, and Bridget Carragher and Ruben Diaz-Avalos for the TMV sample used as a mass standard. This research was supported in part by the Department of Energy Biosciences Division grant award DE-FG03-86ER13498 and the UCLA-DOE Institute of Genomics and Proteomics to RPG, the Netherlands Organisation for Scientific Research (NWO) to AMH, and the National Institutes of Health (NIH; GM071940 and AI069015 to ZHZ). We acknowledge the use of electron microscopy facilities at the UCLA Electron Imaging Center for NanoMachines in California NanoSystems Institute (CNSI) supported by NIH (1S10RR23057 to ZHZ).

FIGURES

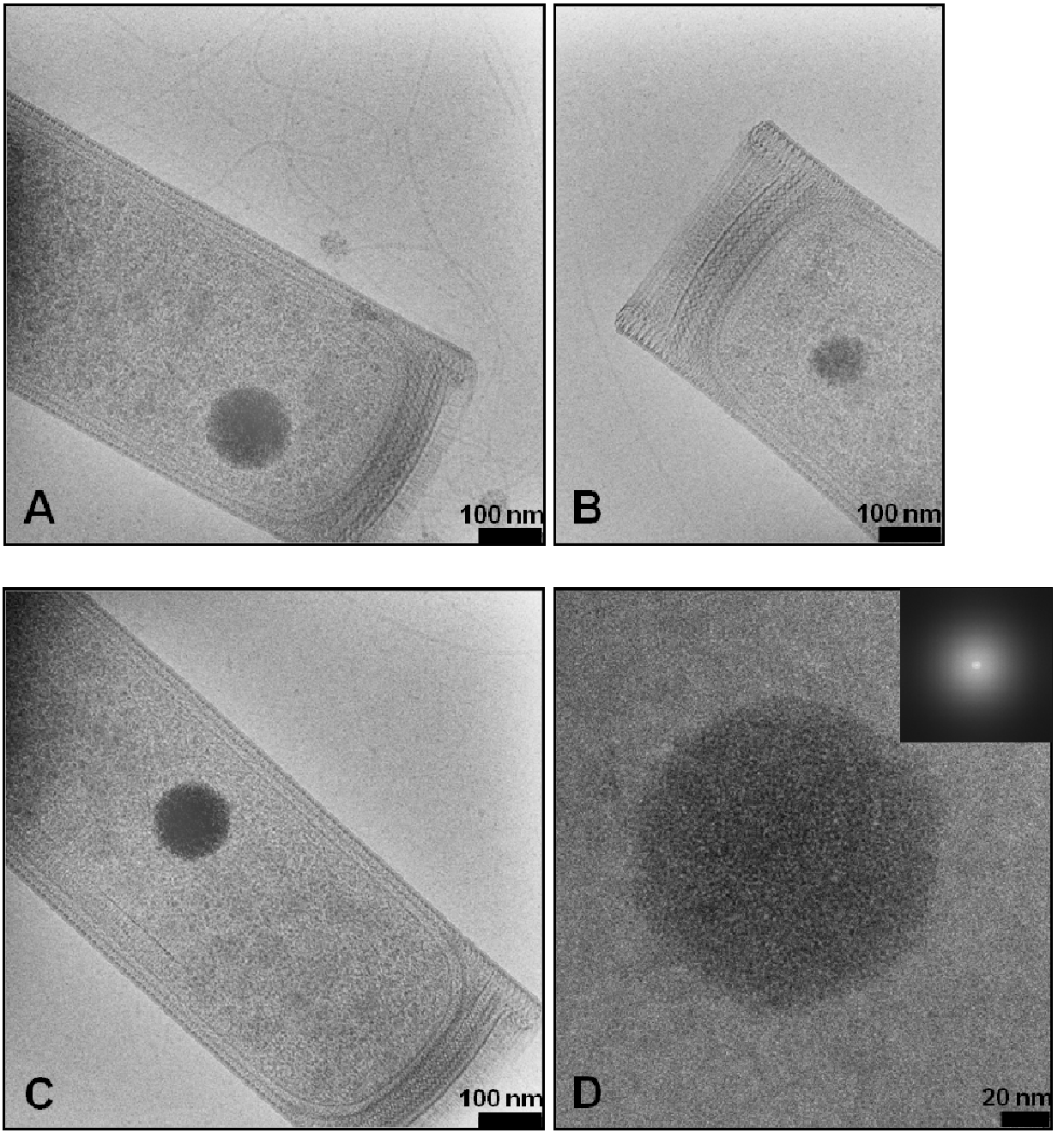

Fig. 2-1. CryoEM of *M. hungatei* JF1 cells. (A-C) Representative cryo EM images of cell ends showing characteristic high-density inclusion bodies. (D) Higher magnification cryo EM image of the same inclusion body shown in (C). The inset is the Fourier transform of the image, showing no pattern indicative of a crystalline lattice or ordered structure within the inclusion bodies.

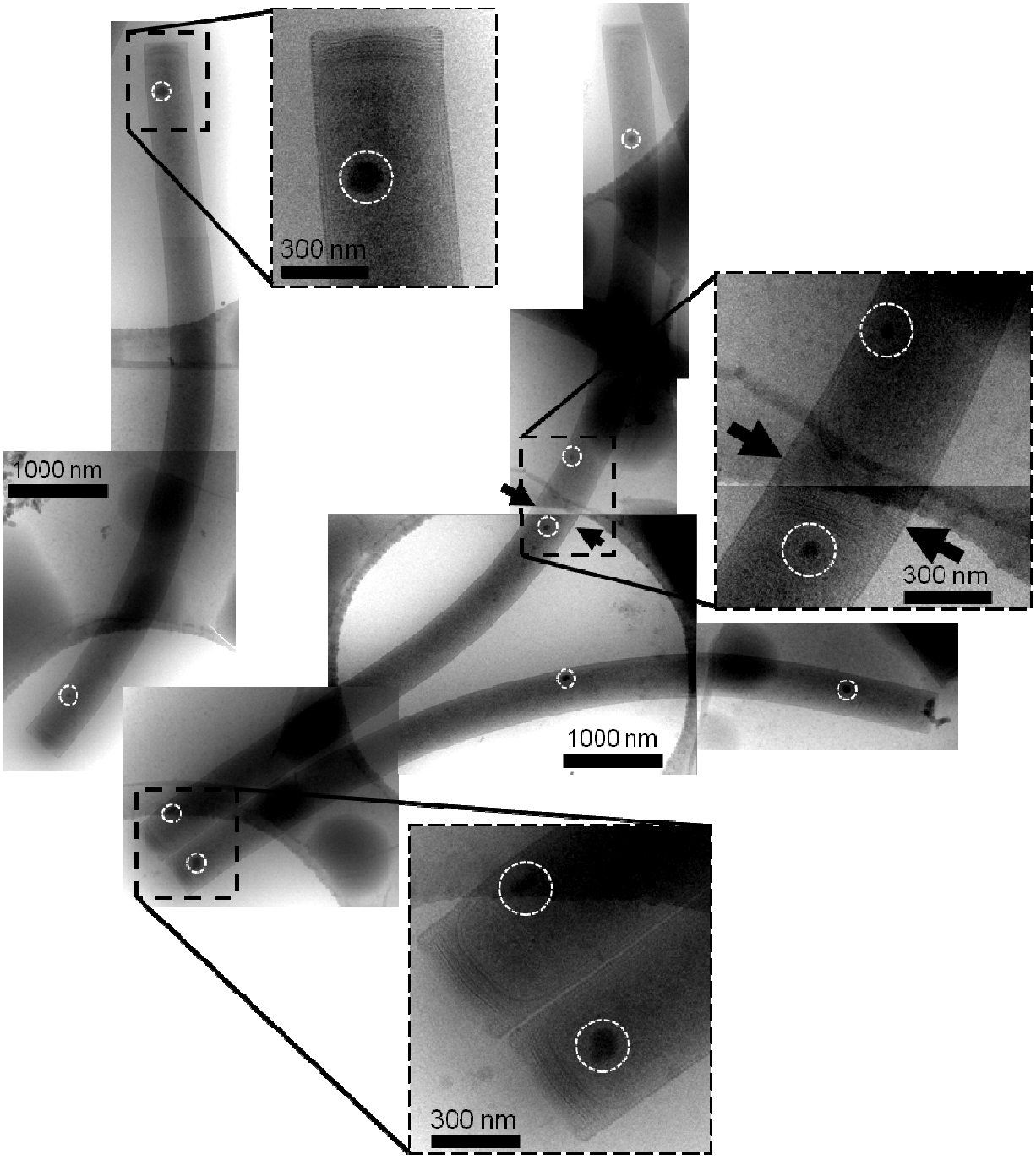

Fig. 2-2. Composite cryo EM images showing whole *M. hungatei* JF1 cells and the relative longitudinal locations of the inclusion bodies. The location of a cell division/septum is indicated by the arrows and inclusion bodies are marked by circles.

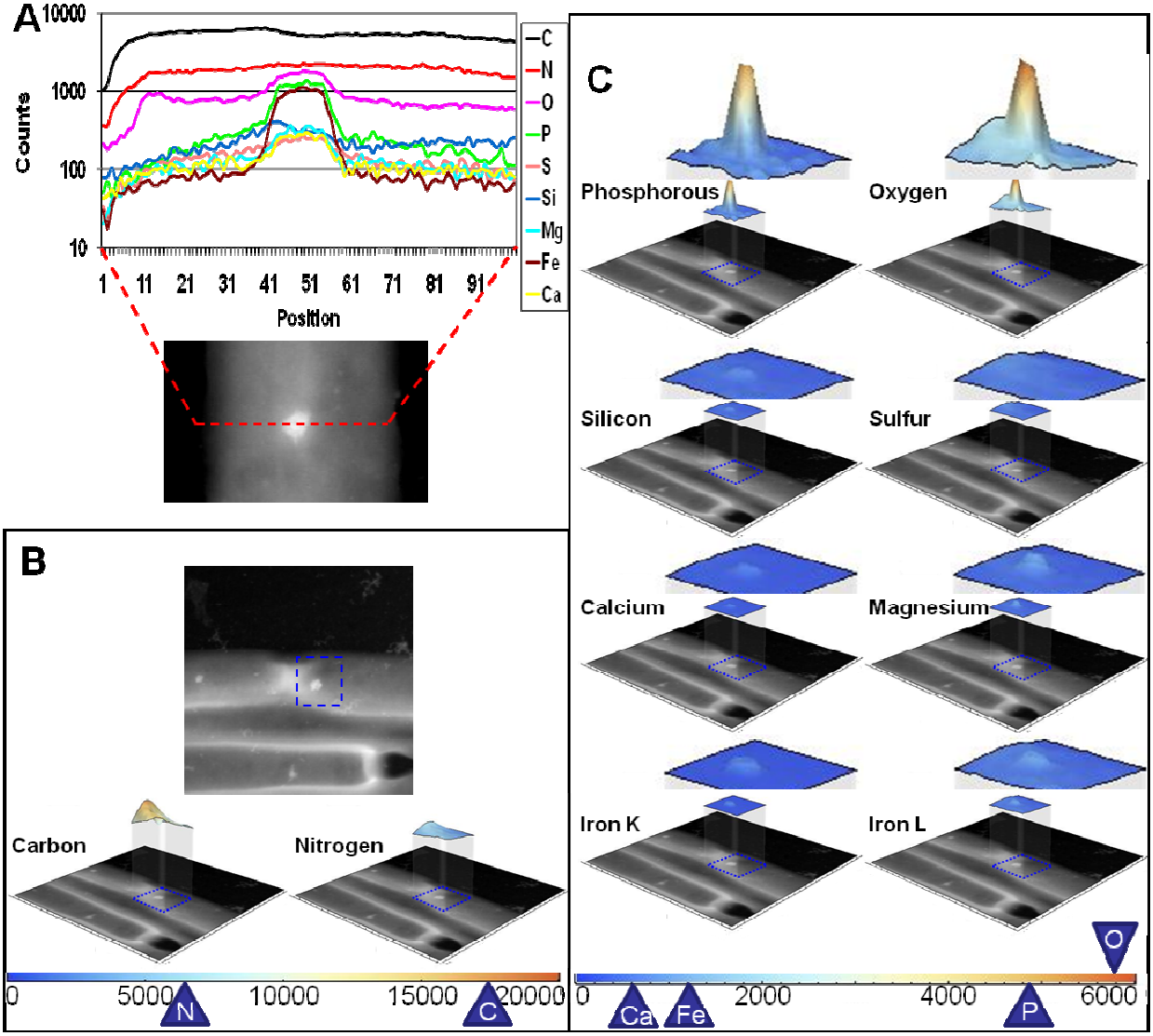

Fig. 2-3. EDX analyses of the *M. hungatei* inclusion bodies. (A) A line spectrum across the width of a cell in the region with an inclusion body. The spectra of the most prevalent elements present in the cell are plotted using different colors (indicated in the box to the right). (B-C) Area spectra of the most prevalent elements identified through the EDX analyses. Top panel in (B): A STEM image of a region containing the ends of three cells. The blue box indicates the region analyzed by EDX to produce an area spectrum (not shown). This area spectrum is then decomposed into individual ones corresponding to different elements. Those spectra with significant counts are displayed as three-dimensional color maps with the color-

coding indicated below. Also shown below each color spectrum is the STEM image to illustrate the location of the area scanned. Due to the use of carbon support film and the natural abundance of both carbon and nitrogen, the spectra for carbon and nitrogen have the highest counts and are shown in the bottom of (B) with a different scale. The spectra for the other prevalent element are shown in (C). Peak counts are also indicated on the color scale bars at the bottom.

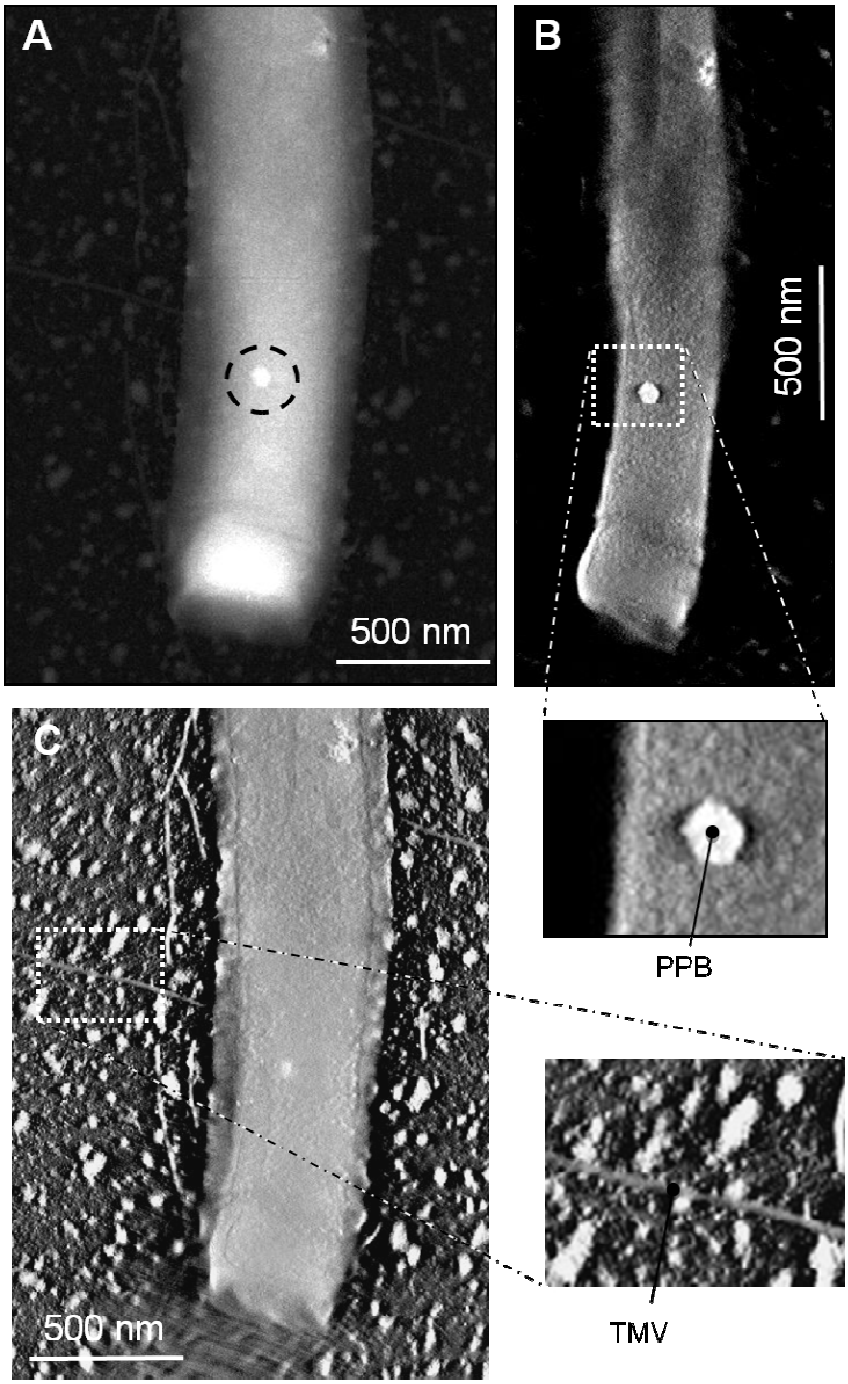

Fig. 2-4. Mass measurement of PPB inside *M. hungatei* cells by STEM tomography.

Tobacco mosaic virus (TMV) is included to serve as a standard for mass measurements. (A) STEM image of the end of a cell containing a PPB (circled). (B-C) Slices extracted from the 3D STEM tomogram reconstructed from the tilt series of the cell shown in (A). Slice in (B) shows the PPB and that in (C) shows the TMV particles.

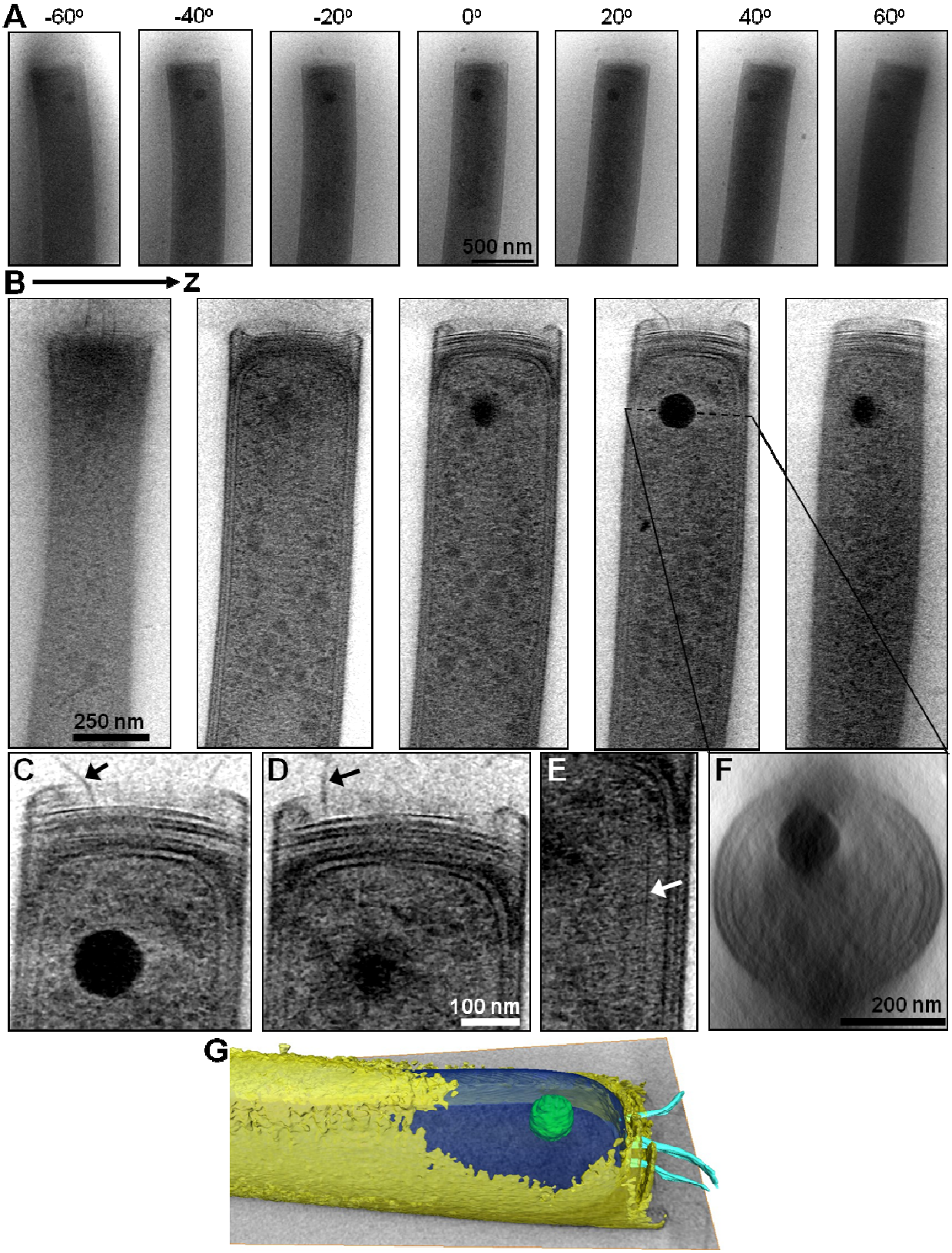
A
-60°
-40°
-20°
0°
20°
40°
60°
500 nm
B
z
250 nm
C
D
100 nm
E
F
200 nm
G

Fig. 2-5. Three-dimensional localization of PPB inside *M. hungatei* cells by cryo ET. (A) An example cryo ET tilt series (+/- 70° tilts) of the end of an *M. hungatei* cell. Only seven of 71 images in the tilt series are shown for illustration and their tilt angles are indicated. (B) Density slices extracted from the 3D tomogram reconstructed from the tilt series shown in (A). (C)-(E) Higher magnification slices from the reconstruction show flagella and cytoskeletal structures, indicated by arrows. (F) A perpendicular cross-section through the 3D reconstruction showing the location of the PPB within the cell lumen. (G) Volume rendering of the tomogram with the PPB shown in green, the cytoplasm in blue, envelope in yellow and flagella in cyan. The cytoplasm and envelope are displayed semi-transparently so that the PPB volume is visible. Shown in grayscale is a slice from the 3D tomographic reconstruction.

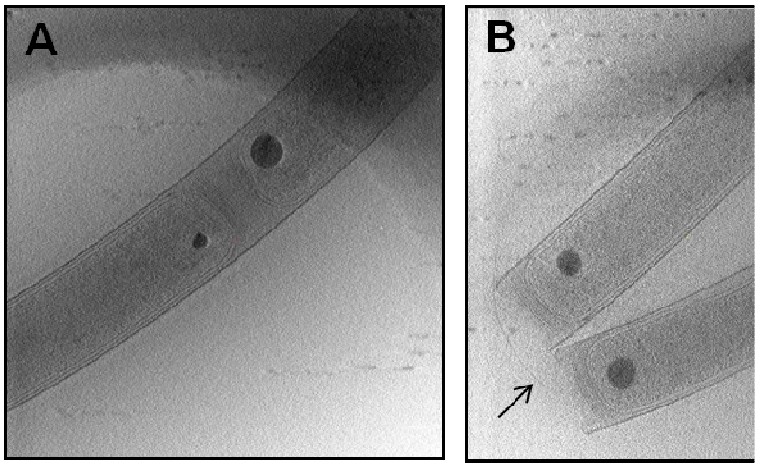
A
B

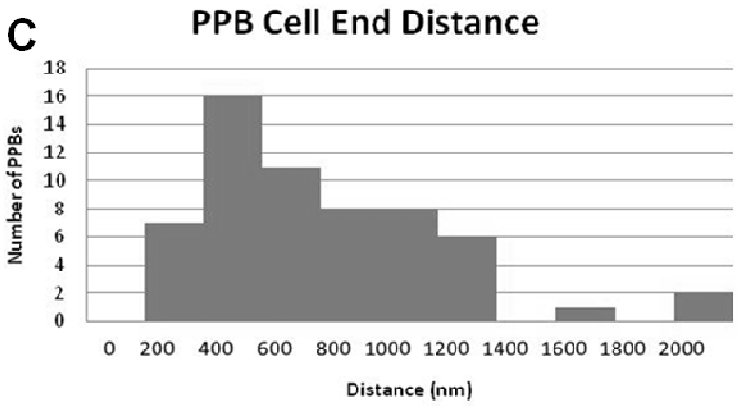
C
PPB Cell End Distance
Number of PPBs
0
2
4
6
8
10
12
14
16
18
0 200 400 600 800 1000 1200 1400 1600 1800 2000
Distance (nm)

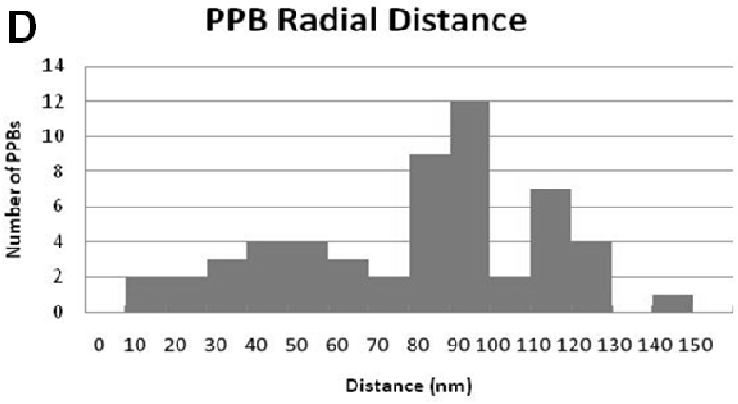
D
PPB Radial Distance
Number of PPBs
0
2
4
6
8
10
12
14
0 10 20 30 40 50 60 70 80 90 100 110 120 130 140 150
Distance (nm)

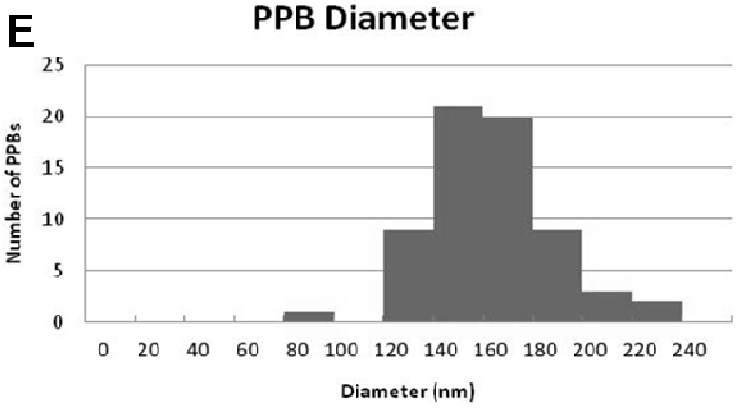
E
PPB Diameter
Number of PPBs
0
5
10
15
20
25
0 20 40 60 80 100 120 140 160 180 200 220 240
Diameter (nm)

Fig. 2-6. Location and size distributions of PPB inside *M. hungatei* cells. (A-B) Central slices through 3D tomographic reconstructions of different *M. hungatei* cells. The slice shown in (A) contains the septum between two recently divided cells sharing a sheath. Note the size difference of the PPBs on the opposite sides of the septum. The slice shown in (B) contains many flagella (arrow) protruding from the ends of the cells. (C) Distribution of PPB distance from ends of cells. (D) Distribution of the PPB relative to the cylindrical axis of the cell. (E) Distribution of PPB diameters. These measurements are based on 65 PPBs in 3D cryo ET reconstructions.

REFERENCES

Ahn, K., and Kornberg, A. (1990) Polyphosphate kinase from *Escherichia coli*. Purification and demonstration of a phosphoenzyme intermediate. *J Biol Chem* **265**: 11734-11739.

Beveridge, T.J., Sprott, G.D., and Whippey, P. (1991) Ultrastructure, inferred porosity, and gram-staining character of Methanospirillum hungatei filament termini describe a unique cell permeability for this archaeobacterium. *J Bacteriol* **173**: 130-140.

Beveridge, T.J., Stewart, M., Doyle, R.J., and Sprott, G.D. (1985) Unusual stability of the *Methanospirillum hungatei* sheath. *J Bacteriol* **162**: 728-737.

Beveridge, T.J., Southam, G., Jericho, M.H., and Blackford, B.L. (1990) High-resolution topography of the S-layer sheath of the archaebacterium *Methanospirillum hungatei* provided by scanning tunneling microscopy. *J Bacteriol* **172**: 6589-6595.

Engel, A. (1978) Molecular weight determination by scanning transmission electron microscopy. *Ultramicroscopy* **3**: 273-281.

Ermantraut, E., Wohlfart, K., and Tichelaar, W. (1998) Perforated support foils with pre-defined hole size shape and arrangement. *Ultramicroscopy* **74**: 75-81.

Ferry, J.G., and Wolfe, R.S. (1976) Anaerobic degradation of benzoate to methane by a microbial consortium. *Arch Microbiol* **107**: 33-40.

Ferry, J.G., and Wolfe, R.S. (1977) Nutritional and biochemical characterization of *Methanospirillum hungatii*. *Appl Environ Microbiol* **34**: 371-376.

Ferry, J.G., Smith, P.H., and Wolfe, R.S. (1974) *Methanospirrillum*, a new genus of methanogenic bacteria. *International Journal of Systematic Bacteriology* **24**: 465-469.

Firtel, M., Southam, G., Harauz, G., and Beveridge, T.J. (1993) Characterization of the cell wall of the sheathed methanogen *Methanospirillum hungatei* GP1 as an S layer. *J Bacteriol* **175**: 7550-7560.

Griffith, E.J., and Grayson, M. (1977) *Topics in Phosphorous Chemistry*. Ann Arbor, MI: J. Wiley and sons Interscience.

Iancu, C.V., Morris, D.M., Dou, Z., Heinhorst, S., Cannon, G.C., and Jensen, G.J. (2010) Organization, structure, and assembly of alpha-carboxysomes determined by electron cryotomography of intact cells. *J Mol Biol* **396**: 105-117.

Kornberg, A., Rao, N.N., and Ault-Riche, D. (1999) Inorganic polyphosphate: a molecule of many functions. *Annu Rev Biochem* **68**: 89-125.

Kremer, J.R., Mastronarde, D.N., and McIntosh, J.R. (1996) Computer visualization of three-dimensional image data using IMOD. *J Struct Biol* **116**: 71-76.

Kulaev, I., and Kulakovskaya, T. (2000) Polyphosphate and phosphate pump. *Annu Rev Microbiol* **54**: 709-734.

Kulaev, I., Vagabov, V., and Kulakovskaya, T. (1999) New aspects of inorganic polyphosphate metabolism and function. *J Biosci Bioeng* **88**: 111-129.

Lechaire, J.P., Shillito, B., Frebourg, G., and Gaill, F. (2002) Elemental characterization of microorganism granules by EFTEM in the tube wall of a deep-sea vent invertebrate. *Biol Cell* **94**: 243-249.

McInerney, M.J., Bryant, M.P., Hespell, R.B., and Costerton, J.W. (1981) *Syntrophomonas wolfei* gen. nov. sp. nov., an anaerobic, syntrophic, fatty acid-oxidizing bacterium. *Appl Environ Microbiol* **41**: 1029-1039.

McInerney, M.J., Struchtemeyer, C.G., Sieber, J., Mouttaki, H., Stams, A.J., Schink, B. et al., (2008) Physiology, ecology, phylogeny, and genomics of microorganisms capable of syntrophic metabolism. *Ann N Y Acad Sci* **1125**: 58-72.

Mountfort, D.O., and Bryant, M.P. (1982) Isolation and characterization of an anaerobic syntrophic benzoate-degrading bacterium from sewage sludge. *Arch Microbiol* **133**: 249-256.

Muller, S.A., and Engel, A. (1998) Mass measurement in the scanning transmission electron microscope: a powerful tool for studying membrane proteins. *J Struct Biol* **121**: 219-230.

Parsons, A.J., Ahmed, I., Rudd, C.D., Cuello, G.J., Pellegrini, E., Richard, D., and Johnson, M.R. (2010) Neutron scattering and *ab initio* molecular dynamics study of cross-linking in biomedical phosphate glasses. *J Phys Condens Matter* **22**: 485403.

Patel, G.B., Roth, L.A., van den Berg, L., and Clark, D.S. (1976) Characterization of a strain of *Methanospirillum hungatti*. *Can J Microbiol* **22**: 1404-1410.

Pritzker, K.P.H. (1998) Calcium pyrophosphate crystal formation and dissolution. In *Calcium phosphates in biological and industrial systems*. Amjad, Z. (ed). Norwell, Massachusetts: Kluwer Academic Publishers, pp. 277-299.

Rao, N.N., Gomez-Garcia, M.R., and Kornberg, A. (2009) Inorganic polyphosphate: essential for growth and survival. *Annu Rev Biochem* **78**: 605-647.

Remonsellez, F., Orell, A., and Jerez, C.A. (2006) Copper tolerance of the thermoacidophilic archaeon *Sulfolobus metallicus*: possible role of polyphosphate metabolism. *Microbiology* **152**: 59-66.

Rohlin, L., and Gunsalus, R.P. (2010) Carbon-dependent control of electron transfer and central carbon pathway genes for methane biosynthesis in the Archaean, *Methanosarcina acetivorans* strain C2A. *BMC Microbiol* **10**: 62.

Rudnick, H., Hendrich, S., Ulrich, P., and Biotevogel, K.-H. (1990) Phosphate accumulation and the occurrence of polyphosphates and cyclic 2,3-diphosphoglycerate in *Methanocarcina frisia*. *Arch Microbiol* **154**: 584-588.

Scherer, P.A., and Bochem, H.-P. (1983) Ultrastructural investigation of 12 *Methanosarcinae* and related species grown on methanol for occurence of polyphosphatelike inclusions. *Can J Microbiol* **29**: 1190-1199.

Southam, G., and Beveridge, T.J. (1992) Detection of growth sites in and protomer pools for the sheath of *Methanospirillum hungatei* GP1 by use of constituent organosulfur and immunogold labeling. *J Bacteriol* **174**: 6460-6470.

Stieb, M., and Schink, B. (1985) Anaerobic oxidation of fatty acids by *Clostridium bryantii* sp. nov., a sporeforming, obligately syntrophic bacterium. *Arch Microbiol* **140**: 387-390.

Chapter III

Discovery and characterization of iron-sulfide and polyphosphate bodies co-existing in *Archaeoglobus fulgidus* cells

Daniel B. Toso[1,2,3], Mohsen Javed[1], Elizabeth Czornyj[1], Robert P. Gunsalus,[13,4,*] and Z. Hong Zhou[1,2,3,*]

Department of Microbiology, Immunology, and Molecular Genetics[1];

Electron Imaging Center for Nanomachines, California Nano Systems Institute[2];

The UCLA Biomedical Engineering Interdepartmental Program[3];

The UCLA Institute of Genomics and Proteomics[4],

University of California, Los Angeles (UCLA),

Los Angeles, CA 90095

Running Title: **Iron-sulfide and polyphosphate bodies in archaea cells**

KEYWORDS: *Archaeaoglobus fulgidus,* polyphosphate energy storage granules, cryo-electron tomography, STEM elemental composition, cell positioning

*To whom correspondence should be addressed:

Cryo EM and biophysical analyses:Hong Zhou, Phone 310-983-1033 Hong.Zhou@ucla.edu

Microbiology: Robert Gunsalus: Phone 310-206-8201 robg@microbio.ucla.edu

SUMMARY

Inorganic storage granules have long been recognized in bacterial and eukaryotic cells, but only recently have been described in archaeal cells. In this study, we determine the cellular organization and chemical compositions of storage granules in the *Euryarchaean, Archaeoglobus fulgidus* strain VC16, a thermophilic, anaerobic microorganism that reduces sulfate in diverse ecosystems. Dense granules are very apparent in *A. fulgidus* cells imaged by cryo electron microscopy (cryo EM), which are either poorly or not seen in negatively stained cells or cell ghost preparations imaged by either negative staining or cryo EM. By cryo electron tomography (cryo ET), we observe that each cell may contain multiple dense granules, which are usually located at the cell periphery adjacent to the cell membrane. Elemental analysis by energy dispersive X-ray (EDX) spectroscopy and scanning transmission electron microscopy (STEM) reveals that each cell contains, surprisingly, two types of granules with totally different compositions. One type, named the iron-sulfide body (ISB), is composed mainly of iron, sulfur and copper; the other, called the polyphosphate body (PPB), is composed of phosphorous, oxygen, magnesium, calcium and aluminum. PPBs, which have been found in other archaeal and bacterial cells, are likely polyphosphate-containing granules used for energy storage and/or for metal ion sequestration. The newly discovered ISBs may result from the reduction of sulfate to sulfide via anaerobic metabolic pathways and thus be associated with energy and metal storage, metal detoxification or other metabolic processes. The exceptional ability of these cells to sequester different elements, including metals, into localized dense granules, may have novel bioengineering applications, and warrants further study.

INTRODUCTION

Archaeoglobus fulgidus is a hyperthermophilic, sulphur-metabolizing, anaerobic archaean. Belonging to the to the *Archaeoglobales* division of the *Euryarchaeota*, it is found in marine thermal vents, hot springs, and oil field waters. It can produce biofilms in response to stress which may be important for metal detoxification, surface adherence, and nutrient acquisition (Hartzell and Reed, 2006). *A. fulgidus* cells are used for metal sequestration in water treatment and, due to its thermophilc properties, can serve as a source of high temperature stable enzymes. Due to production of hydrogen sulfide, it has been implicated in oil souring and oil pipeline corrosion (Beeder et al, 1994).

A. fulgidus strain V16 is a sulfate reducing chemo-heterotroph. Initially isolated from marine hydrothermal vents in Italy (Stetter, K.O. 1988), this obligate anaerobe can utilize a variety of carbon compounds as electron donors for sulfate, sulfite or thiosulfate reduction to sulfide (Hartzell and Reed, 2006). Some strains are capable of chemo-lithotrophic growth and use hydrogen as an electron donor as well as nitrate as an alternative electron acceptor. *A. fulgidus* V16 cells are morphologically spherical to irregular coccoids in shape and some strains are motile by means of a single flagellum per cell (Stetter, K.O. 1988; Hartzel and Reed, 2006).

In this study, we employ a combination of cryo-electron microscopy, cryo-electron tomography, and EDX analyses to identify and characterize high-density inclusion bodies (also called granules) distributed within the *A. fulgidus* cytoplasm. We show that these structures of come in two types that can reach ~240 nm in diameter. They are rich in phosphorous and oxygen or iron and sulfur, and both are typically positioned nearby the cell membrane at opposite sides of the cell when the two types are present. Likely functions include phosphate, iron and sulfur storage and/or cell energy storage in the form of polyphosphate and iron-polysulfides.

RESULTS

Imaging of A. fulgidus *V16 whole cells and cell ghosts*

Initially, we imaged whole cells negatively stained with 1% UA by conventional TEM (Fig. 3-1A). However, due to the large size and thickness of the whole cells, the stain does not penetrate well and it is very difficult to visualize the interior of the cell. Consequently, negative stain TEM images do not routinely show evidence of the dense granules within the cells. In contrast, cells embedded in vitreous ice directly imaged by cryo electron microscopy (cryo EM) without staining clearly reveal the presence of electron dense granules in each cell (Fig. 3-1B). However, the contrast of the cryo EM images is limited by the use of low dose exposure necessary to minimize radiation damage to the cell.

Next, *A. fulgidus* cell ghost preparations were made from whole cells as described in Materials and Methods and imaged after being negatively stained with a 1% uranyl acetate solution (Fig. 3-1C). The ordered S-layer coat surrounding the cell membrane is apparent whereas the granules usually present within are either absent or do not appear as uniformly dark electron dense bodies. This may be due to their loss or disintegration during the ghost preparation process, whereby most of the cellular cytoplasm is extracted leaving behind the cell membrane with attached S-layer proteins. While this preparation leaves behind cell ghosts that are easily stained and visualized due to their ability to flatten on the carbon surface of the grid, the loss of the cell contents does not allow visualization of the dense granules.

The same cell ghost preparation was frozen in vitreous ice and imaged by cryo EM. The *A. fulgidus* cell ghosts visualized this way have very poor contrast due to the thinness of the sample, so 3D tomograms were reconstructed after collecting tilt series by cryo electron tomography (cryo ET) (Fig. 3-1D). This, however, did not allow routine visualization of intact dense granules within the cell, as most of the cellular contents were extracted. It does appear that remnants of the granules, possibly attached to the cellular membrane, can occasionally be

visualized within the cell ghosts (circled in Fig. 3-1D). There also appear to be cell envelope associated structures or scars, which may have been granule assembly sites (arrows).

3D visualization of inclusion bodies within* A. fulgidus *cells by cryo ET.

Next, we used cryo ET to reconstruct whole cells in three dimensions. Visualizing cells embedded in vitreous ice preserves their structures in a natural state and eliminates the artifacts associated with staining (Fig. 3-1A). These cryo ET reconstructions of *A. fulgidus* cells reveal that they have a typical S-layer envelope surrounding the cellular mono-layer membrane composed of C40 isoprenoid di-ether lipids (Lai. et al, 2008). The reconstructions also show that the *A. fulgidus* cells are irregular, coccoid shaped and approximately 1 µm in diameter. The clearly visible cell membrane (~37 Å thick) is surrounded by a uniform S-layer of ~110 Å in thickness. These two structures are separated by a periplasmic-like space (~130 Å) (Fig. 3-2A).

The most apparent feature within the cytoplasm of the cell is the presence of one to two electron dense inclusion bodies. The presence of these high density inclusion bodies has not been previously described in *A. fulgidus*. The granules vary from roughly spherical to ellipsoidal with smooth rather than angular surfaces (Fig. 3-2A-C).

Based on density, granules can be classified as newly developed or developed. Newly developed granules are frequently observed within cells undergoing exponential growth phase (Sup. Fig. 3-S1). They appear to be composed of very small particles that have clustered into a closely packed, roughly spherical shape (Fig. 3-2A, upper granule). Granules that are developed do not exhibit the particulate appearance and are more rounded in shape (Fig. 3-2A, lower granule and Fig. 3-2C). Repeating or ordered arrangements were not observed either visually as a crystalline pattern in the packing of the TEM image or in the Fourier transform (FT) of the images of the inclusion bodies (Fig. 3-2B).This evidence suggests that the bodies have an amorphous arrangement that would allow packing of smaller molecules into the structure.

Inspection of freeze-thaw prepared cell ghosts reveals apparent disintegration of granules as evidenced by many small particulate fragments.

Cells in stationary phase exhibited a characteristic arrangement in which two dense, developed granules are present on the periphery of the cell (Fig. 3-2C). When these cells are reconstructed in three dimensions by cryo ET, it is further observed that each of the granules are positioned very close to the cell membrane, often appearing to touch the surface of the cell, locally deforming it (Fig. 3-2D). This suggests that the granules are positioned intentionally adjacent to the membrane and may be associated with one or more membrane activities within the cell.

By examining the 3D tomograms of cells containing dense bodies we were able to compile size and localization data. The granules are positioned close to the edges of the cell, with an average distance of around 50 (+/- 18) nm from the cell membrane (Fig. 3-3A). Along with this their shape appears to be ellipsoidal, with a size distribution slightly longer along the axis of the cell membrane with an average size of 243 (+/- 30) nm parallel to the membrane and 223 (+/- 22) nm perpendicular to the membrane (Fig. 3-3B,C). This seems to suggest that the granules are specifically localized near the membrane and in many instances locally deform the membrane surface (Ca along ~200-300 uM).

Elemental composition of granules

Intracellular granules have been characterized in bacteria and other archaea utilizing both energy-filtered TEM (EELS) and energy dispersive X-ray spectroscopy (EDX) in order to analyze the elemental composition of the inclusion bodies (Scherer and Bochem, 1983; Lechaire *et al.*, 2002; Remonsellez *et al.*, 2006). An FEI Titan STEM instrument was employed to collect EDX spectra to analyze the elemental composition of the inclusion bodies within representative *A. fulgidus* cells as previously described (Toso *et al.*, 2011).

Initially, element line spectra across the *A. fulgidus* bodies was obtained by scanning the electron probe along a line across the sample, and the spectra revealed a high abundance of phosphorous and oxygen within the granule region (Fig. 3-4A,B). Individual point spectra in the region of the granule show that, in addition to phosphorous and oxygen, calcium, magnesium, copper and aluminum are also concentrated in the dense bodies (Fig. 3-4C). The high concentration of phosphorous and oxygen along with the cationic elements is consistent with our previous results demonstrating the presence of poly-phosphate bodies (PPBs) in *Methanospirillum hungatei* JF1 (Toso *et al.*, 2011). The demonstration of these very concentrated PPBs in a second *Euryarchaeota* species was encouraging, but upon further EDX analysis we found some of the granules had very different spectra.

Area scan spectra, or dot-mapping, were obtained by scanning specific areas of additional cells that included one or more inclusion bodies, and some of these area scans showed high concentrations of iron and sulfur, not phosphorous and oxygen, within the bodies (Fig. 3-5A,B). Examining individual point spectra in the region of these new granules showed that not only were sulfur and iron highly concentrated, along with copper. Phosphorous, oxygen, magnesium, calcium and aluminum were not concentrated compared to surrounding cellular cytoplasm (Fig. 3-5C). This new type of granule, named iron sulfur bodies (ISBs), in which iron and sulfur are concentrated, are suspected to be composed of ferrous sulfide (Fe-S) or Fe-polysulfide (Fe-[S_n]). Either would form from the reduction of sulfate (SO_4^{2-}) to hydrogen sulfide (H_2S) during the crucial anaerobic respiration processes needed for cell energy production and survival. Conceivably, Fe-polysulfide may be formed from an intermediate of the sulfate reduction pathway and serve as an energy rich storage material. The Fe-polysulfide would be subsequently reduced to sulfide (HS^-) for energy harvesting. Alternatively, these dense granules containing high concentrations of iron and sulfur may serve as a metal storage and/or detoxification device.

In many cells there were found to be two granules present (Figs. 2, 4, 5, and 6). When granules were found that contained high concentrations of iron and sulfur and identified as ISBs (Fig. 3-5A-C) the second granule in these cells was subsequently analyzed and found to be composed of elevated concentrations of phosphorous and oxygen along with calcium, magnesium, copper and aluminum, therefore identified as PPBs (Fig. 3-5D,E). Line scan spectra across the cell and examination of the individual point spectra in the granule region show the characteristic PPB elemental composition seen before (Fig. 3-5F). The individual co-localization of the two types of granules within the same cell was repeatedly observed.

In order to confirm the co-localization of granule types, area scan spectra were performed which contained both granules within the same cell. The area scans again reveal that each granule had very different compositions, one contained high concentrations of sulfur and iron while the other had high concentrations of phosphorous and oxygen (Fig. 3-6A,B). Contrasting the individual point spectra from within each granule in the cell confirmed the very different compositions and showed the characteristic spectra shown previously for ISBs and PPBs in this cell type (Fig. 3-6C).

Effect of cell nutrition on dense body formation

The ability of *A. fulgidus* cells to form the two body types depends, in part, on the composition of the cell culture medium. When phosphate was limited, no bodies were formed. The main effect of limiting specific nutrients in the culture medium manifested in the cell morphology. Reduced phosphate and lactate caused cells to grow to be less dense and smaller in size when observed in negative stain (Sup. Fig. 3-S2). No phosphate initially caused cells to appear further shrunken (Sup. Fig. 3-S2 panel E). After treating for three generations under the altered conditions, having no phosphate in solution did not allow cells to even proliferate (Sup. Fig. 3-S3). Cryo EM images of cells with reduced phosphate show a clear reduction in size compared to normal concentrations.

DISCUSSION

Granules in *A. fulgidus* strain V16 were characterized by their composition, size and locations within the cell. The elemental compositions of the PPB and ISB granules clearly distinguish these two intracellular structures. The former lacks the iron and sulfur elements abundant in the ISB's while the ISBs lack the phosphate and oxygen abundant in the former. Likewise, the less abundant elements present in the PPBs: magnesium, calcium and aluminum, are absent in the Fe-S bodies and the PPB's lack iron. The ratios of the predominant elements seen in PPBs and ISBs are diagnostic: whereas the former exhibits characteristic oxygen phosphorous ratio of 2:1, the latter has an iron sulfur ratio of 1:2. This provides a potential basis for high throughput STEM assisted screening of cells to characterize granules in A*. fulgidus* and related archaeal strains. Further analysis of the variation in density between granule types and at different stages of development are also possible.

What are the functions of the PPB and ISB granules? Considerable discussion has been tendered on roles for PPBs over the past thirty years (Kulaev and Kulakovskaya, 2000; Kulaev, et al, 1999; Rao, et. al. 2009; Kornberg et. al. 1999). These include cell energy capture and storage to support of diverse cell functions including chromosome replication and cell division. Other roles include phosphate storage, metal chelation and metal detoxification. In contrast, the role(s) of the newly described ISB granules are not known. Besides the afore mentioned roles in energy and iron storage, ISB granules may be involved in metal sequestration and detoxification. *A. fulgidus* species thrive in highly reducing and metal rich environments. Fluids flowing from hydrothermal vents, for example from black and white smoker vents, are reported to contain low to high uM amounts of calcium, copper, zinc, iron, manganese and strontium (Kelley, et. al., 2002). Nearby sea waters rich in dissolved magnesium, phosphate and sulfate also recirculate within these vent habitats. Finally, the black and white smokers also have associated metal precipitates and soluble by-products that are formed and that may prove toxic to nearby microbes.

Noteworthy, both PPB and ISB granules are positioned in characteristic locations nearby or at cell cytoplasmic membrane surface. This uniform location suggests that cells possess a means to position each granule type, presumably to facilitate accumulation of cell nutrients from the environment for storage, and utilization as cell reserves. We speculate that associated enzyme machinery reside at or nearby the cell membrane to facilitate their formation and utilization. For example, for PPBs, this membrane location could coordinate accumulation of phosphate from the cell exterior via high affinity uptake systems (e.g., AF0791, AF1356-1360, AF1798) with co-localized polyphosphate polymerizing enzymes for granule formation. By another scenario, a poly-phosphate driven proton pump would operate to generate a proton gradient when needed by the cell. This pump might also run in the reverse direction by utilizing proton import to form polyphosphate inside the cell.

The presence of putative EM visualized structures or scars along the inner surface of the cytoplasmic membrane (sup figure x) suggests this potential for associated enzyme machinery to accomplish one or more of the above processes. Conceivably, poly-sulfur forming enzymes could be associated with the ISB's and it has been previously shown that *A.fulgidus* cells are capable of metabolizing thiosulfate (Hartzell and Reed, 2006). Tests of these ideas must await the development of genetic tools for *A. fulgidus*.

From the Cryo EM measurements of the *A.fulgidus* cell envelope dimensions we can accurately assess/document the cell compartment surface areas and volumes. A one micron diameter spherical cell would have an overall cell volume of 0.524 μm^3 where the volume, V = (4/3) pi r^3. Using the following measures of the cell membrane ~37 angstroms thick, the S-layer lattice is ~110 angstroms thick, and the low electron density periplasmic-like space that separates these two structures is ~130 angstroms thick (Fig. 3-2A), the *A.fulgidus* volume is partitioned into cytoplasm (84.3% or 0.441 μm^3), membrane (2.1% or 0.011 μm^3), periplasm (7.2% or 0.038 μm^3), and surface layer (6.4% or 0.034 μm^3). The intracellular PPB and ISB

granules observed in *A.fulgidus* cells can individually compose up to 1.4% of the cytoplasmic space (~230 nm diameter).

There are few documented examples of inorganic storage granules present in the archaea in contrast to the many recognized granules in bacterial and eukaryotic cells (review article). We recently/previoulsy reported the presence of PPBs in the methanogen *Methanospruillum hungatgei* JF1 (Toso et al., 2011). The bodies were spherical (Ca. 100 nM in diameter) and localized nearby but not on the membrane at the cell ends. Interestingly, they also differed from the PPB's reported in this study in that they contained iron whereas the *A. fulgidus* V16 PPB's lack iron. These STEM data suggests different sub-classes of PPBs occur in the archaea and more research appears justified to understand the nutritional/genetic basis for these observations. Early reports of PPB's in several other archaea including several *Sulfolobus* and *Methanosarcina* species (Remonsellez et al., 2006; Scherer and Bochem, 1983) and elemental analysis has reported some metal compositions, including iron. In this study we also examined the effect of cell nutrition on *A. fulgidus* V16 granule formation. Limiting cells for carbon supply or phosphate resulted in formation of few or no PPB's or ISB's. This is consistent with observations that cells monitor the environment and adapt physiologically.

Both granule types (PPSs and ISBs) present in *A. fulgidus* strain V16 are positioned in characteristic membrane-adjacent locations (Fig. 3-2 & 3). These uniform locations suggests a means to position each type of granule and that the cell possesses the genetic ability to spatially (and presumably temporally) program granule accumulation/utilization. Interestingly, inspection of negative stained cell sections of the *A. fulgidus* V16 related strain, *A.fulgidus* strain 7324, revealed the presence of dark bodies adjacent to the cell membrane (Figure 1; Beeder et al, 1999). Although not identified or described by the authors of that study, these electron dense bodies likely contain polyphosphate (PPBs) and/or Fe-S (ISBs) described in this study.

EXPERIMENTAL PROCEDURES

Cell culture.

A. fulgidus strain V16 (DMS 4304) cells were cultured at 83°C in an anaerobic CO_2/bicarbonate buffered mineral medium supplemented with vitamins and sodium lactate as previously described (Rohlin et al., 2005). The medium consisted of 1L of ultra-pure water, 18g NaCl, 3.4 g $MgSO_4$ -7 H_2O, 2.8 g $MgCl_2$ - $6H_2O$, 0.5 g NH_4Cl, 0.5 g KCl, 0.55 g KH_2PO_4, 0.14 g $CaCl_2$ - $2H_2O$, 1 mL of a 1000x H^+ trace mineral solution (50 mM HCl, 1 mM H_3BO_3, 7.5 mM $FeCl_2$, 5 mM $NiCl_2$, 0.5 mM $MnCl_2$, 0.5 mM $ZnCl_2$, 0.5mM $CoCl_2$, 0.5 mM $CuCl_2$, 0.5 mM $CuCl_2$, 0.5 mM $AlCl_2$), 1 mL of a 1000x OH trace mineral solution (10 mM NaOH, 0.1 mM Na_2SeO_3, 0.1 mM Na_2WO_4, 0.1 mM Na_2MoO_4), and 1 mL of 1000x vitamin solution (Balch et al., 1996). Sodium lactate was added to a final concentration of 20 mM. The medium was flushed with a N_2/CO_2 (80:20) gas mixture to remove oxygen and then dispensed into N_2/CO_2 flushed glass bottles. The bottles were then sealed with butyl rubber stoppers and crimp aluminum caps. The medium was autoclaved at 121 ℃. Prior to inoculation, the medium was supplemented with a sterile anaerobic stock solution of 2.5% $Na_2S \cdot 9H_2O$/2.5% Cysteine HCl (1% v/v) and 1M $NaHCO_3$ (2% v/v) to reduce the medium and adjust it to pH 7.0.

Preparation of A. fulgidus *cell ghosts.*

Cells grown as described above (500 mL of culture) were divided into two equal portions and harvested by centrifugation at 5,000 x g for 45 minutes at room temperature. Pellets were re-suspended in 1 mL of "Wash Buffer" (18 g L^{-1} NaCl, 3.4 g L^{-1} $MgSO_4$- $7H_2O$, 2.8 g L^{-1} $MgCl_2$ - $6H_2O$, 0.147 g L^{-1} $CaCl_2$ - $2H_2O$, 20mM KH_2PO_4, adjusted to pH 7 with NaOH) and transferred to a 2 mL microfuge tube. The cells were centrifuged at 13,500 RPM for 1 minute and the pellet was washed three additional times in 1 mL of Wash Buffer. The pellet was re-suspended by gentle pipetting up and down. After the final cell wash, the pellets were suspended in 1 mL of "Wash Buffer" containing 1µl of DNAse (10 µg/ml) and 1µL of RNAse (10 µg/ml). This cell

suspension was then immediately frozen in a dry ice/ethanol bath. Immediately after freezing it was then allowed to completely thaw in a water bath at room temperature. The freeze/thaw step was repeated 5 additional times. The cell suspension was then centrifuged at 13,500 RPM for one minute and the supernatant was transferred to a 2 ml microfuge tube.

The pellet was washed three times in a “Low Salt buffer” by suspending the pellet in 1 mL of the low salt buffer and pipetting up and down. The cells were then centrifuged at 13,500 RPM for 1 minute. Once the pellet was washed three times, it was then suspended in 1 mL of “Low Salt Buffer” and stored at -70℃.

Preparation of* A. fulgidus *cell ghosts without “Low Salt Buffer”.

The cells were treated essentially the same as mentioned above except that following the 6 freeze/thaw cycles, the cells were not further washed with the “Low Salt” buffer. The cell suspension was stored at -70℃.

Electron microscopy

For negative stained TEM, copper EM grids with carbon-coated Formvar film were glow-discharged and followed by placement of a small droplet (~4 µl) of *A. fulgidus* cell suspension onto the carbon side of each grid. After one minute at room temperature, the excess of the sample droplet was blotted from the side of the grid and a droplet of 1% uranyl acetate solution was immediately placed on the grid. After the stain sat for one minute it was blotted off and the staining/blotting step was repeated four times to remove any excess sample from the grid. After air drying, the grid was observed in an FEI Tecnai F20 transmission electron microscope operated at an accelerating voltage of 200 kV to assess the concentration of cells on the grid. To adjust concentration, cells were centrifuged at low speed (13,500 RPM) in a table-top microfuge, and re-suspended in culture medium.

To prepare ice-embedded cells for cryo EM observation or cryo ET, 100 µl of cell solution with optimized concentration was mixed with 4 µl of 10 nm protein-A gold solution and

mixed thoroughly. A droplet (4 µl) of this mixed solution was placed onto a glow discharged, 200 mesh Quantifoil holey carbon grid with a spacing of 3.5 µm hole/ 1 µm edge. The sample was allowed to settle for 30 seconds, blotted by filter paper, and immediately plunged into liquid nitrogen cooled liquid ethane.

A Gatan 626 cryo sample holder and the above-mentioned Tecnai F20 electron microscope were used to image the *A. fulgidus* cells imbedded in vitreous ice on a 16 megapixel TVIPS CCD camera.

Cryo electron tomography

For the cryo ET reconstructions we used an FEI Titan Krios instrument operated at an accelerating voltage of 300kV and equipped with a Gatan image filter (GIF) 2002 camera. During tilt series acquisition, we chose cells whose long axes were roughly parallel to the tilt axis of the microscope. The cells were imaged at ~30,000x. An underfocus value of 6 µm was targeted for all images in the tilt series. All tomography tilt series were recorded using the FEI Batch Tomography software with a tilt range from -70^{o} to $+70^{o}$ and 2^{o} increment. The total electron dosage on the sample is 200 $e^{-}/Å^{2}$ for each tilt series.

Cryo ET data analysis and 3D visualization

The tomography tilt series were processed with a suite of programs to generate 3D reconstructions. Alignment of the tilt series was performed using the etomo tomography processing software from the Imod package (Kremer et al., 1996). The steps included X-ray removal, rough alignment by cross-correlation, fine alignment by fiducial gold tracking, and tilt-axis adjustment. The aligned tilt series were then used to make 3D reconstructions using weighted back-projection reconstruction in etomo or GPU-based SIRT (Simultaneous Iterative Reconstruction Technique) reconstruction implemented in Inspect3D. The 3D reconstructions were saved as stacks of X-Y plane images that are single pixel slices along the Z-plane. Slices from the reconstructions were displayed using slicer within 3dmod from the Imod package.

Amira (Visage Imaging GmbH, http://www.amira.com/) was used to create volume renderings of the 3D density maps of the cells.

STEM and EDX analysis

STEM imaging and EDX analysis were performed using an FEI Titan 80-300kV scanning transmission electron microscope. *A. fulgidus* cells were placed on carbon coated copper grids, air-dried and imaged inside the Titan instrument.

FEI TEM Imaging and Analysis (TIA) software package was used to acquire the line scan and area scan EDX spectra of different areas of the sample at 300kV. The spectral data for the indicated elements were stored as counts over distance or area. The TIA software package was used to output the individual point spectra as well as to generate the line scan and area plots.

Acknowledgements

This research was supported in part by the Department of Energy Biosciences Division grant award DE-FG03-86ER13498 and the UCLA-DOE Institute of Genomics and Proteomics to RPG and the National Institutes of Health (NIH; GM071940to ZHZ). We acknowledge the use of electron microscopy facilities at the UCLA Electron Imaging Center for NanoMachines in California NanoSystems Institute (CNSI) supported by NIH (1S10RR23057 to ZHZ).

FIGURES

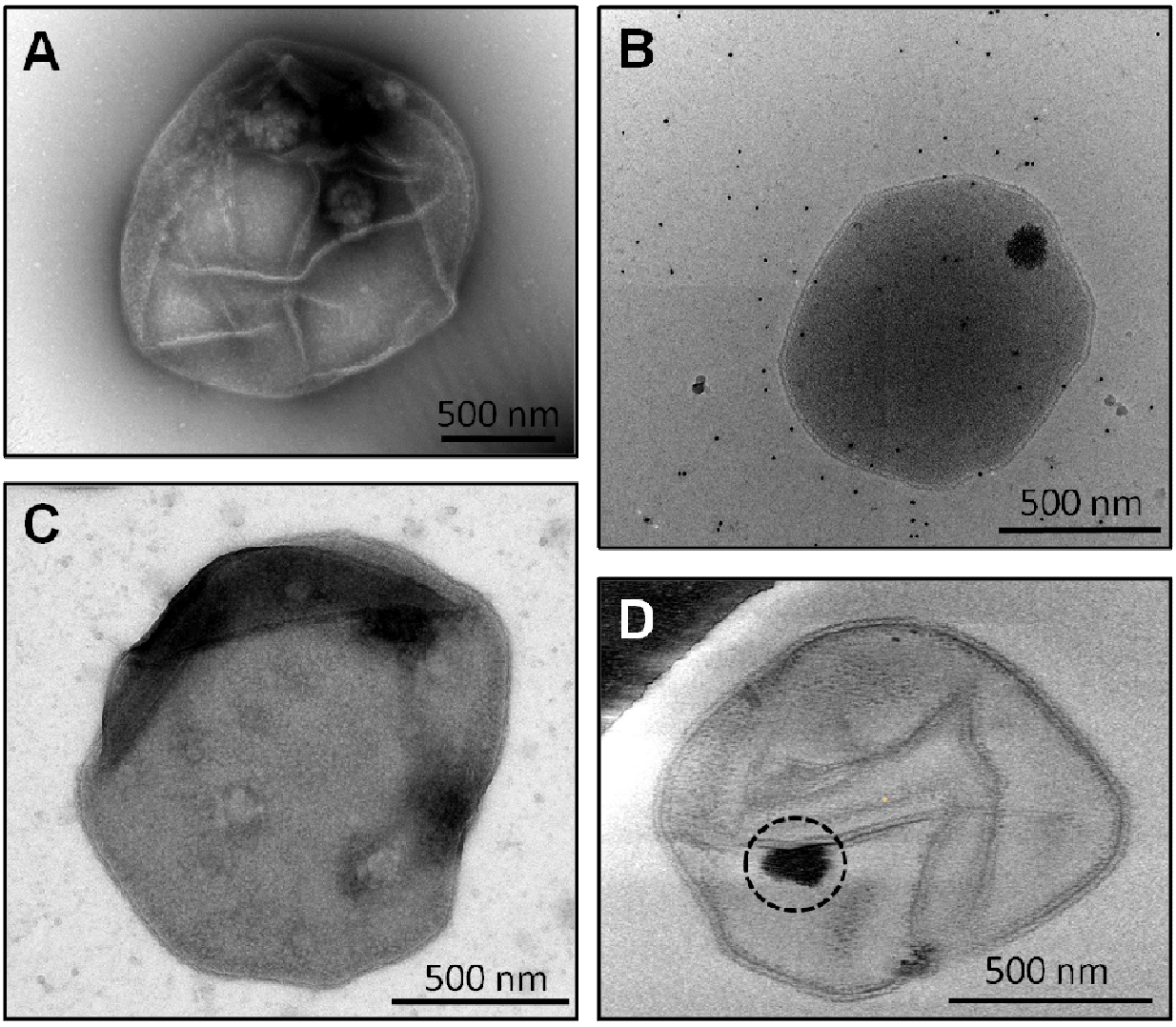

Fig 3-1. Electron microscopy of *A. fulgidus* cells and visualization of intracellular granules.

(A,B) Transmission electron microscopy images of an A. fulgidus cell stained by 1% uranyl acetate (UA) (A) or embedded in vitreous ice (B). (C,D) Representative TEM images of cell ghosts of *A. fulgidus* stained with UA (C) or embedded in vitreous ice (D). The remains from a possible dense granule are circled (D).

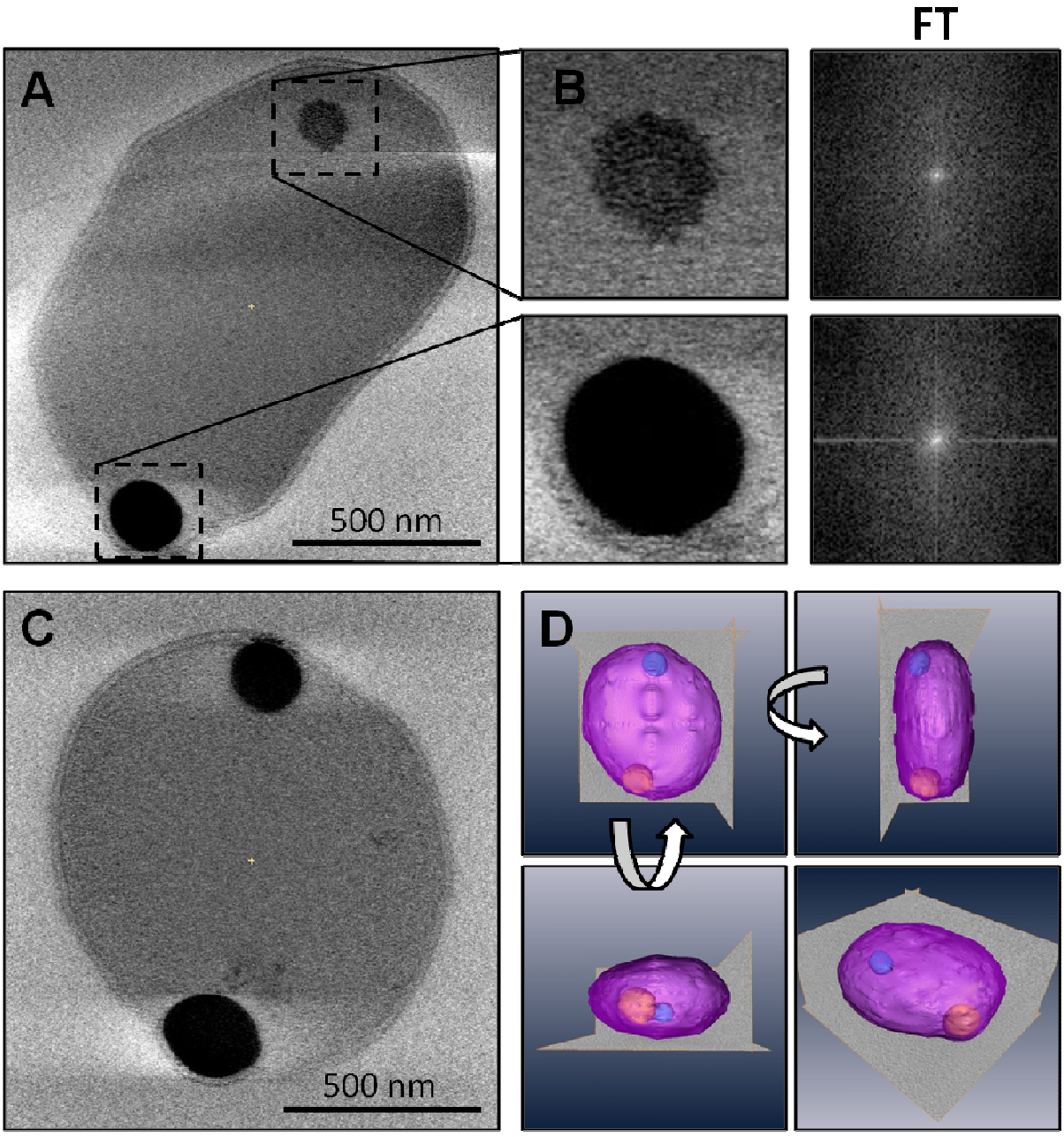

Fig 3-2. Cryo ET tomography of *A. fulgidus* cells reveals dense cytoplasmic bodies.

A) Central slice from a 3D tomogram reconstructed from a cryo ET tilt series of a whole cell frozen in vitreous ice. B) The two granules present in (A) are enlarged to show their amorphous features. The FT of each granule is shown on the right. C) Central slice from the 3D tomogram of another cell. D) 3D rendering of the cell in (C) shown from different angles. The cell is shown in pink, the 2 granules in blue and yellow.

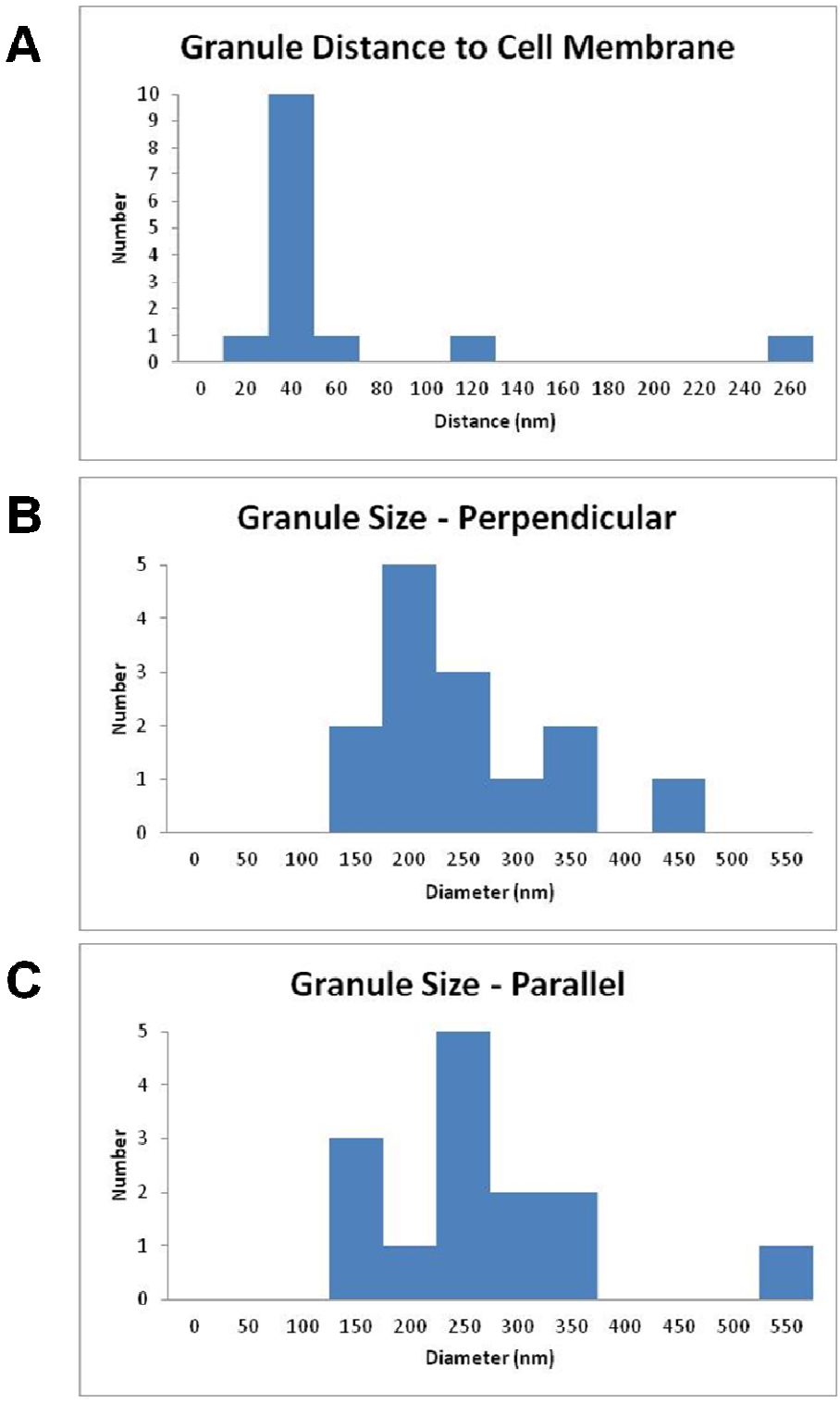

Fig 3-3. Size and location distribution of Granules in *A. fulgidus* cells

(A) Distance of granules from the cell membrane. (B) Diameter of granules perpendicular to the cell membrane. (C) Diameter of granules parallel to the cell membrane.

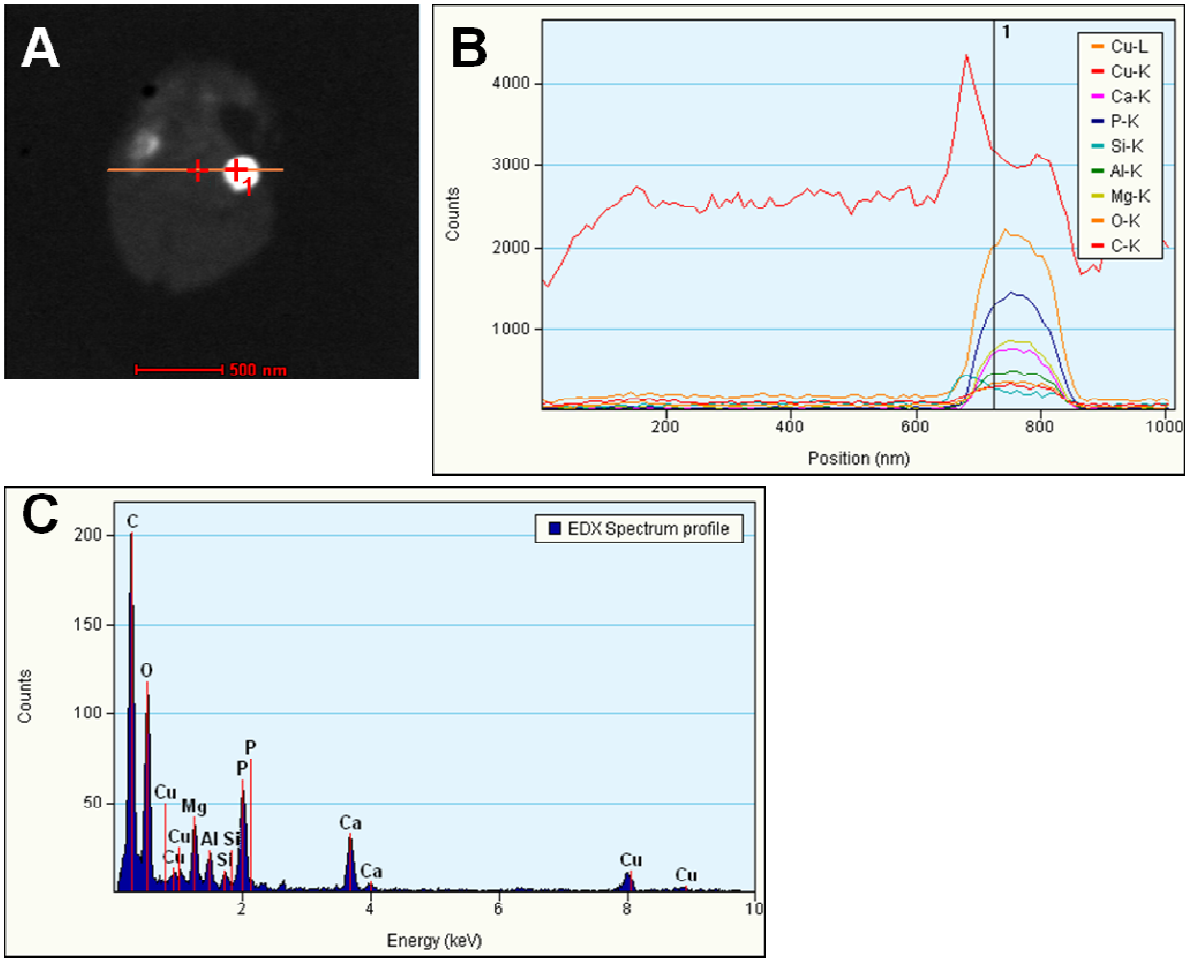

Fig 3-4. Elemental composition through a granule cross section by EDX analysis.

A) STEM image of the analyzed cell, the path of the probe is shown as an orange line. B) The EDX line spectra across the cell shown in (A). Each element is plotted in a different color. C) The individual EDX point spectrum from the location specified in (A) by a cross with the number 1and in (B) by a vertical line.

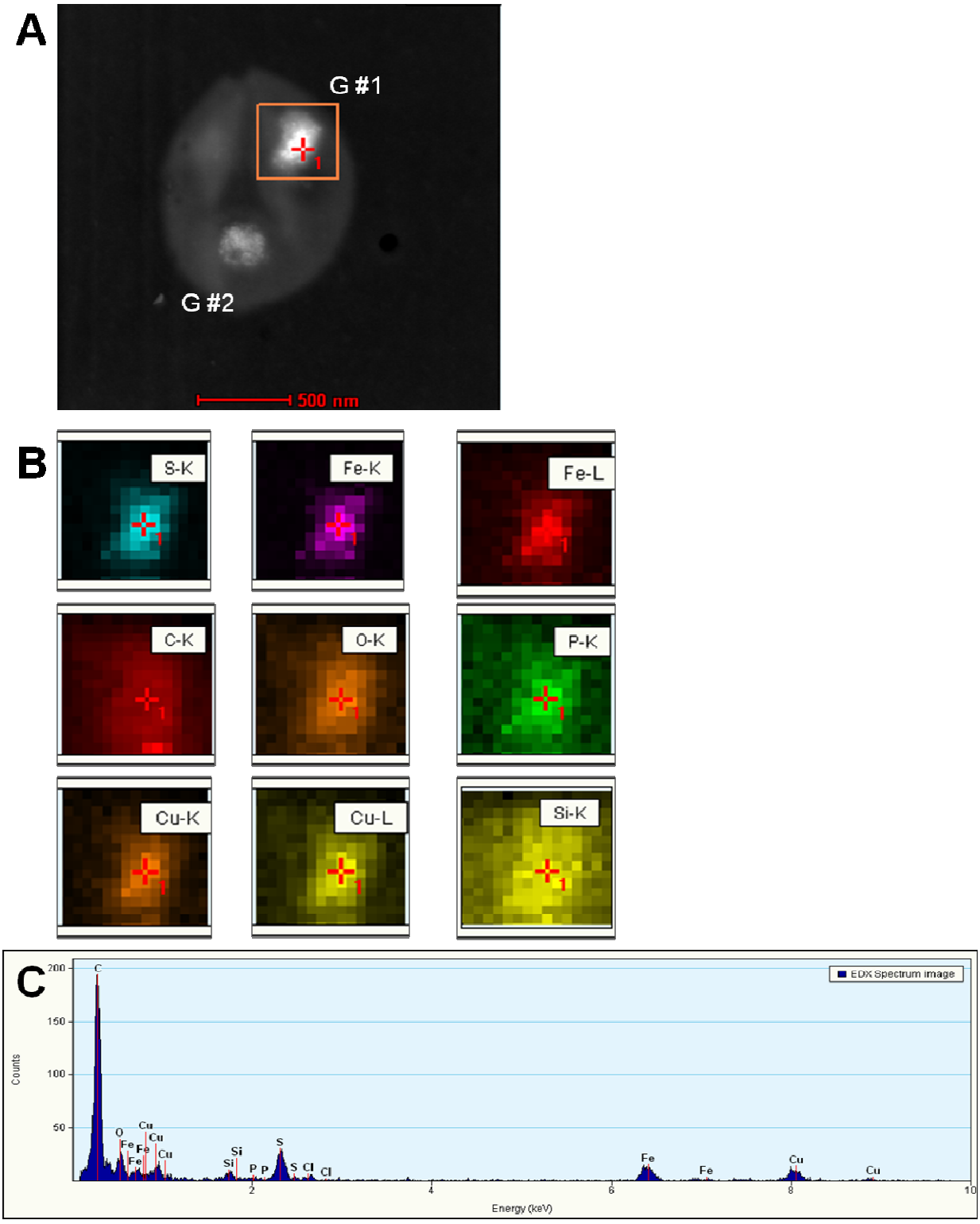
A
G #1
G #2
500 nm
B
S-K
Fe-K
Fe-L
C-K
O-K
P-K
Cu-K
Cu-L
Si-K
C
EDX Spectrum Image
Counts
Energy (keV)
C
O
Fe
Fe
Fe
Cu
Cu
Cu
Si
Si
P
P
S
S
Cl
Cl
Fe
Fe
Cu
Cu

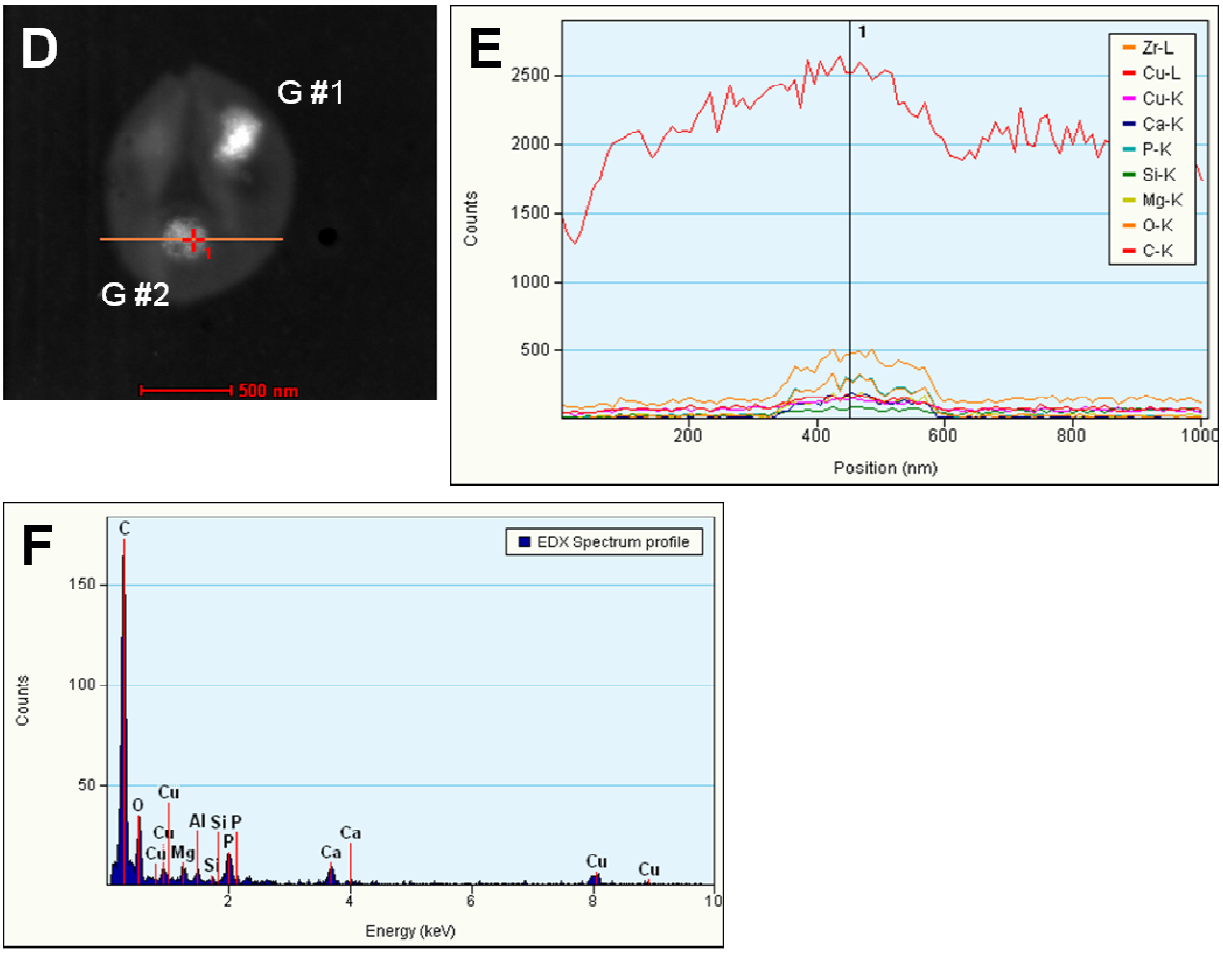

Fig 3-5. Separate EDX analysis of two granules in a single intact *A. fulgidus* cell.

A) STEM image of the analyzed cell, the first area scanned by the probe is shown as an orange box. The two granules are labeled G#1 and G#2. B) The EDX area scans for each element found in the region specified in (A), which contains G#1. Each element is plotted in a different color. C) The individual EDX point spectrum from the location specified in (A) and (B) by a cross with the number 1. D) STEM image of the analyzed cell, the path of the probe for the second scan is shown as an orange line. E) The EDX line spectra across the cell shown in (D), which contains G#2. Each element is plotted in a different color. F) The individual EDX point spectrum from the location specified in (D) by a cross with the number 1 and in (E) by a vertical line.

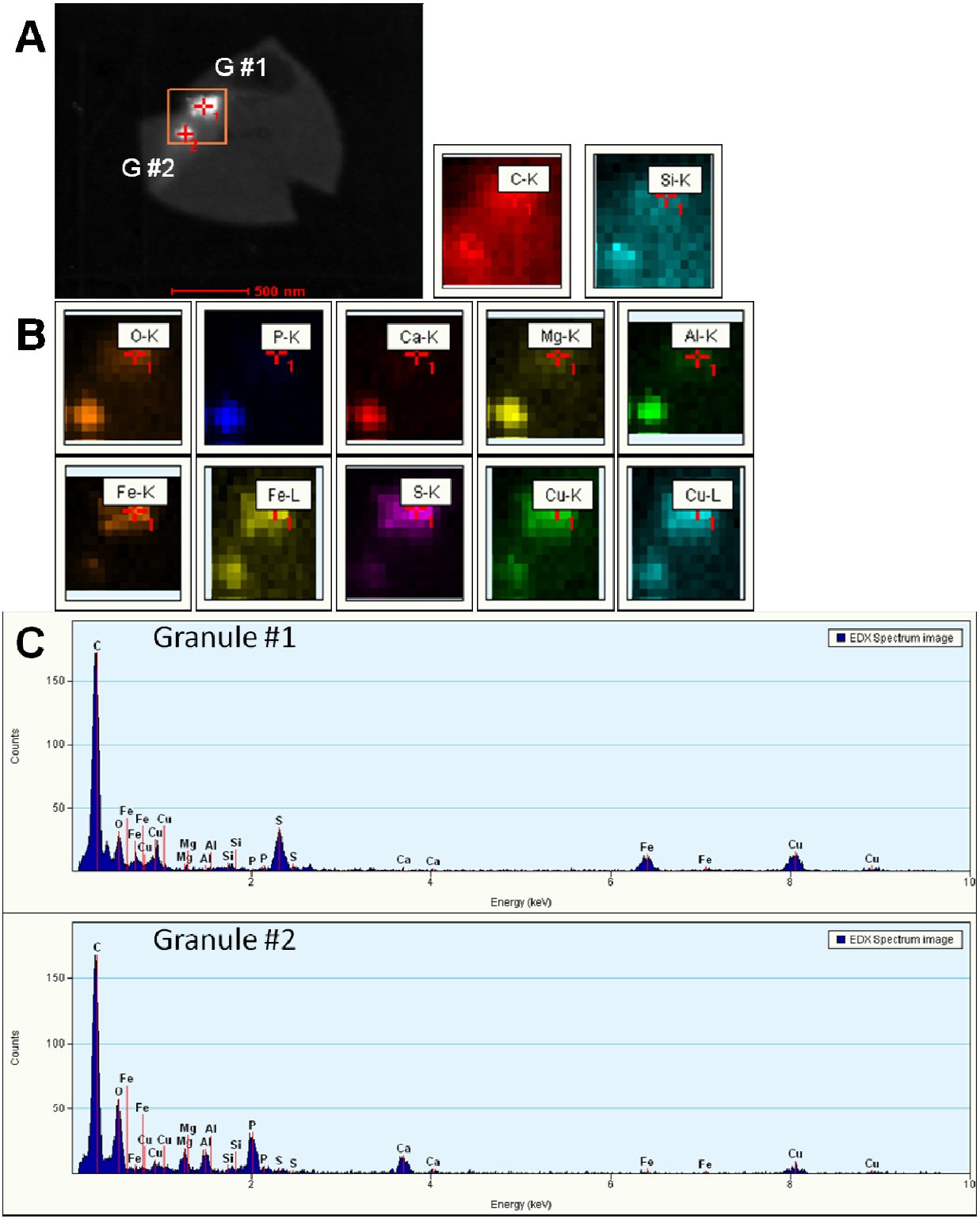

Fig 3-6. Combined EDX analysis of two granules in a single *A. fulgidus* cell

A) STEM image of the analyzed cell, the area scanned by the probe is shown as an orange box. The two granules are labeled G#1 and G#2. B) The EDX area scans for each element found in the region specified in (A), which contains both G#1 and G#2. Each element is plotted in a different color. C) The individual EDX point spectra from the locations specified in (A) by crosses with the numbers 1 and 2. The first spectrum is from G#1 and the second is from G#2.

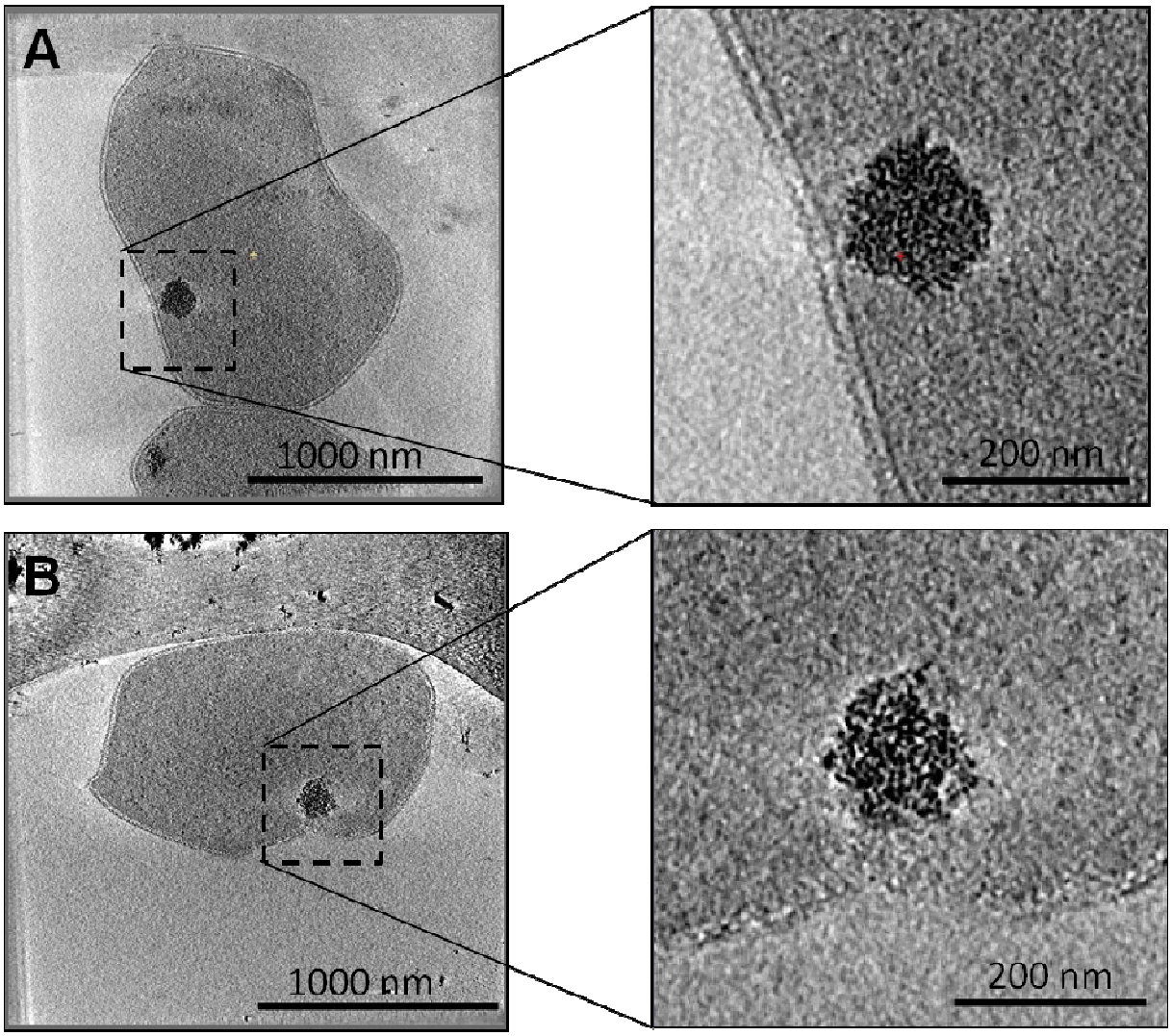

Sup Fig 3-1. *A. fulgidus* cells in growth phase showing newly developed granules.

A,B) Slices from 3D tomograms reconstructed from cryo ET tilt series of *A. fulgidus* whole cells in growth phase. The insets show the granules present within each cell at higher magnification.

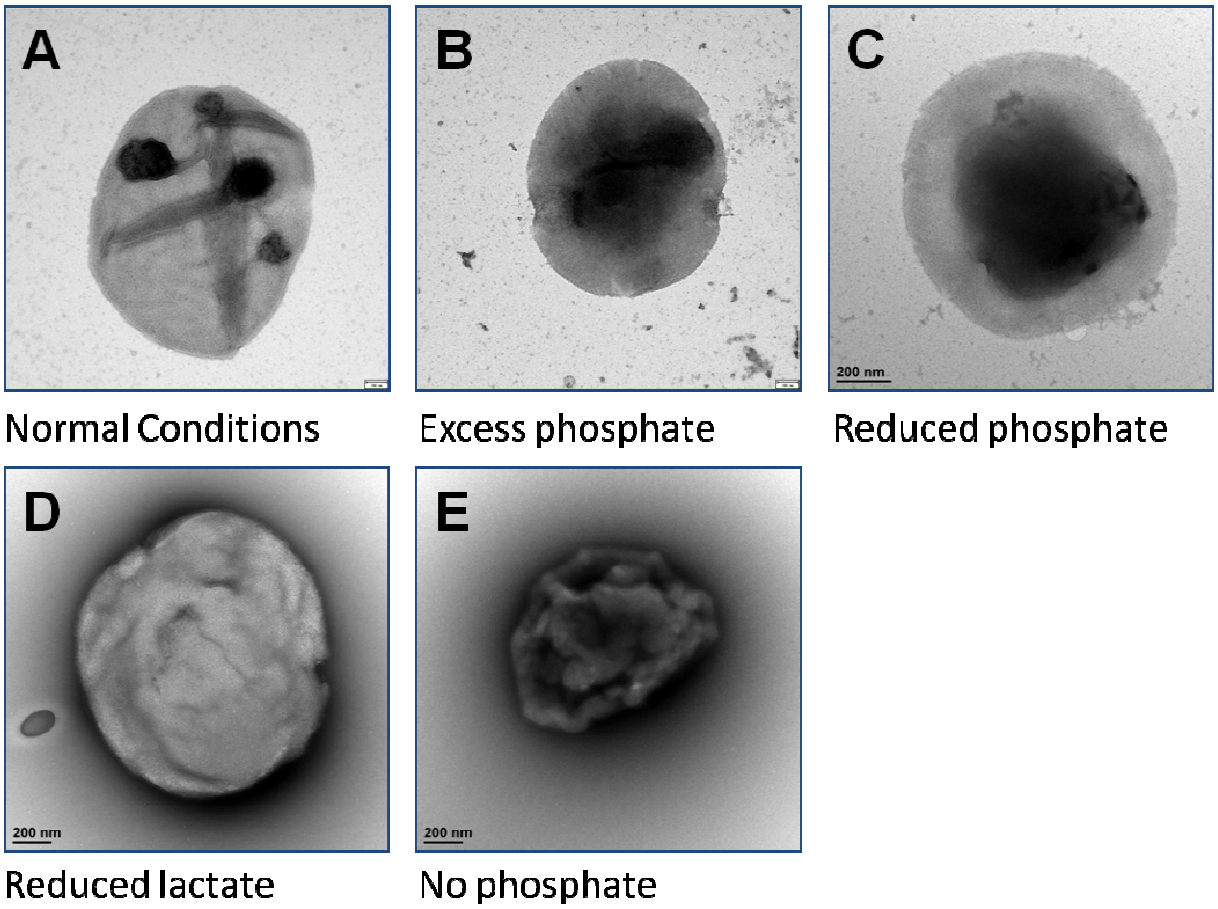

Sup Fig 3-2. *A. fulgidus* development under varying nutritional conditions

A-E) TEM images of (A) a cell grown in normal conditions, (B) a cell grown with excess phosphate, (C) a cell grown with reduced phosphate, (D) a cell grown with reduced lactate, and (E) a cell grown with no phosphate. All samples were negatively stained with 1% UA.

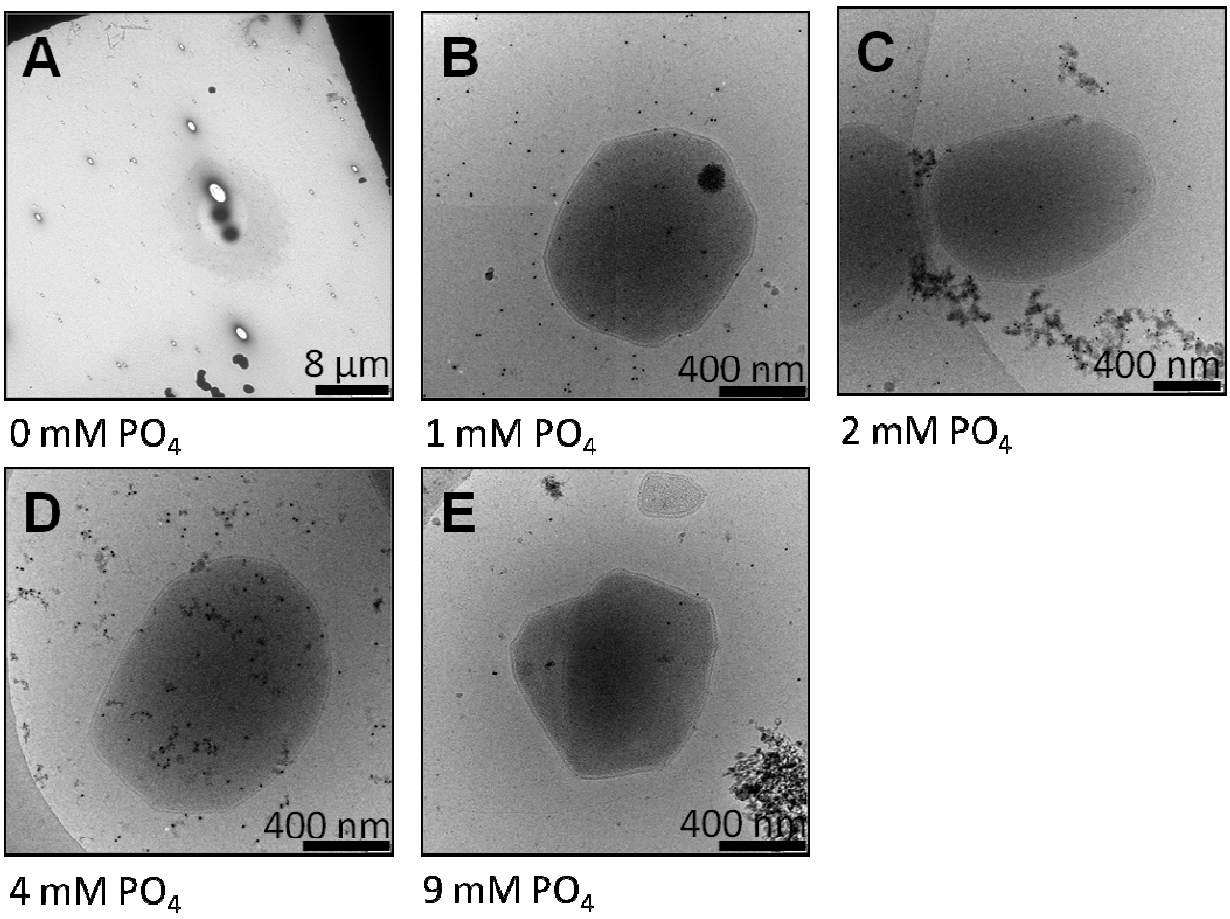

Sup Fig 3-3. Cryo EM of *A. fulgidus* cells after three generations of reduced or elevated phosphate conditions.

A) Low magnification image of a TEM grid, stained with 1% UA, of a sample grown with no phosphate. Almost no cells are present. B-E) Cryo EM images of cells grown in (B) 1 mM phosphate, (C) 2 mM phosphate, (D) 4 mM phosphate (normal conditions), and (E) 9 mM phosphate.

REFERENCES

Balch, W. E., G. E. Fox, L. J. Magrum, C. R. Woese, and R. S. Wolfe. 1996. Methanogens: reevaluation of a unique biological group. *Microbiol. Rev.* **43**:260–296.

Beeder, J., Nuiesen, R.K., Rosnes, J.T., Torsvik, T., and Lein, T. (1994) Archeaoglobus fulgidus isolated from hot north sea oil field waters. *App. Environ. Microbiol.* **60**:1227-1231.

Hartzell, P. and Reed, D.W. (2006) The Genus *Archaeoglobus*. *The Prokaryotes* **3**:82-100.

Kelley, D.S., Baross, J.A., and Delaney, J.R. (2002) Volcanoes, fluids, and life at mid-ocean ridge spreading centers. *Annu. Rev. Earth Planet Sci.* **30**:385-491.

Kornberg, A., Rao, N.N., and Ault-Riche, D. (1999) Inorganic polyphosphate: a molecule of many functions. *Annu Rev Biochem* **68**: 89-125.

Kulaev, I., and Kulakovskaya, T. (2000) Polyphosphate and Phosphate Pump. Ann. Rev. Microbiol. **54**:709-734.

Kulaev, I., Vagabov, V., and Kulakovskaya, T. (1999) New aspects of inorganic polyphosphate metabolism and function. *J Biosci Bioeng* **88**: 111-129.

Lai, D., Springstead, J.R., and Monbouquette, H.G. (2008) Effect of growth temperatures on tetraether lipid biochemistry in archaeoglobus fulgidus. *Extremophiles* **12**(2):271-278.

Rao, N.N., Gomez-Garcia, M.R., and Kornberg, A. (2009) Inorganic polyphosphate: essential for growth and survival. *Annu Rev Biochem* **78**: 605-647.

Remonsellez, F., Orell, A., and Jerez, C.A. (2006) Copper tolerance of the thermoacidophilic archaeon *Sulfolobus metallicus*: possible role of polyphosphate metabolism. *Microbiology* **152**: 59-66.

Rohlin, J.D. Trent, L., K. Salmon, U Kim, R.P. Gunsalus, and J.C. Liao. 2005. Heat shock response in *Archaeoglobus fulgidus.* J. Bacteriol. 187:6045-6057.

Scherer, P.A., and Bochem, H.-P. (1983) Ultrastructural investigation of 12 *Methanosarcinae* and related species grown on methanol for occurence of polyphosphatelike inclusions. *Can J Microbiol* **29**: 1190-1199.

Stetter, K.O. 1988. "Archaeoglobus fulgidus gen. nov., sp. nov. a new taxon of extremely thermophilic Archaebacteria". *Syst. Appl. Microbiol.* 10:172–173

Toso, D.B., Henstra, A.M., Gunsalus, R.P., and Zhou, Z.H. (2011) Structural, mass, and elemental analyses of storage granules in methanogenicarchaeal cells. *Env. Microbiology* **13**(9): 2587–2599.

Chapter IV

Cellular division in Archaea examined by cryo electron tomography

Daniel B. Toso, Nicole Poweleit, Mohsen Javed, Robert P. Gunsalus, and Z. Hong Zhou

ABSTRACT

Cellular division is one of the most extensively studied biological processes, but it has not yet been fully described in archaeal cells. In this study we characterize the processes of cellular division in *Methanospirillum hungatei* and *Archaeoglobus fulgidus*, two members of the Euryarchaeota phylum of archaea. Samples of both archaeal species were grown to early exponential growth phase and rapidly frozen in vitreous ice to fix the cells in various states of division. These dividing cells were then visualized in three dimensions by cryo electron tomography (cryo ET), allowing characterization of the structural changes that occur step-by-step throughout the process of cell division in each archaeal species. In *M. hungatei*, cellular division proceeds as a semi-uniform constriction at a cleavage plane in the middle of the lengthened cell followed by subsequent reformation of the septum region that separates each cell. In *A. fulgidus*, cellular division proceeds from a localized, shallow depression to a deep invagination that extends from one side of the cell to the other. In addition, it was established that the filamentous temperature-sensitive protein Z (FtsZ) is integral to cytokinesis in both cells and S-layer formation is a driving force of division in *A. fulgidus*.

INTRODUCTION

Cellular division is a process that cells from every organism of life must undergo during their life cycle and it is integral for all organisms to proliferate. The process involves a series of steps generally following the pattern of cellular growth, chromosome replication, segregation of the duplicate genomes, and finally cytokinesis, during which the cell physically divides into two daughter cells, each containing a copy of the genome.

The main goal of cell division is to create duplicate cells with the same genetic material contained in each. Throughout the process, there are a vast amount of cellular processes devoted to making sure each step is carried out properly. The cells must first prepare to divide by growing in size and copying the chromosomes that make up the genetic material of the cell. This process is usually divided into three stages: G1 phase, during which the cell grows in preparation for chromosome replication, S phase, during which the DNA is replicated, and lastly G2, during which the cell grows further in preparation for genome segregation. Once the DNA has been copied it must be properly segregated to each daughter cell. In eukaryotes, this complicated process is called mitosis, while in prokaryotes it is called binary fission. Finally, after the two copies of genetic material have been properly segregated, the cell can proceed to separate into two daughter cells by undergoing the process of cytokinesis.

The process of cytokinesis in eukaryotic cells is carried out via the constriction of a membrane-anchored actomyosin ring composed of actin cytoskeletal filaments and myosin II motor proteins, which is driven, in part, by filament depolymerization (Pinto et al., 2012). In the majority of prokaryotic cells, which includes most bacteria and the Euryarchaeota phylum of archaea, cytokinesis is regulated through the formation of a membrane-anchored Z-ring composed of FtsZ, a tubulin homolog, and associated proteins such as FtsA and ZipA (Lutkenhaus, 1993). Recently, a third mechanism has been described in the Crenarchaeota and Thaumarchaeota phyla of archaea involving Cdv-mediated formation of a contractile ring

apparatus, which is homologous to the ESCRT-III machinery in eukaryotic vesicle formation and final membrane scission during cytokinesis (Samson et al., 2011).

In this study we employ cryo-electron tomography (cryo ET) to visualize and characterize in three dimensions the process of cell division in two members of the Euryarchaeota phylum of archaea, *Methanospirillum hungatei* and *Archaeoglobus fulgidus*. In order to do this we cultured cells until they were undergoing exponential growth phase and then rapidly froze them in vitreous ice to capture cells at various stages of division. We show that each cells undergoes a series of distinct structural changes during the division process, especially in *M. hungatei*, which has an extensive amount of external structures to reproduce for each cell. Interestingly, while both cells express FtsZ proteins and are expected to use the cytoskeletal filaments to mediate cytokinesis, the process is carried out in a very different manner for each: in *M. hungatei* it is a mostly uniform pinching of the membrane, while in *A. fulgidus* it involves an asymmetric invagination that traverses the cell. The differences likely occur due to the physical constraints of *M. hungatei* and its tubular, envelope-bound structure, differences in specific localization of FtsZ filaments, and S-layer formation stabilizing and driving the invagination in *A. fulgidus*.

RESULTS

Because of the limitations of the cryo ET technique, mainly the poor contrast, which is exacerbated in thick samples such as whole cells, it is difficult to resolve certain intracellular features such as nucleic acids and non-filamentous or non-repeating protein structures (Milne et al., 2009). Therefore, we have focused on the ultrastructural changes that occur, mainly in the later stages of cell division, which encompasses cytokinesis and, in *M. hungatei*, the formation of the septum and associated structures. We are able to compare and contrast the process of cytokinesis among the two distinct *Euryarchaeota* species and establish an understanding of how each organism carries out the crucial task of dividing from one cell into two daughter cells.

Cell division in Methanospirillum hungatei

The unique ultrastructure of *M. hungatei* cells imaged by cryo EM was first described previously (Toso et al., 2011). The features that are relevant to cell division are mainly the structures present at the ends of these extended cells that grow from 5 to 10 µm in length. These structures include the multi-layered outer assembly composed of the cell membrane, proteinaceous S-layer, and external, enveloping sheath, as well as the multi-layered plug at the end of each cell and the septum region formed between adjacent cells (Fig. 4-1). It was first observed, during the examination of the dense granules later identified as polyphosphate bodies (PPBs), that the cells characteristically grow to approximately double their length before dividing by binary fission at the center (Toso et al., 2011). Consequently, a single continuous sheath envelope can contain multiple cells, with septum regions between adjacent cells, after several rounds of growth and division have occurred. These septum regions must be reformed each time a cell divides and effectively adds additional steps to the process of cell division beyond cytokinesis. Through the use of cryo ET of many cells at different stages of division, we were able to examine these processes, to some degree, step-by-step in three dimensions.

In order to analyze cells undergoing division, *M. hungatei* cells were grown up to early exponential growth phase and harvested over a three day period at 24 hour intervals, as described in Methods. The cells were checked for concentration and sample quality by negatively staining before being rapidly frozen in vitreous ice, also as described in Methods. Examining cells harvested on the first day showed many more cells actively growing and dividing compared to the cells harvested on the second and third days. Samples were evaluated for good cell concentration and the presence of many dividing cells, as shown in low magnification stain images as lengthened cells in the process of or recently completed division. In the second and third day, especially, cell samples showed extended filaments containing multiple cells that had already completed cell division. Consequently, most of the tomograms of cells in the midst of cell division were collected from frozen grids of the Day 1 samples, while many cells in the later stages of septum formation were found on grids from the Day 2 samples.

During the first phase of observable division, the cellular membrane begins to pinch inward, signifying the start of cytokinesis. In *M. hungatei* cells, this process appears as a somewhat uniform, circular contraction of the membrane from the sheath. As shown in a series of cellular tomograms at different states of cytokinesis, this process proceeds until the cell is contracted to a small radius, whereupon scission would occur (Fig. 4-2). Significantly, it was observed that the S-layer appears to be absent at the region of cytokinesis. This is confirmed when examining the cross-section of the 3D tomograms of these cells (Fig. 4-3). It seems that the divisome machinery that leads the cell to constrict during cytokinesis also excludes the membrane-anchored S-layer proteins from the region undergoing constriction. It is also observed that the constriction process does not proceed in a completely symmetric, circular pattern (Fig. 4-3A). While it seems to proceed in a somewhat uniform manner, constricting from the entire circumference of the cell, it is shown to be asymmetric. This indicates that the process does not involve the constriction of a large, uniform, membrane-anchored ring structure, which would most likely be apparent in the tomograms as well, but may be the result of discrete

constriction events that additively lead to the semi-uniform invagination of the cell membrane. Furthermore, membrane associated cytoskeletal filaments are seen in some of the tomograms of dividing cells in the region of constriction, and may be involved in the cytokinesis process (Fig. 4-3B, insets). These filaments may be composed of FtsZ, which are integral to cytokinesis in many prokaryotes and are known to be expressed in *M. hungatei* cells (Mhun_0660).

In the next phase of division, the multi-layered plugs begin to form in the space between the recently divided cells. This is the beginning of the process of septum formation. Plug formation appears to be an asymmetric process, with one plug being formed first before the other plug is formed on the opposite side of the septum. The plugs often appear to extend at an angle, relative to the sheath, rather than perpendicular as seen in fully formed septa. This may be due to a specific formation process whereby both plugs originate from the same region on one side of the septum and then tend to angle apart as they grow outward across the septum. This lateral plug growth can be seen in several of the tomograms (Fig. 4-4A). One final thing of note during this process is the appearance of parallel filaments arrayed along the inside of the sheath in the septum region (Fig. 4-4A, indicated by bracket). These filaments are spaced regularly along the surface of the sheath and their appearance coincides with the formation of the plugs.

In the final stages of septum formation, the fully formed plugs first extend across the septum at an angle, which is mostly likely due to their formation process as described above (Fig. 4-4B). Eventually, the plugs settle in a mostly perpendicular orientation to the sheath with a slight curvature. The plugs seem to have a somewhat fixed position relative to one another and settle with a slightly variable spacing, which may be related to the aforementioned filaments which always line the sheath surface in the septum region located between the two plugs. The position of the septum seems to be fixed independently of the cells, as several tomograms show fixed septa including uniformly spaced plugs with cells in different states of retraction from the septum region (Fig. 4-4C). Finally, the cells adopt a distinctive conformation with the septum

fully formed, plugs spaced apart somewhat uniformly, the filaments lining the sheath, and the cells abutting against the plugs. One unique feature that is not seen in every tomogram collected of the septum regions is the formation of arrays of filaments within the septum region. It is unknown what their function is or if they are somehow involved in the formation of the outer layer structures (Fig. 4-4D).

Cellular division in Archaeoglobus fulgidus

The *A. fulgidus* cell has a somewhat different ultrastructure compared to *M. hungatei* and is briefly described in Chapter III. First of all, it is not bound by a rigid, tubular sheath layer, but is free to form amorphous, rounded cells. It does have a distinctive S-layer external to the plasma membrane, similar to *M. hungatei*, which is composed of a paracrystalline lattice of membrane-anchored proteins (Fig. 4-5A). It is noted in cryo EM images of whole cells that while the cells generally have a rounded appearance, often some of the edges of the cell can appear to be angular or straightened, which may be due to rigidity in the repeating structure of the membrane-anchored S-layer imposing some linearity on the surface of the cell (Fig. 4-5B). This structural rigidity may have some influence on the process of cell division, which we examined in three-dimensions through the use of cryo ET tilt series acquisition of whole cells in exponential growth phase.

We first noted cellular division when examining negatively stained cell culture preparations and observed cells that appeared stuck together, almost as if they were budding from each other (Fig. 4-5C). It was suspected that they had divided and formed these conformations, however, due to the drying and staining of the cells it was difficult to determine how this came about. When observing these cells by cryo EM, it was found that they were not actually connected, but merely in very close proximity, abutting against one another along a large area of S-layer bound membrane (Fig. 4-5D). Again, this was suspected to be the conformation adopted after the cells had just divided.

The initial imaging of whole cells proved difficult due to the thickness of the cells that leads to very thick ice, often approaching 1 µm in thickness. This causes problems with ice crystallization as well as very poor contrast, especially in the thick portions of the cell, resulting in poor quality images and poor quality of the subsequent reconstructions. Capturing cells in the midst of division also proved difficult. It was initially not known how to resolve these issues, but luckily subsequent studies examining cells grown with different nutrient conditions provided a suitable sample for cryo ET study of cellular division.

While examining *A. fulgidus* cells grown with varying phosphate concentrations, it was observed that the cells grown in media containing 2 mM phosphate, half of the concentration used in normal growth media, were smaller in size compared to cells grown under normal conditions (Fig. 4-6A). This smaller size, coupled with the ability of these pliable cells to flatten when the solution was blotted to a thin film prior to freezing, lead to thinner ice, around 300-350 nm thick, and higher quality images of the whole cells frozen in vitreous ice. It was also observed that many of the cells, harvested early in their exponential growth phase, seemed to be in the midst of dividing, with what looked like cleavage furrows present (Fig. 4-6B-D). Unexpectedly, the cleavage furrows appeared to propagate in a unidirectional manner across the cells from one side to the other. Subsequently, cryo ET tilt series were collected of several cells in order to study this unique division process in three dimensions.

A series of three-dimensional reconstructions of the dividing *A. fulgidus* cells reveal that the process of cytokinesis proceeds from a depression to an invagination, spanning the width of the cell, which extends across the cell in order to split it into two approximately equal-sized daughter cells (Fig. 4-7). Initially, at the beginning of cytokinesis there is often a region of the membrane that becomes depressed inward (Fig. 4-7A). This is most likely due to the membrane in this region being constricted locally by cytokinetic forces. This constriction appears to occur completely asymmetrically, only one side of the membrane pinches inward during division as opposed to a uniform pinching of the membrane in a circular band at the middle of the cell.

Thus, it appears that constriction occurs in a localized region. In fact, when examining the regions of constriction in the reconstructions, short membrane-associated filaments can be observed (Fig. 4-8). These are likely filaments comprised of the protein FtsZ, as it is expected to be involved in cytokinesis and is expressed in *A. fulgidus* cells (AF0535).

After the membrane is initially depressed, cell division proceeds with the formation of a more localized invagination (Fig. 4-7B). This invagination eventually spans the entire width of the cell and appears like a furrow, as can be seen by cross-sectional views (Fig. 4-7C-E). This furrow then pushes deeper into the cell and eventually extends to the opposite membrane where scission occurs to separate the cell into two daughter cells of roughly equivalent size. Of particular significance is the observation that the S-layer remains present and intact throughout this invagination process. In fact, even at the leading edge of the invagination, the S-layer coats the entire surface of the membrane and can be seen looping back on itself (Fig. 4-8A, inset). It is suspected that S-layer formation stabilizes the invagination of the membrane and, due to its rigidity, may actually be a driving force to push the furrow across the cell.

DISCUSSION

FtsZ's role in cytokinesis of archaeal cells

Both *M. hungatei* and *A. fulgidus*, belonging to the phylum Euryarchaeota, are known to express the FtsZ protein (Mhun_0660 & AF0535, respectively) responsible for cytokinesis in many other prokaryotes including both bacteria and archaea (Lutkenhaus, 1993; Lutkenhaus et al., 2012; Wang et al., 1996). FtsZ is tethered to the membrane through interaction with FtsA and ZipA proteins in *E. coli* (Pischoff and Lutkenhaus, 2002). Futhermore, this interaction is required to recruit the remaining proteins present in the Z ring, whose formation allows division to proceed (Hale and de Boer, 2002).

Previously, cryo ET examination of FtsZ filaments and Z ring formation in the bacteria *Caulobacter crescentus*, whose cells form thin, extended regions of cytoplasm during division that are ideal for cryo ET, sparsely arranged filaments were found perpendicular to the long axis of the cell arranged adjacent to the membrane and the prevalence of these filaments was altered corresponding to changes in FtsZ expression level (Li et al., 2007). The conclusion was reached that FtsZ filaments do not actually form solid ring structures, as seen previously by fluorescence studies (Margolin, 1998; Sun and Margolin, 1998), but form short filaments that act locally by changing conformation through GTP hydrolysis, which had been shown to alter the filaments from a straightened to a curved conformation (Lu et al., 2000). The conformational change of the membrane-anchored filaments would provide the driving force to pinch the membrane and, additively, many such events would lead to membrane constriction. It is suggested that the highly dynamic nature of the filaments, which have been shown to have a halftime of 8-10 seconds (Anderson et al., 2004) and would be polymerizing and depolymerizing continually, may be responsible for the ring structures shown previously, as all of the FtsZ, both free and filamentous, would contribute to fluorescence (Li et al., 2007). However, the actual substructure of the Z ring is a matter of dispute in the field and it has been suggested that cryo ET simply fails to capture many of the filaments present, due to its limitations, when considering

the evidence for ring structures (Lutkenhaus et al., 2012). In our cryo ET reconstructions of whole archaea cells in the midst of division there are several different sources of evidence for the presence of FtsZ filament involvement in cell division events.

First of all, we found evidence for the presence of filaments composed of FtsZ in the regions of constriction in dividing cells of both *M. hungatei* (Fig. 4-3B) and *A. fulgidus* (Fig. 4-8B,C). These filaments were not present in large concentrations or found to form any obvious superstructures such as rings, but were observed as scattered membrane-associated short filaments in the regions of cell constriction. The filaments were oriented perpendicular to the long axis of the cell in *M. hungatei* and were located lying along the membrane of the cell (Fig. 4-3B). *A. fulgidus* cells do not have a defined long axis, as they are rounded, but there is a defined cleavage plane and filaments were discovered adjacent to the membrane parallel to the cleavage plane (Fig. 4-8B,C).

In addition, filaments were observed adopting both straightened (Fig. 4-3B, upper cross-section) and curved (Fig. 4-3B, lower cross-section) conformations in *M. hungatei* cells. This gives evidence for a possible GTPase mediated conformational change in the filaments, as the straight filaments could be composed of FtsZ bound to GTP, while the curved filaments would be composed of FtsZ bound to GDP, after hydrolysis of GTP to GDP. When the membrane anchored straight filaments change conformation to a more curved structure, this causes a pinching in the membrane. This process can be repeated, as the GDP bound FtsZ filaments depolymerize into monomers before nucleotide exchange and straight filament polymerization. These pinching events caused by many individual short filaments can additively cause membrane constriction (Li et al., 2007).

Furthermore, the filaments observed in the *A. fulgidus* cells seem to have a variable length, with filaments observed adjacent to the larger initial depression region adopting longer configurations (Fig. 4-8C) while filaments adjacent to the smaller region of the cleavage furrow adopt shorter configurations (Fig. 4-8B). This dynamic property supports the theory that

individual filaments act to provide the force for contraction, as opposed to larger ring structures, as they can adapt their length to correspond with the area of constriction. This would allow the filaments to shorten as the area of constriction shrinks, even to length scales below tens of nanometers, as seen in *M. hungatei* as the gradual reduction in the circumference of pinching and in *A. fulgidus* as the development of the narrow cleavage furrow.

Finally, the amount of asymmetry observed during cell constriction activity supports a model of localized cytokinesis activity, such as may be caused by FtsZ filaments. In *M. hungatei*, it was observed that the constriction of the cells, while it tends to proceed in a circular pattern, originates at specific locations around the circumference of the cell (Fig. 4-3A). It is also seen that the circular constriction process is by no means uniform as is seen in the asymmetric pinching of many cells undergoing cytoskinesis (Fig. 4-2). In *A. fulgidus*, the process of cell cytokinesis, as described previously, is observed to be completely asymmetric, proceeding from one side of the cell to the other (Figs. 4-6 & 7). This almost precludes the possibility of ring structures being involved in the constriction process, rather than more localized and dynamic forces.

Almost all of the evidence observed in our cryo ET reconstructions of dividing cells supports the theory of dynamic FtsZ filament activity during cytokinesis. First of all, the observations of short membrane-associated filaments present in the regions of constriction in both *M. hungatei* and *A. fulgidus*. Secondly, the presence of both straightened and curved filaments among those observed, indicating conformational change by GTPase activity. Thirdly, the dynamic length properties of the filaments, which allow them to adapt to shorter length scales corresponding to the cytokinesis structures observed, including narrow constricting cells and cleavage furrows. Finally, the asymmetric cytokinesis processes we observed would favor localized, dynamic constriction processes. This leads to the conclusion that dynamic FtsZ filaments can provide the driving force of cell constriction via conformational change during

cytokinesis in the archaea cells we examined in this study and they may provide a more universal mechanism for cytokinetic activity among prokaryotes.

The role of the S-layer in cytokinesis of archaeal cells

External envelope layer formation has been shown to be integral to cellular division in bacterial cells, such as *E. coli*, as it was shown that divisome machinery, including the Z ring, stimulate cell wall peptidoglycan, also known as murein, synthesis in the region of cell invagination during cell division (Nanninga, 1991). This murein production helps to stabilize the constricting membrane and promotes cytokinesis. Additionally, it has previously been shown that S-layer formation is involved in cell division in *Methanocorpusculum sinese* cells and may possibly be generalized to be significant in any cells with a single membrane-anchored para-crystalline cell envelope layer (Pum et al., 1991). The strain produced by adding additional S-layer subunits to the fully-coated surface of the cell causes inward growth of the S-layer, which leads to the formation of shallow invaginations that can extend deeper as more subunits are added to the envelope layer.

This phenomenon of shallow depressions leading to deep invaginations is almost exactly what we observed by cryo ET in *A. fulgidus* cells undergoing division (Fig. 4-6 & 7). Particularly, it was observed that S-layer proteins can be seen lining the entire area of the invaginations, even up to the leading edge as it extends deeper into the cell (Fig. 4-8A, inset). This leads us to believe that S-layer formation in *A. fulgidus* may, in fact, significantly contribute to the process of cell cytokinesis, by providing the driving force for cleavage furrow extension across the width of the cell.

In *M. hungatei*, the S-layer, conversely, does not seem to be involved directly in cell division at all, as it was seen in the cryo ET reconstructions that the S-layer is excluded from the regions undergoing cytokinesis (Fig. 4-3). *M. hungatei* cell morphology is not dependant on the shape of the S-layer as it is bounded by a rigid external sheath layer, therefore it seemingly

does not share the same constraints related to S-layer rigidity and crystalline lattice network strain as single-enveloped archaea such as *A. fulgidus*. It is not known what mechanism excludes the membrane-anchored proteins of the S-layer from the constricting region or why, exactly, this is preferred in *M. hungatei*. The cell's divisome machinery that regulates cell division may be responsible, as the Z ring and other proteins involved are active in the cleavage zone. This machinery is most likely involved in regulating the post-divisional septum formation processes, as well. These processes would require the exportation of large amounts of proteins and other components involved in plug and septum formation. It is possible that the presence of the S-layer coating the membranes would interfere with exportation or other septum formation related processes after cell division, therefore the cell acts to exclude the S-layer from the membrane prior to division.

Compare and contrast division in M. hungatei and A. fulgidus

We have noted that the processes of cell division in *M. hungatei* and *A. fulgidus* proceed in somewhat different manners. *M. hungatei* cells first grow to twice their normal length, divide by constricting semi-uniformly and pinching off in the center, and finally reform their extensive external septum structures. *A. fulgidus* cells first grow larger, form initial depressions, and eventually extend cleavage furrows across the cell width. Both of these processes are suspected to involve FtsZ filaments, which produce constriction force through conformational change. However, as *A. fulgidus* utilizes S-layer formation to drive the cleavage furrow growth, it may not use FtsZ filament driven constriction to the same degree as *M. hungatei*, which does not use S-layer formation to stabilize membrane pinching at all.

Finally, each cell may regulate cellular division processes in a different manner. In *A. fulgidus* cells*, we* observed that FtsZ filaments may be involved in the formation of the initial membrane depressions, as membrane-associated filaments were observed in the region of depressions in the cryo ET reconstructions (Fig. 4-8C). This formation of initial depressions by

FtsZ filaments may be localized by divisome machinery to direct S-layer invagination, allowing the cell to regulate where the cleavage furrow develops. This is important because proper nucleoid segregation must occur prior to cytokinesis, producing daughter cells with one copy of the genome in each. In *M. hungatei* cells, the localization of the cleavage plane is not as arbitrary because the cell itself has a fixed geometry and the divisome machinery can be directed to the center of the extended, tubular cell before initiating cell division and regulating cleavage perpendicular to the long-axis of the cell.

EXPERIMENTAL PROCEDURES

Cell Culture

Methanosprillum hungatei strain JF1 (DSM 864) was cultivated on a CO_2/bicarbonate buffered mineral medium supplemented with trace metals, vitamins, and sodium acetate with a vessel headspace containing a 80%-20% atmosphere of hydrogen and carbon dioxide. The medium contained per 1000 ml: 0.54 g NaCl, 0.12 g $MgSO_4 \cdot 7H_2O$, 5.0 g NH_4Cl, 1.8 g KH_2PO_4, 2.9 g K_2HPO_4, 0.06 g $CaCl_2 \cdot 2H_2O$, 2.72 g Na Acetate $\cdot 3H_2O$, 10 mL of 100x trace metal solution and 1 mL of 1000x vitamin solution. Following sterilization, the medium was supplemented with 10 ml filter-sterilized solution of reducing reagent (2.5% $Na_2S \cdot 9H_2O$, 2.5% Cysteine HCl) and 20 ml of a 1 M $NaHCO_3$ solution. Trace metals and vitamins were as previously described for *M. acetivorans* (Rohlin and Gunsalus, 2010). Following inoculation, anaerobe tubes containing 10 ml of medium were incubated at 37 °C horizontally on a rotary drum shaker (60 RPM, New Brunswick, Inc). Cells were serially transferred at least three times with transfers made at mid-exponential phase to achieve 10 plus cell doublings prior to harvest. Cells were harvested early in exponential growth phase by centrifuging 1 mL of cell supension at low speed (5,000 x g) and resuspending in 100 µl of medium over a three day period, with 24 hours between each harvest.

Archaeoglobus fulgidus (DMS 4304) cells were cultured at 83°C in an anaerobic CO_2/bicarbonate buffered mineral medium supplemented with vitamins and sodium lactate as previously described (Rohlin et al., 2005). The medium consisted of 1L of ultra-pure water, 18g NaCl, 3.4 g $MgSO_4 \cdot 7H_2O$, 2.8 g $MgCl_2$ - $6H_2O$, 0.5 g NH_4Cl, 0.5 g KCl, 0.55 g KH_2PO_4, 0.14 g $CaCl_2 \cdot 2H_2O$, 1 mL of a 1000x H^+ trace mineral solution (50 mM HCl, 1 mM H_3BO_3, 7.5 mM $FeCl_2$, 5 mM $NiCl_2$, 0.5 mM $MnCl_2$, 0.5 mM $ZnCl_2$, 0.5mM $CoCl_2$, 0.5 mM $CuCl_2$, 0.5 mM $CuCl_2$, 0.5 mM $AlCl_2$), 1 mL of a 1000x OH trace mineral solution (10 mM NaOH, 0.1 mM Na_2SeO_3, 0.1 mM Na_2WO_4, 0.1 mM Na_2MoO_4), and 1 mL of 1000x vitamin solution as previously described (Balch et al., 1996). Sodium lactate was added to a final concentration of 20 mM. The medium was flushed with a N_2/CO_2 (80:20) gas mixture to remove oxygen and then dispensed into

N_2/CO_2 flushed glass bottles. The bottles were then sealed with butyl rubber stoppers and crimp aluminum caps. The medium was autoclaved at 121 ℃. Prior to inoculation, the medium was supplemented with a sterile anaerobic stock solution of 2.5% $Na_2S \cdot 9H_2O$/2.5% Cysteine HCl (1% v/v) and 1M $NaHCO_3$ (2% v/v) to reduce the medium and adjust it to pH 7.0. Additional cultures were grown with varying PO_4 concentrations from the 4 mM normally used, including: nil, 1 mM, 2 mM, and 9 mM. All cultures were serially transferred at least three times at mid-exponential phase, retaining the same media conditions. Cells were harvested during exponential growth phase by centrifuging 1 mL of cell suspension at low speed (5,000 x g) and resuspending in 100 µl of media.

Electron microscopy

In order to assess sample concentration and quality, cell samples were first examined by negative staining and cryo electron microscopy (cryo EM). For negative stained TEM, copper grids with carbon-coated Formvar film were first glow-discharged, followed by placement of a small droplet (~4 µl) of cell suspension onto the carbon side of each grid. After one minute at room temperature, the excess of the sample droplet was blotted from the side of the grid and a droplet of 1% uranyl acetate solution was immediately placed on the grid. After one minute, the stain droplet was blotted off and the staining/blotting step was repeated four times to remove any excess sample from the grid. After air drying, the grid was observed in an FEI Tecnai F20 transmission electron microscope operated at an accelerating voltage of 200 kV to assess the concentration of cells on the grid. To adjust concentration, if necessary, cells were centrifuged at low speed (5,000 x g) in a table-top microfuge, and re-suspended in culture medium.

To prepare ice-embedded cells for cryo EM observation, a droplet (4 µl) of cell suspension was placed onto a glow discharged, 200 mesh Quantifoil holey carbon grid with a spacing of 3.5 µm hole/ 1 µm edge. The sample was allowed to settle for 30 seconds before being blotted by filter paper and immediately plunged into liquid nitrogen cooled liquid ethane.

A Gatan 626 cryo sample holder and the above-mentioned Tecnai F20 electron microscope were used to image the cells imbedded in vitreous ice on a 16 megapixel TVIPS CCD camera.

Cryo electron tomography

To prepare ice-embedded cells for cryo ET, 100 µl of cell solutions with optimized concentration were mixed with 4 µl of 10 nm protein-A gold solution and mixed thoroughly before freezing on Quantifoil grids as described above. For cryo ET tilt series collection, we used an FEI Titan Krios instrument operated at an accelerating voltage of 300kV and equipped with a Gatan image filter (GIF) 2002 camera. During tilt series acquisition, we chose cells whose long axes were roughly parallel to the tilt axis of the microscope. The cells were imaged at varying magnifications in the range of 30,000-50,000x. An underfocus value of 5 µm was targeted for all images in the tilt series. All tomography tilt series were recorded using the FEI Batch Tomography software with a tilt range from -70^{o} to $+70^{o}$ and 2^{o} increment or -65^{o} to $+65^{o}$ and 1^{o} increment. The total electron dosage on the samples was 200 $e^{-}/Å^{2}$ for each tilt series.

CryoET data analysis and 3D visualization

The tomography tilt series were processed with a suite of programs to generate 3D reconstructions. Alignment of the tilt series was performed using the etomo tomography processing software from the Imod package (Kremer et al., 1996). The steps included X-ray removal, rough alignment by cross-correlation, fine alignment by fiducial gold tracking, and tilt-axis adjustment. The aligned tilt series were then used to make 3D reconstructions with weighted back-projection reconstruction in etomo or GPU-based SIRT (Simultaneous Iterative Reconstruction Technique) reconstruction implemented in Inspect3D. The 3D reconstructions were saved as stacks of X-Y plane images that are single pixel slices along the Z-plane. Slices from the reconstructions were displayed using slicer within 3dmod from the Imod package. Further processing, such as binning and filtering, was performed using Imod clip functions in

order to improve contrast and reduce noise in the reconstructions. Amira (Visage Imaging GmbH, http://www.amira.com/) was used to create volume renderings of the 3D density maps of the cells.

FIGURES

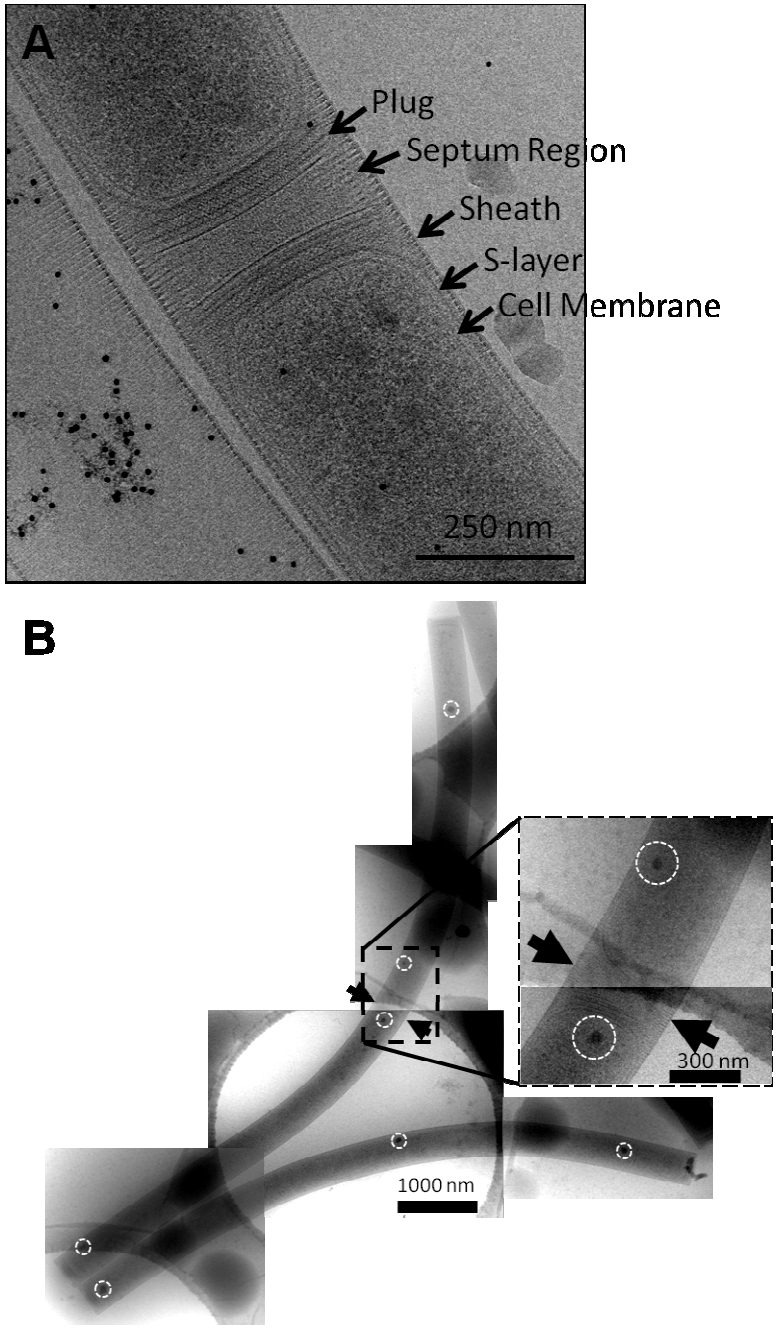

Fig. 4-1: *M. hungatei* cell ultrastructure (A) CryoEM image of a septum region, with labeled plug, septum, sheath, S-layer, and cell membrane. (B) Cell composite showing recently divided cells sharing a single sheath. The septum region is labeled with arrows. (Toso et al., 2011)

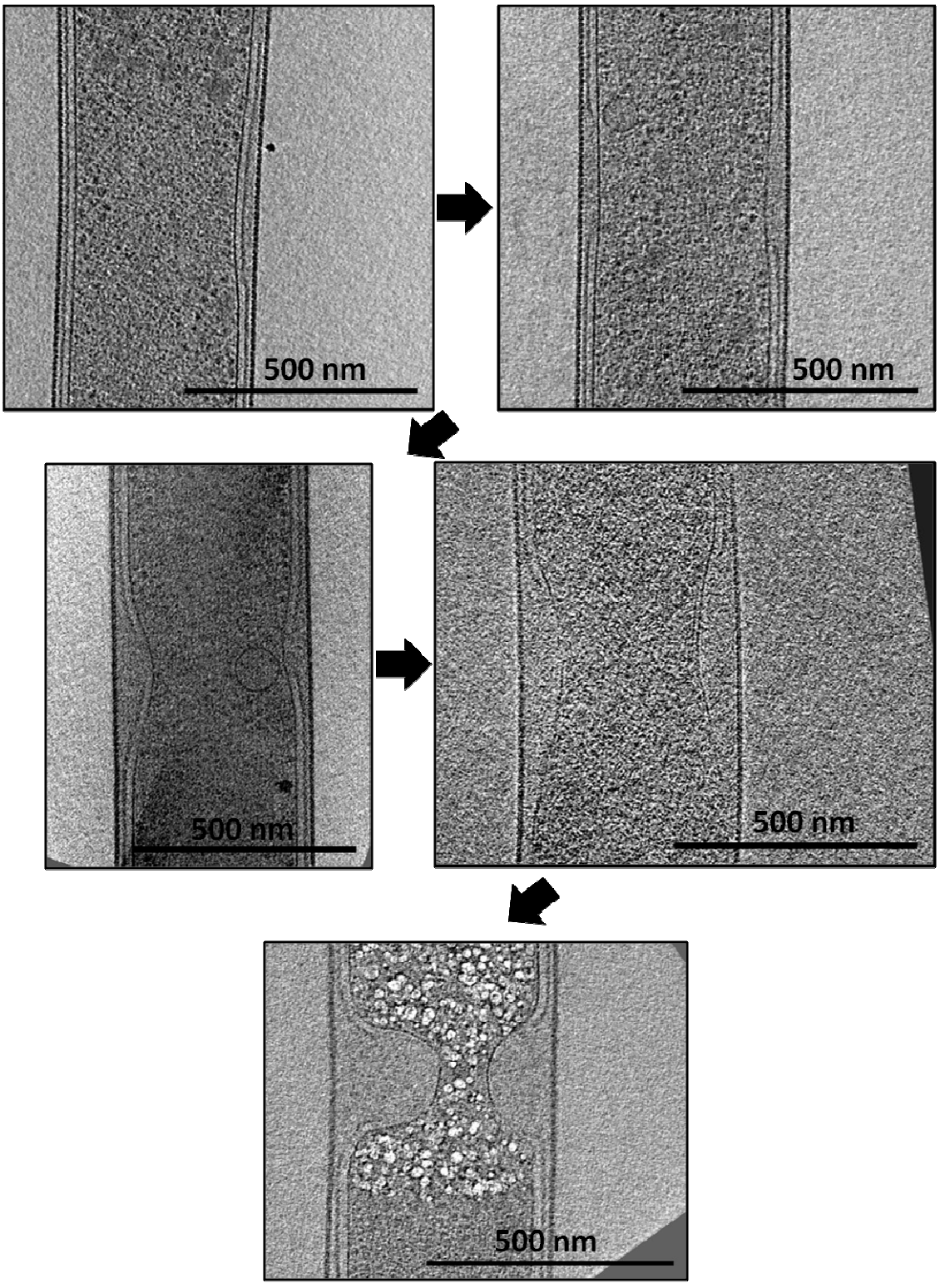

Fig. 4-2: *M. hungatei* cytokinesis shown in a series of central slices from cryo ET reconstructions of several different cells frozen in the midst of division.

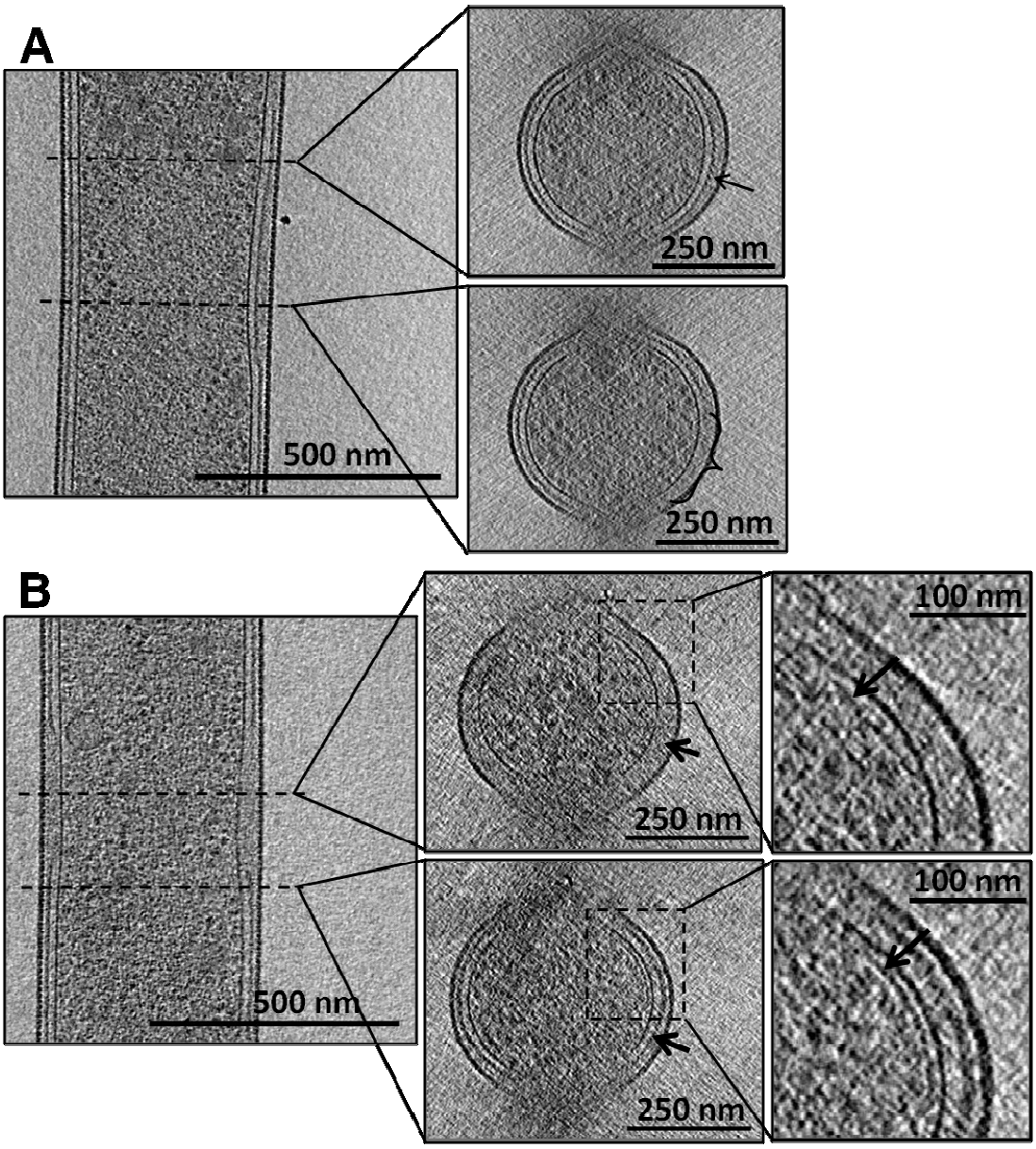

Fig. 4-3: Central slices and cross-sectional views through cryo ET reconstructions of two different *M. hungatei* cells undergoing cytokinesis. (A) Membrane pinching initially begins only on one side of the cell and S-layer exclusion can be seen in the cross-section of the constricting region, confined to one quadrant (indicated by a bracket). (B) Membrane pinching extends around the entire circumference of the cell and S-layer exclusion is shown to be uniform in a cross-section of this region (indicated by an arrow). Insets show higher magnification views of membrane-associated cytoskeletal filaments believed to be FtsZ.

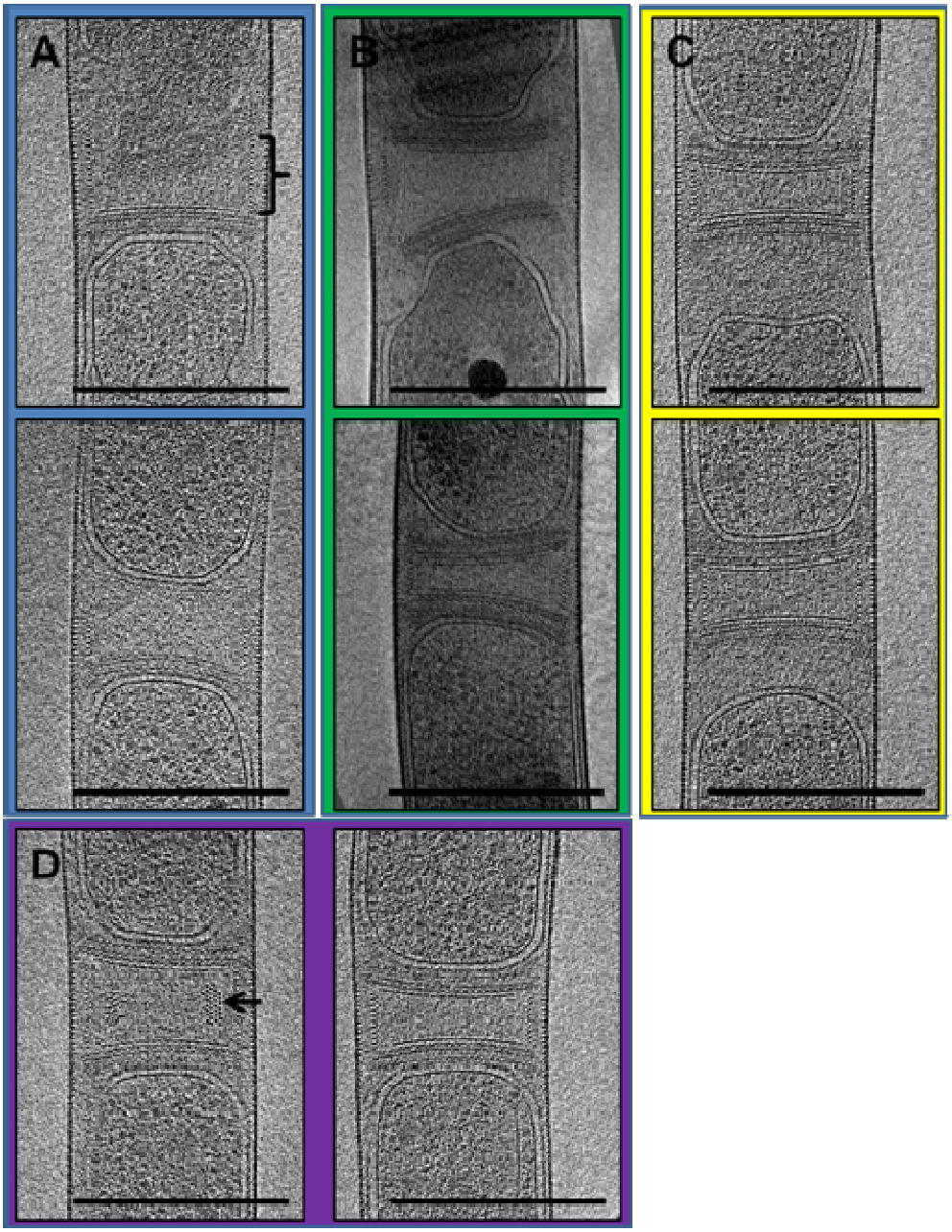

Fig. 4-4: *M. hungatei* septum formation proceeds in several stages. Slices from cryo ET reconstructions from representative cells are shown. (A) Plugs are forming in the septum region. Filaments arranged along the inner wall of the sheath are indicated by a bracket. (B) Plugs are formed, but not settled in their final position. (C) The plugs have settled into the final septum configuration, independent from the cells. (D) The characteristic final septum configuration. A filament array within the septum region is indicated by an arrow. All scale bars are 500 nm.

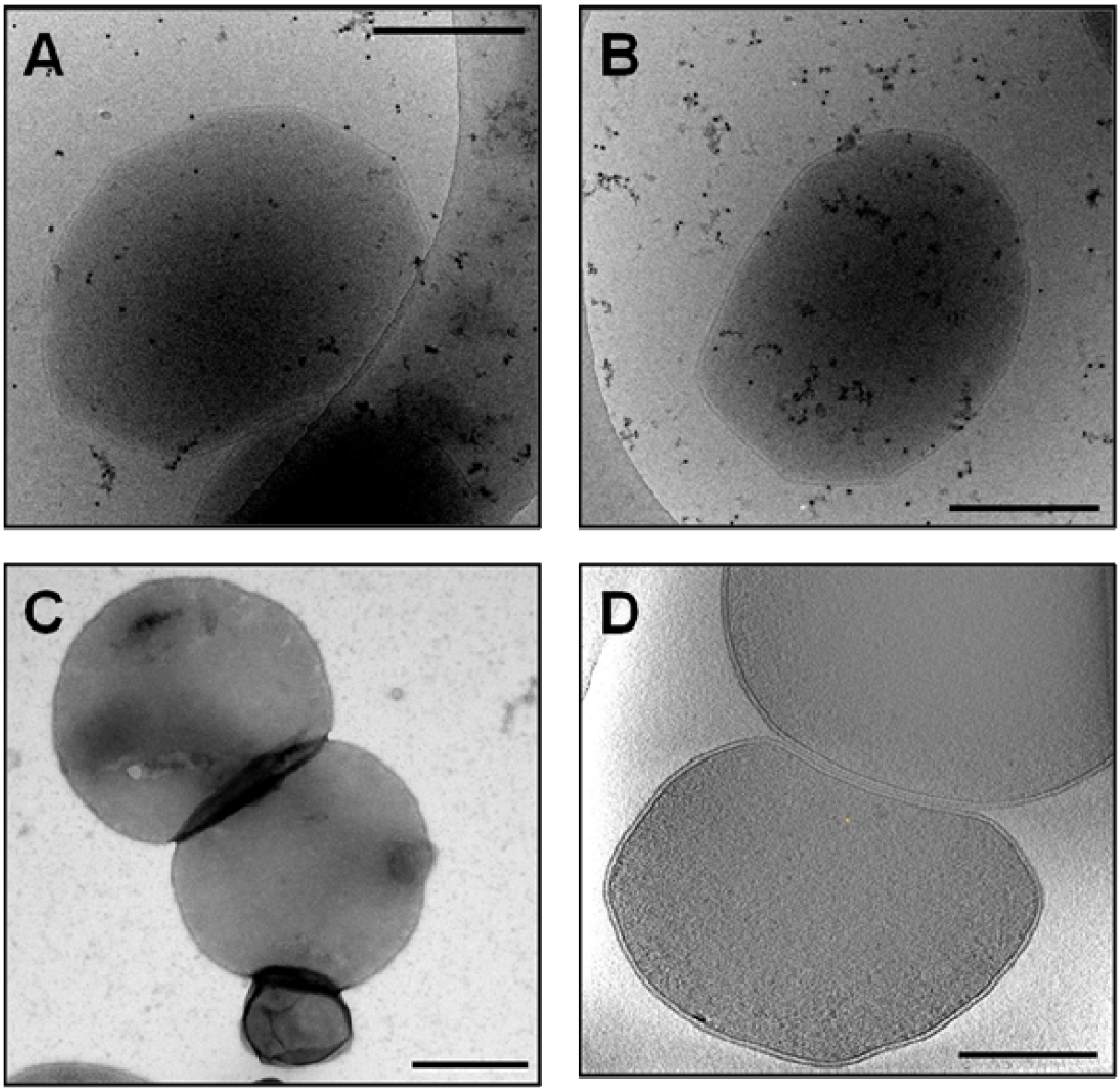

Fig. 4-5: (A,B) CryoEM images of whole *A. fulgidus* cells frozen in vitreous ice. (A) The cell has a more rounded appearance. (B) The cell has angular and straightened edges. (C) Negatively stained cells which have recently divided, showing a budded appearance. (D) A central slice through a cryo ET reconstruction of recently divided cells, showing their shared boundary. Scale bars are 500 nm.

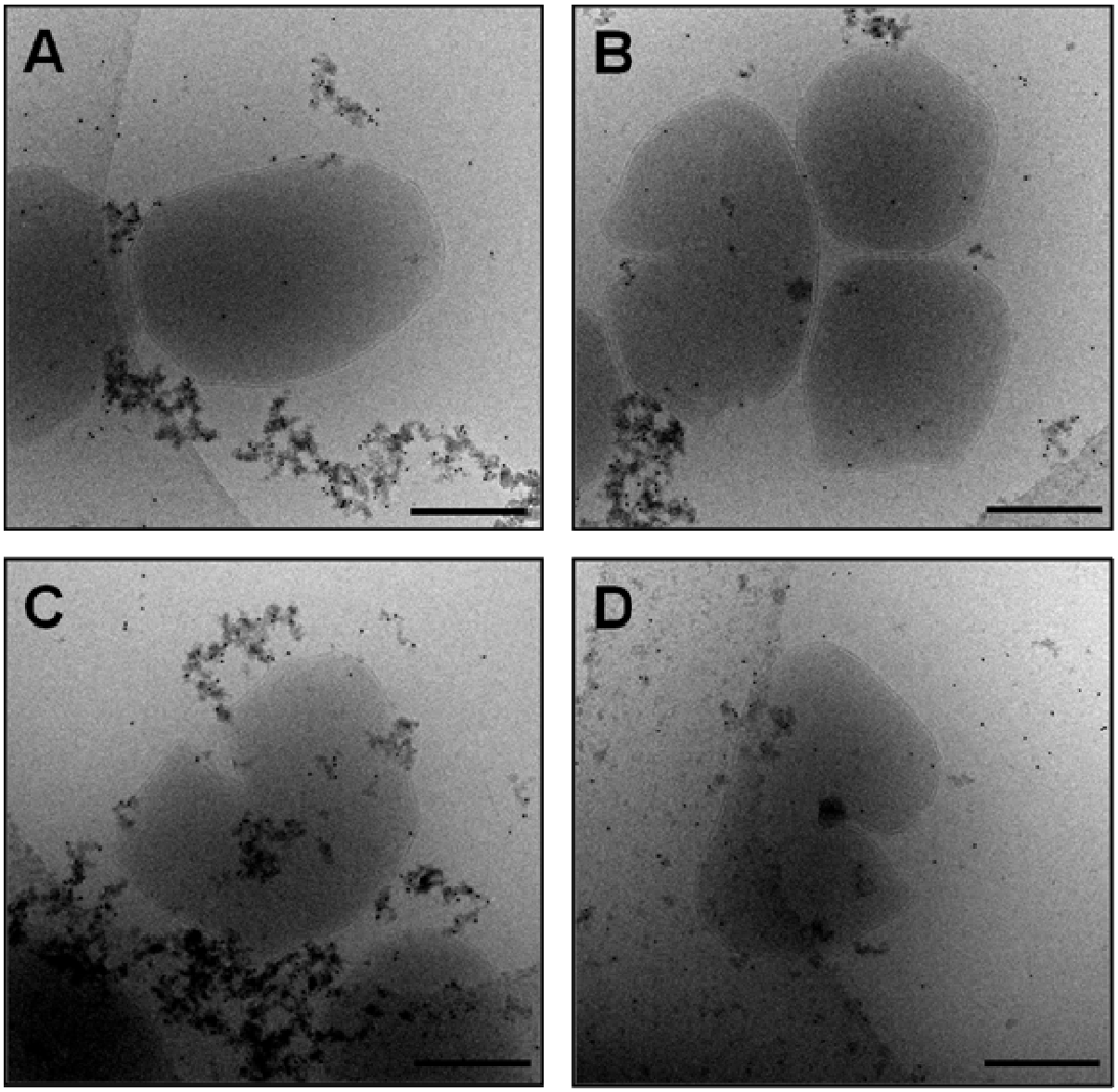

Fig. 4-6: Cryo EM images of *A. fulgidus* cells grown in media with 2 mM phosphate. (A) The cells are reduced in size compared to cells grown in normal phosphate conditions (4 mM). (B-D) Many cells appear to be in the midst of division. Scale bars are 500 nm.

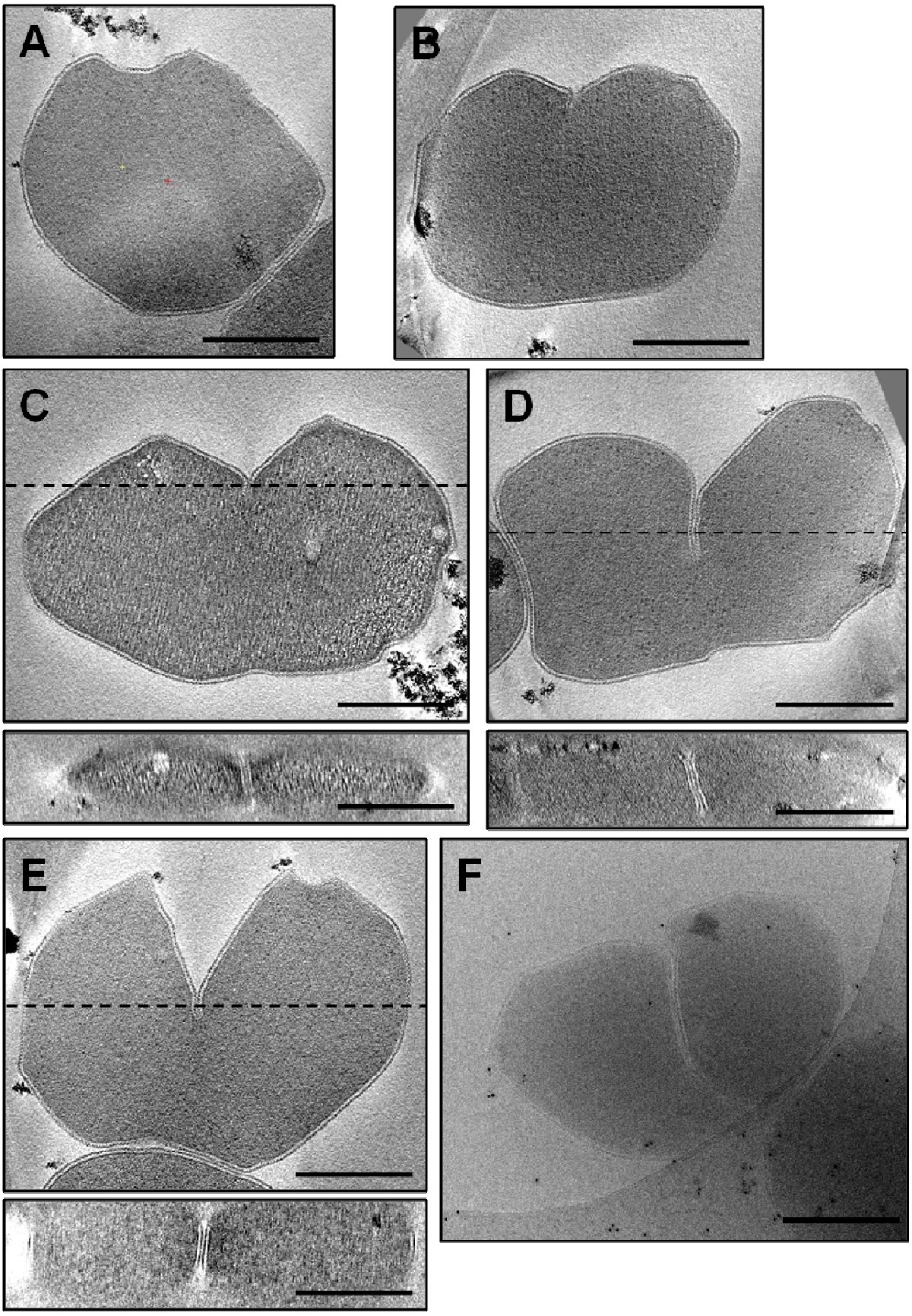
A
B
C
D
E
F

Fig. 4-7: The process of *A. fulgidus* cytokinesis shown as a series of central slices from cryo ET reconstuctions of cells undergoing division. (A-E) (A) Initial depression of the membrane. (B) Localized invagination originates in the depression. (C-E) The cleavage furrow extends across the cell. The dashed lines represent the planes shown in the lower cross-sectional views, which demonstrate that the cleavage furrows span the entire depth of the cell. (F) CryoEM image of a cell just before scission, the furrow has extended across the entire width of the cell. All scale bars are 500 nm.

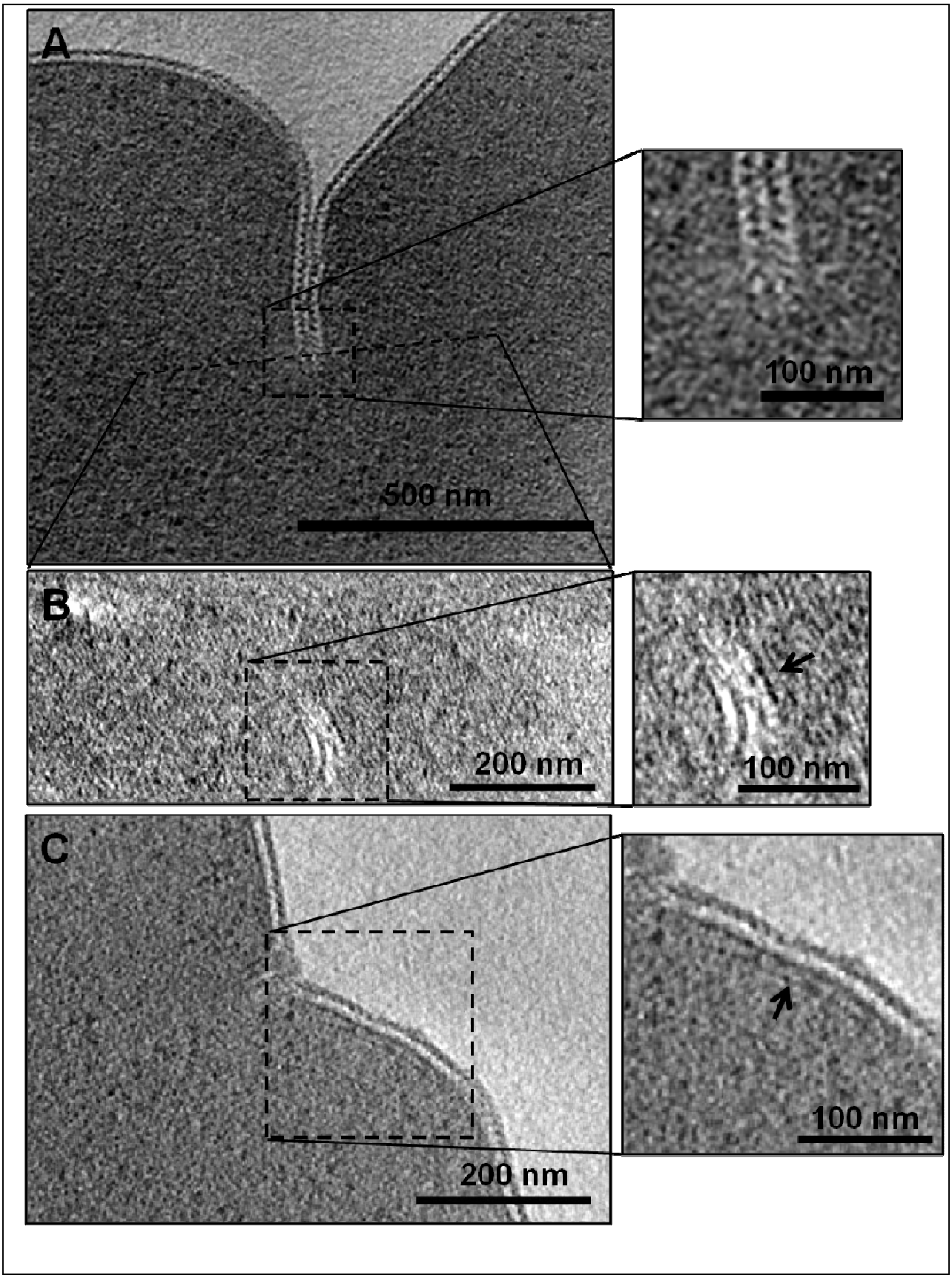
A
500 nm
100 nm
B
200 nm
100 nm
C
200 nm
100 nm

Fig. 4-8: Higher magnification view of a cryo ET reconstruction slice of (A) a cleavage furrow region, (B) cross-section across the dotted line in (A), and (C) a cellular depression region. (A, inset) A higher magnification view of the leading edge of the furrow showing complete S-layer infiltration. (B, inset) A higher magnification view of the region near the cleavage furrow. An arrow indicates a membrane-associated filament. (C, inset) A higher magnification view of the membrane near the depression region. The arrow indicates a membrane-associated filament.

REFERENCES

Anderson, D.E., Gueiros-Filho, F.J., and Erickson, H.P. (2004) Assembly dynamics of FtsZ rings in Bacillus subtilis and Escherichia coli and effects of FtsZ-regulation proteins. *J Bacteriol* **186**(17): 5775-5781.

Balch, W. E., G. E. Fox, L. J. Magrum, C. R. Woese, and R. S. Wolfe. 1996. Methanogens: reevaluation of a unique biological group. *Microbiol. Rev.* **43**:260–296.

Hale, C.A., de Boer, P.A. ZipA is required for recruitment of FtsK, FtsQ, FtsL, and FtsN to the septal ring in Escherichia coli. *J Bacteriol* **184**(9): 2552-2556.

Kremer, J.R., Mastronarde, D.N., and McIntosh, J.R. (1996) Computer visualization of three-dimensional image data using IMOD. *J Struct Biol* **116**: 71-76.

Li, Z., Trimble, M.J., Brun, Y.V., and Jensen, G.J. (2007) The structure of FtsZ filaments *in vivo* suggests a force-generating role in cell division. *EMBO J* **26**: 4694-4708.

Lu, C., Reedy, M., Erickson, H.P. (2000) Straight and curved conformations of FtsZ are regulated by GTP hydrolysis. *J Bacteriol* **182**(1): 164-170.

Lutkenhaus, J. (1993) FtsZ ring in bacterial cytokinesis. *Mol Microbio* **9** :403-409.

Lutkenhaus, J., Pichoff, S., and Shishen, D. (2012) Bacterial Cytokinesis: From Z Ring to Divisome. *Cytoskeleton* **69**: 778-790.

Margolin, W. (1998) A green light for the bacterial cytoskeleton. *Trends Microbio* **6**: 233-238.

Milne, J.L.S., Subramaniam, S. (2009) Cryo-electron tomography of bacteria: progress, challenges and future prospects. *Nat Rev Microbiol.* **7**(9):666-675

Nanninga, N. (1991) Cell division and peptidoglycan assembly in *Escherichia coli*. *Mol. Microbio* **5**(4): 791-795.

Pinto, I.M., Rubinstein, B., Kucharavy, A., Unruh, J., and Li, R. (2012) Actin depolymerization drives actomyosin ring contraction during budding yeast cytokinesis. *Cell* **22**: 1247–1260

Pischoff, S., Lutkenhaus, J. (2002) Unique and overlapping roles for ZipA and FtsA in septal ring assembly in Escherichia coli. *EMBO J* **21**(4): 685-693.

Pum, D., Messner, P., and Sleytr, U.B. (1991) Role of the S-layer in Morphogenesis and Cell Division of the Archaebacterium *Methanocorpusculum sinense*. *J Bacteriol* **173**(21): 6865-6573.

Rohlin, L., and Gunsalus, R.P. (2010) Carbon-dependent control of electron transfer and central carbon pathway genes for methane biosynthesis in the Archaean, *Methanosarcina acetivorans* strain C2A. *BMC Microbiol* **10**: 62.

Rohlin, L.,Trent, J.D., Salmon, K., Kim, U., Gunsalus, R.P. and Liao, J.C.(2005) Heat shock response in *Archaeoglobus fulgidus. J. Bacteriol* **187**:6045-6057.

Samson, R.Y. and Bell, S.D. (2011) Cell cycles and cell division in the archaea. *Cur Op Microbio* **14** : 350-356.

Sun, Q., Margolin, W. (1998) FtsZ dynamics during the division cycle of live Escherichia coli cells. *J Bacteriol* **180**(8) : 2050-2056.

Toso, D.B., Henstra, A.M., Gunsalus, R.P., and Zhou, Z.H. (2011) Structural, mass, and elemental analyses of storage granules in methanogenicarchaeal cells. *Env. Microbiology* **13**(9): 2587–2599.

Wang, X., Lutkenhaus, J. (1996) FtsZ ring: the eubacterial division apparatus conserved in archaebacteria. *Mol. Microbio.* **21**(2):313-319.

Chapter V

Prospectus

There are still some questions left unanswered and further work than can be done based on some preliminary studies. Here is a brief rundown of what remains to be completed.

Reconstruction of cell ends including plugs and flagella of M. hungatei

Although the ends of the cells were examined, to some degree, by cryo ET of dividing cells. A molecular level resolution reconstruction of the components of would provide a much better understanding of the organization and function of the components that make up the cell ends, mainly the multi-layered plug structure and flagella that protrude from the cell.

Initial, early studies of extracted plugs were performed, examining negatively stained plug layers (Fig. 5-1A & B) as well as by cryo EM. In addition, initial ET reconstructions were made to examine the 3D structure of the plugs after segmentation (Fig. 5-1E). Unfortunately, the sample preparation procedure was very difficult to reproduce and did not provide a high concentration of sample or of sufficient quality. Another drawback was that the layers of the plugs were disassociated from the cell architecture and from each other, so an assessment of their arrangement and interaction in their native environment was not possible by this approach.

The flagella of *M. hungatei* were initially examined by extraction and attached to whole cells and negatively stained (Fig. 5-1C & D). The structure of the archaeal flagella has not been examined very thoroughly. It is known that it functions similarly to bacterial flagella, however, its composition and assembly are quite distinct. They are much thinner, around 10 nm in diameter, are composed of unique archaeal flagellin proteins, and assemble in a solid filament from the base rather than the distal end in the shape of a tube (Bardy et al., 2003). They more closely resemble the bacterial type IV pilus system in structure, gene homology, and several other characteristics (Ng et al., 2006).

A high resolution structure is being pursued via helical reconstruction by other members of our group. Along with biochemical and mass spec data, a much more thorough understanding of the structure and function of this unique motility apparatus is expected.

M. hungatei external layer characterization to higher resolution

M. hungatei, which was originally found in sewage sludge, itself is required to live in anaerobic environments for survival, as it is extremely sensitive to oxygen exposure. It is part of a group of methanogenic anaerobes that are essential for breaking down organic waste in the environment and has thus been utilized to process municipal wastewater and industrial waste (Schiraldi et al., 2002). The by-product of breaking down these organic wastes is the release of methane gas, which is a greenhouse gas but can also be utilized as fuel. There is evidence that the outer sheath layer is structured so that as methane gas builds between the membrane and the sheath, the increase in pressure causes the individual bands of the sheath to separate and release the gas, analogous to a pressure relief valve (Xu et al., 1996). By characterizing the sheath structure to higher resolution we may be able to determine if this assessment of its function is correct.

A series of CCD images of whole *M. hungatei* cells embedded in vitreous ice were acquired using the Titan Krios instrument in conjunction with the Leginon software package (Fig. 5-2). The cells imaged were in stationary phase to reduce the amount of growth and cell division related turnover present in the sample. Regions of the interior of the cells, which were as straight as possible, were collected in order to gather a dataset suitable for helical analysis of the sheath layer. It was discovered that the subunits of the sheath display a repeating pattern that does not seem to be completely ordered. Instead, there are sets of 3, 4, or 5 small repeating units within each of the larger subunits, and these different subunit sets do not repeat in a regular fashion. The lack of a regular repeating subunit pattern made reconstruction by helical symmetry much too difficult, so it was decided to try sub-tomogram averaging.

Sub-tomogram averaging involves boxing out many particles of a repeating or regular structure from the volume of a 3D tomogram and averaging these together to increase the SNR and get a higher resolution structure. In our preliminary study, the rigid, tubular structure of *M. hungatei* cells was exploited by boxing particles along a tube defined by two points at the center of the cell spaced along a straight segment with same the diameter as the cell. Points were selected from the whole circumference of the cell in order to get orientations of the outer layers of the cell in all directions (Fig. 5-3A). After picking the points, particles were boxed out from the 3D reconstruction and then went through an iterative process of alignment and averaging. After several rounds of alignment and averaging the resulting averaged structure shows a resolved lattice at the level of the S-layer (Fig. 5-3B) and the repeating banded structure at the level of the sheath (Fig. 5-3C). As is shown in the initial sub-tomogram averaged structure, a molecular level resolution of the S-layer and sheath is being approached. With further averaging and refinement of the procedure this method could elucidate molecular-level organization of these two envelope layers in *M. hungatei* cells. This procedure could also be applied to the multi-layered plug structure at the ends of each cell. One limitation is the fact that the cells always lie lengthwise and, therefore, the plugs have the same orientation in every tomogram. Sub-tomogram averaging may alleviate this problem to some degree. By examining the structure of the sheath, S-layer, plug, and other components of the complex envelope layers of *M. hungatei*, we will gain an understanding how this organism, as well as other Achaea, have adapted to their environments, which are often harsh in the extreme.

FIGURES

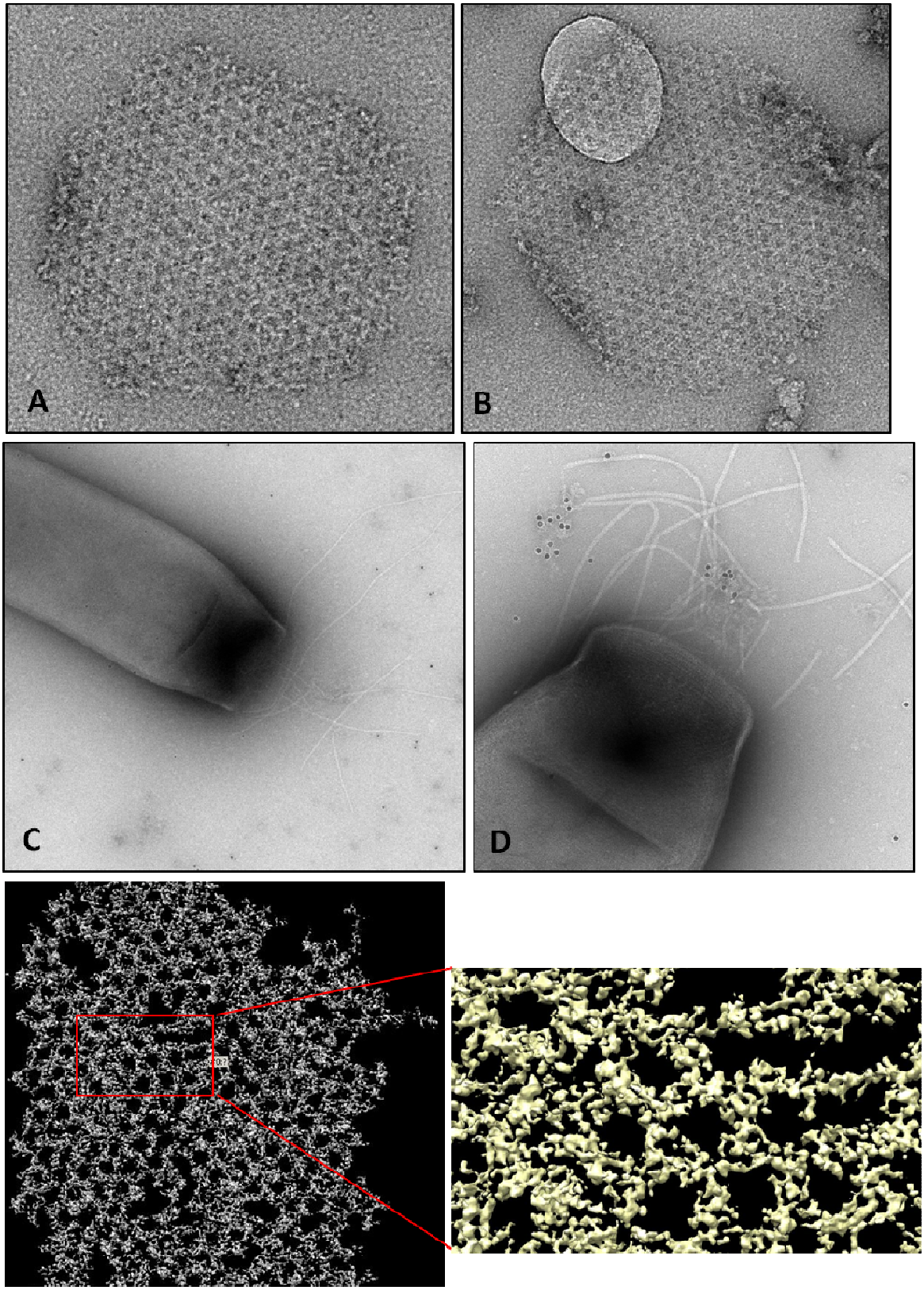

Fig. 5-1 Images of MH plug layers (A & B) and flagella (C & D), the samples have been negatively stained using 2.5% uranyl acetate. (E) Segmented structure of a ET reconstruction of an extracted plug.

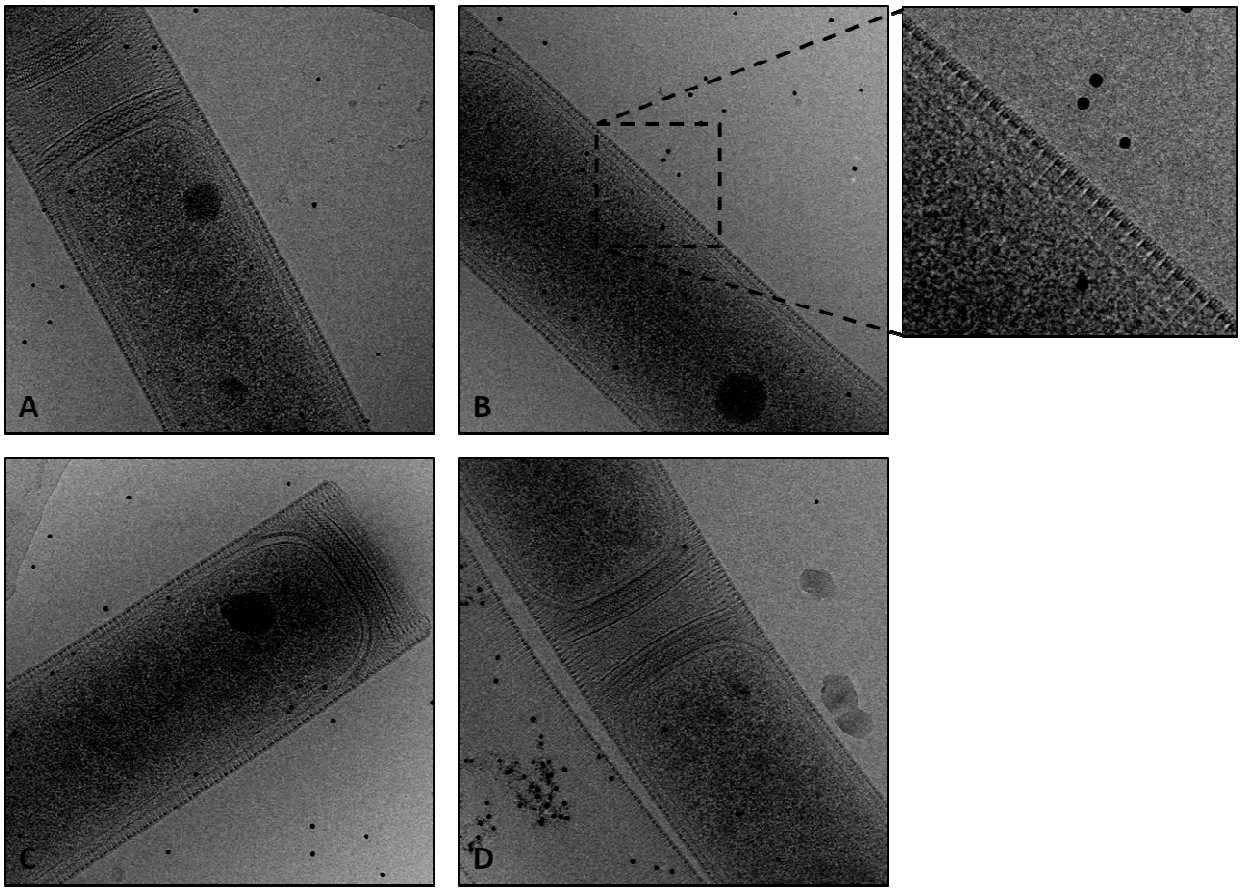

Fig. 5-2: (A-D) Images of straight segments of MH cells. The inset of (B) shows a close up view of the edge of a cell, which clearly shows the spacing of the sheath structure

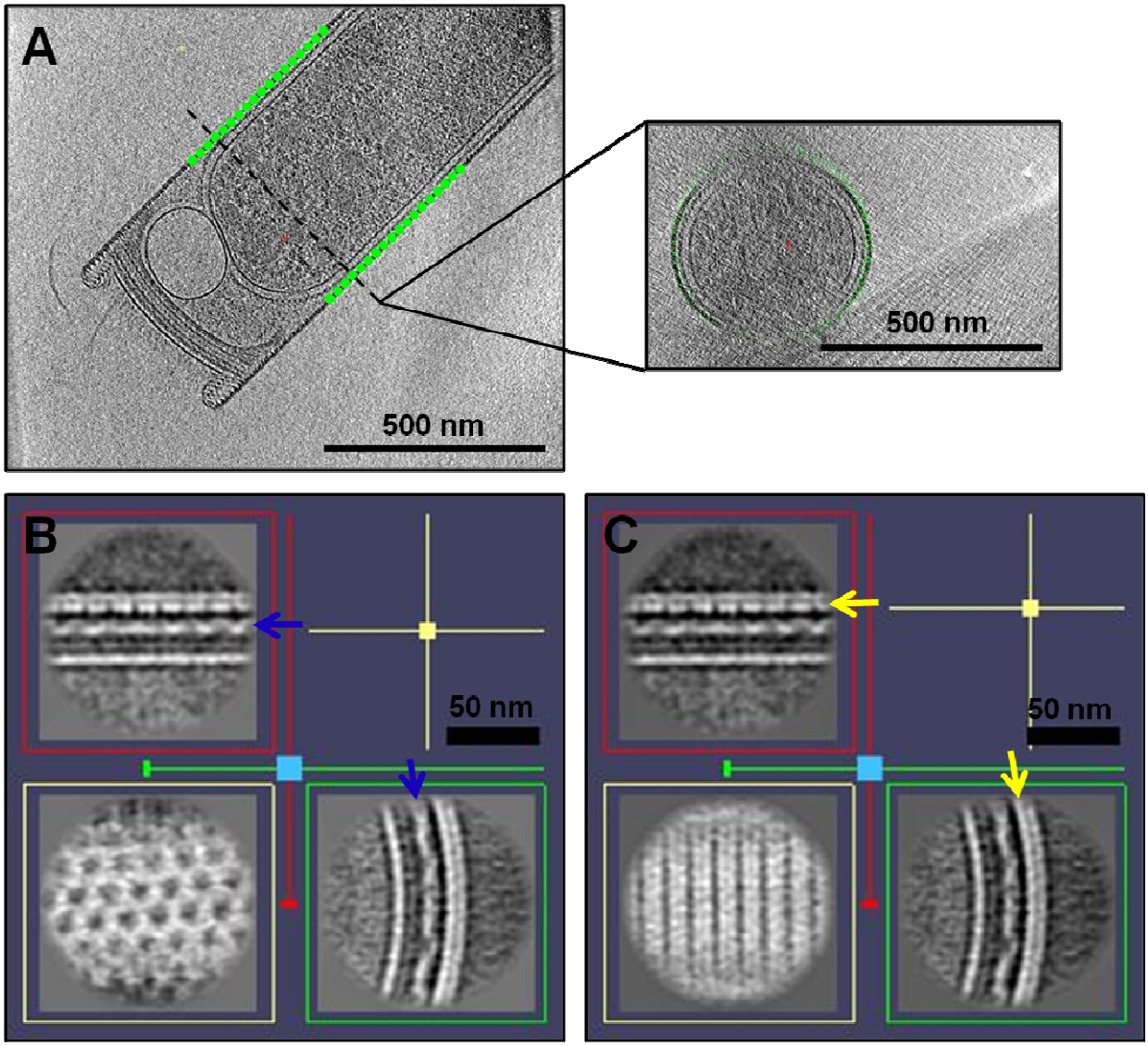

Fig. 5-3: Preliminary subtomogram averaging of *M. hungatei*. (A) Particle selection along the cellular surface of a cryo ET reconstruction. Inset shows a cross-sectional view. (B) S-layer structure after averaging. (C) Sheath structure after averaging.

REFERENCES

Bardy, S.L., Ng, S.Y., and Jarrell, K.F. (2003) Prokaryotic motility structures. *Microbiology* **149**: 295-304

Ng, S.Y., Chaban, B., and Jarrell, K.F. (2006) Archaeal flagella, bacterial flagella and type IV pili: a comparison of genes and posttranslational modifications. *J Mol Microbiol Biotechnol* **11**: 167-191.

Schiraldi, C., Giuliano, M., De Rosa, M. (2002) Perspectives on biotechnological applications of archaea. *Archaea* **1**(2): 75-86.

Xu, W., Mulhern, P.J., Blackford, B.L., Jericho, M.H., Firtel, M., and Beveridge, T.J. (1996) Modeling and measuring the elastic properties of an archaeal surface, the sheath of Methanospirillum hungatei, and the implication of methane production. *J Bacteriol* **178**(11): 3106-3112.